The effect of thermal properties and climatic factors on the behaviour of concrete elements.

Thulani Peter Mlilwana

Department of Civil Engineering

Faculty of Engineering, Built Environment, and Information Technology

University of Pretoria

A dissertation submitted in partial fulfilment of the requirements for the degree of

Master of Engineering (Structural Engineering)

2018

THE EFFECT OF THERMAL PROPERTIES AND CLIMATIC FACTORS ON THE BEHAVIOUR OF CONCRETE ELEMENTS.

Thulani Peter Mlilwana

A dissertation submitted in partial fulfilment of the requirements for the degree of

MASTER OF ENGINEERING (STRUCTURAL ENGINEERING)

In the

Department of Civil Engineering

Faculty of Engineering, Built Environment, and Information Technology

University of Pretoria

2018

Summary

THE EFFECT OF THERMAL PROPERTIES AND CLIMATIC FACTORS ON THE
BEHAVIOUR OF CONCRETE ELEMENTS.

Thulani Peter Mlilwana

Supervisor: Professor EP Kearsley

Department: Civil Engineering

University: University of Pretoria

Degree: Master of Engineering Structural Engineering

Concrete structures are subjected to complex and highly variable climatic conditions including temperature, wind speed, rainfall, and solar radiation. The thermal behaviour of concrete structures has become an important research area due to the increasing physical size of concrete structures and, more recently, the advent of integral construction methods which have gained popularity for reducing long-term maintenance requirements. While the demand for sustainable materials and construction methods has increased as measures are taken to adapt to and mitigate the effects of climate change, the human economy has grown. The energy required for these activities is released thermally into the atmosphere and is climate forcing.

In this dissertation the effect of variations in climatic conditions on the thermal response of simple concrete structures is investigated. After discussing previous studies relevant to this field, an experimental program is described, in which the effects of surface colour (albedo, solar absorptivity and emissivity), member geometry, material properties, and daily and seasonal climatic variations on the temperature distributions of three reference structures constructed in Pretoria, South Africa is studied. A two-dimensional finite element heat transfer model is developed to simulate the effect of these parameters.

It is found that high conductivity materials with high albedo surfaces, and minimal cross-sectional depth exhibit uniform thermal gradients. Thus, they are less prone to high stresses that could result in thermal cracking. Such combinations of geometry, materials and surfacing could be implemented as climate

adaption and mitigation measures as they simultaneously reduce the urban heat island effect and carbon dioxide emissions as the need for electrical heating and cooling in buildings is reduced.

Declaration

I, the undersigned hereby declare that:

I understand what plagiarism is and I am aware of the University's policy in this regard;

The work contained in this thesis is my own original work;

I did not refer to work of current or previous students, lecture notes, handbooks or any other study material without proper referencing;

Where other people's work has been used this has been properly acknowledged and referenced;

I have not allowed anyone to copy any part of my thesis;

I have not previously in its entirety or in part submitted this thesis at any university for a degree.

Signature:

Name:	Thulani Peter Mlilwana
Student number:	12159281
Date:	November 2018

Acknowledgements

I wish to express my appreciation to the following organisations and persons who made this project report possible:

Table of Contents

List of Figures

List of Tables

Nomenclature

A	$(T_{max} - T_{min})/2$ (°C)
A_d	Annual average temperature fluctuation about yearly average (°C)
A_i	Area of cross-section i (m^2)
B	$(T_{max} + T_{min})/2$ (°C)
B_d	Average yearly temperature (°C)
c	Specific heat (J/kg·°C)
d	Day of the year
E	Modulus of elasticity (GPa)
h^2	Thermal diffusivity (m^2/h)
h_c	Convection coefficient (W/m^2·°C)
I	Global or total solar radiation (W/m^2)
I_b	Direct light (W/m^2)
I_d	Diffuse light (W/m^2)
I_g	Light that is reflected from other surfaces (W/m^2)
I_n	Radiation on a surface normal to the sun (W/m^2)
k	Thermal conductivity (W/m·°C)
k_a	Thermal conductivity of aggregate (W/m·°C)
k_c	Thermal conductivity of concrete (W/m·°C)
k_p	Thermal conductivity of hydrated cement paste (W/m·°C)
q_c	Convective heat flux (W/m^2)
q_r	Total longwave radiation emitted by a surface (W/m^2)
q_s	Longwave radiation from the concrete surface (W/m^2)
q_{sky}	Longwave radiation from the sky (W/m^2)
r	Solar reflectivity
S	Total radiation for a single day (W/m^2)

t	Time after sunrise (Hours)
t_i	Time of day ($0 \le t \le 24$ Hours)
T	Temperature (°C)
T_{air}	Ambient air temperature (°C)
T_d	Daily average temperature (°C)
T_i	Temperature of cross-section i (°C)
T_{mean}	Effective temperature of total cross-section (°C)
T_{max}	Maximum daily temperature (°C)
T_{min}	Minimum daily temperature (°C)
T_s	Surface temperature (°C)
T_{sd}	Length of solar day (Hours)
T_{sky}	Equivalent sky temperature (°C)
u	Wind speed (m/s)
V_a	Volume fraction of aggregate
α	Coefficient of thermal expansion (10^{-6}/°C)
α_{SR}	Solar absorptivity
ε	Elastic strain (µm/m)
ε_c	Emissivity of the concrete surface
θ	Solar radiation input (Radians)
θ_n	Angle between the tilted surface and the earth (Degrees)
ρ	Density (kg/m³)
ρ_d	Oven-dry density (kg/m³)
ρ_m	Density in moist condition (kg/m³)
σ_{SB}	Stefan-Boltzmann constant (5.97×10^{-8} W·m^{-2}·K^{-4})
σ	Elastic stress (MPa)
γ	Annual Lag factor ($100 \le \gamma \le 110$ days)
ζ	Daily Lag factor (9 Hours)

Chapter 1   Introduction

1.1   Background

Sustainable development has been defined by the World Commission on Environment and Development (Brundtland et al., 1987), as "*development that meets the needs of the present without compromising the ability of future generations to meet their needs*". The Brundtland Commission not only recognised that many of the challenges presently faced across the world are interrelated crises that form a single global problem, but also presented realistic solutions that could be implemented at national and internal levels to address the challenges affecting sustainable deployment. Following proceedings of the Commission, member states of the United Nations adopted protocols, treaties and resolutions for the achievement of sustainable development goals. In 2015, the African Union Commission adopted Agenda 2063, a strategic framework that seeks to accelerate the implementation of continental initiatives for growth and sustainable development (AUC, 2015).

The growth of the human economy has influenced the demand for sustainable materials and the proliferation of construction methods. Presently, concretes produced with Portland cement are the most widely used construction materials in the world in terms of volume. The development of infrastructure, industry and housing is largely attributable to the readily available raw materials, strength and durability characteristics of concrete. However, these activities are climate forcing as the production of Portland cement contributes up to 5% of all anthropogenic carbon dioxide emissions (Damtoft et al., 2008). Concrete structures are subjected to complex and highly variable climatic conditions including air temperature, wind speed, rainfall, and solar radiation. The thermal behaviour of concrete structures has become an important research subject due to the increasing physical size of concrete structures and, more recently, the advent of integral construction methods which have gained popularity for reducing long-term maintenance costs. It is known that concrete has substantial heat capacity and is thus able to store large amounts of energy. This energy is released thermally into the atmosphere, further influencing the climate change conundrum.

Since the early 1960s, researchers have investigated the response of engineering structures to parameters such as ambient temperature, solar radiation and wind speed with many of the previous studies being performed under European climatic conditions. Consequently, the recommendations obtained several decades ago require validation due to increases in the average global temperature and

increased variability of regional climates. In addition to the change in global climates, in recent times Southern African climatic conditions have exhibited greater variability between maxima and minima due to El Niño oscillations (Hulme et al., 2001).

In this research project, the thermal behaviour of concrete elements exposed to the Southern African climate is investigated. The research presented in this dissertation seeks to make a meaningful contribution to the development of climate change mitigation strategies by investigating the effect of surfacing material colour on the thermal behaviour of concrete structures. It is posited that the use of light-coloured materials for surfacing could effectively reduce urban temperatures thereby reducing cooling demands and greenhouse gas emissions.

1.2   Objective of Study

The objective of this research project was to investigate the thermal behaviour of normal-weight concrete beams that were exposed to diurnal and seasonal variations in climate. In this dissertation the following relationships are investigated:

- The influence of climatic actions on the thermal behaviour of simply supported concrete beams. The climatic actions to be considered include ambient temperature, solar radiation, rainfall, and wind speed;
- The influence of thermal mass on transient thermal behaviour;
- The influence of the thermal properties of concrete on thermal behaviour; and
- The Influence of surface emissivity and solar absorptivity on the surface temperatures and vertical temperature distributions within simply supported concrete beams.

1.3   Scope of Study

In this research project, the effects of thermal loading and surface properties on the behaviour of simply supported concrete beams were investigated. Three simply supported beams with identical dimensions were instrumented and constructed at the University of Pretoria Concrete Laboratory. A normal-weight concrete mix composition produced using Portland cement and aggregates produced in South Africa produced and used to construct the aforementioned beams. In order to accurately predict the thermal behaviour of homogenous concrete material, steel reinforcement was not provided in any of the test specimens. The instrumentation used in the study included thermistor sensors, temperature compensated concrete embedment strain gauges and foil strain gauges that were used to measure

internal temperatures, strain and climatic variations from January 2018 to July 2018 with data collected every 15 minutes throughout the study period using a combined data acquisition system. Following the experimental investigation, a two-dimensional finite element heat transfer model was developed and validated using the experimentally measured thermal responses and data. Following this, the validated numerical model was used to simulate the effect of the variables described in Section 1.2 on the thermal behaviour of simply supported members with homogenous material properties.

1.4   Research Methodology

Following a review of relevant literature, an experimental program consisting of three phases was conducted. In Phase I, three instrumented concrete beams were cast using a single concrete mix composition. The beams were then cured under laboratory conditions for seven days. This was followed by Phase II, in which the beams were allowed to dry under laboratory and outdoor conditions to determine an analysis datum for all the beams before the beam surfaces were painted. In Phase III, an experiment was designed in which the newly surfaced concrete beams (whitetop, greytop, and blacktop) were exposed to atmospheric conditions on the roof of a building at the University of Pretoria Hatfield campus from January 2018 to July 2018. The experimental site was selected to ensure an unobstructed horizon. The aim of the final stage was twofold:

- Firstly to investigate the thermal behaviour of mature concrete with different surface characteristics under climatic loading, and
- To aid the development and validation of a finite element thermal prediction model.

A two-dimensional finite element heat transfer model was developed in Abaqus/Standard, a general purpose analysis module in the Abaqus suite of finite element programs. The model was used to simulate the behaviour of the concrete beams described above and was validated using measured temperature data. Following the successful development of the heat transfer model, a parametric investigation was performed to extend its analysis capabilities and address the limitations of the experimental investigation. In the parametric study, the following variables were investigated:

- Climatic actions such as global radiation, air temperature, and wind speed;
- Cross-sectional dimensions of the concrete element;
- Adiabatic heat transfer boundaries;
- Thermal properties of the concrete, and
- Surface characteristics, namely solar absorptivity and emissivity.

1.5   Organization of the Dissertation

This dissertation is organised into seven Chapters with additional appendices as follows:

- Chapter 1, Introduction, serves to provide the reader with the background and motivation for the research conducted in this dissertation. The chapter further serves to describe the objectives and scope of the study, as well as an outline of the research methodology that was followed.

- Chapter 2, Literature Study, serves to inform the reader on the present state of knowledge regarding the thermal properties of concrete, climatic loading of concrete structures, and the effect of surfacing characteristics on the behaviour of concrete structures.

- Chapter 3, Experimental Study, describes the experimental procedure followed to achieve the research objectives. The materials, instrumentation, and test methods used are described in detail. The trends observed in the experimental study are presented, followed by a comparison of some results with relevant research that has been previously conducted.

- Chapter 4, Finite Element Model Development, provides a background into the interpretation of climatic parameters, material and surface characteristics, and heat transfer methods for use in finite element modelling. Using the aforementioned components, the development and validation of a finite element thermal prediction model is described.

- Chapter 5, Finite Element Model Implementation, describes the use of the finite element thermal prediction model developed in Chapter 4 to perform a parametric study. The climatic actions used are presented and discussed.

- Chapter 6, Results Analysis and Discussion, contains a presentation of the parametric study and an analysis of results thereof.

- Chapter 7, Conclusions and Recommendations. In this chapter, conclusions regarding the research objectives are presented. Lastly, recommendations for future research are presented.

Chapter 2   Literature Study

2.1   Introduction

In this chapter a review of the current state of knowledge regarding the effects of climatic actions on the design and behaviour of concrete structures and elements is presented. The literature study begins with an introduction to the fundamental principles of heat transfer related to concrete structures. This is followed by an introduction to mass concrete with emphasis placed on the thermal characteristics thereof. Previous research relevant to the effect of climatic actions on concrete structures and elements, as well as current design guidelines used by bridge, pavement and structural engineers for thermal actions are discussed. This chapter is concluded with a brief introduction to the use of numerical simulation for the prediction of the thermal behaviour of mature concrete.

2.2   Climatic Loading of Concrete Structures

Concrete structures are subjected to complex and highly variable climatic conditions including diurnally and annually varying air temperature, solar radiation, wind, relative humidity, and the various forms of precipitation such as rain, snow and hail. Since the early 1960s, researchers have investigated the structural response to these parameters as the physical size of concrete structures increased and the advent of modern construction methods required a greater understanding of thermal behaviour. In conventional structural design, strength, serviceability and durability requirements are used to determine the size of structures and structural elements. The economical design of concrete structures with large horizontal surfaces such as bridge superstructures, roofs and pavements and the increased demand for maintenance-free infrastructure requires climatic actions to be understood and considered in addition to the permanent or variable dynamic and static actions that are expected during the asset lifecycle. The structural response is dependent on restraint to free movement, geometry, geographic location, daily and seasonal variation in weather conditions and the thermal properties of the construction material (Elbadry and Ghali, 1983).

Extensive climatic information is not always available thus it is often necessary to use prediction models based on known local climate trends and geographical information. In this section, the heat transfer principles that are used to predict the response of concrete structures subjected to solar radiation, varying air temperature and wind and the models that are used to generate climate data are presented.

2.2.1 Solar Radiation

The term solar radiation refers to the short wavelength electromagnetic energy that is emitted by the surface of the sun. The characteristic wavelengths of solar radiation occur due to the sun's surface temperature being higher than the surrounding temperature. On the electromagnetic spectrum, approximately half of solar radiation occurs in the visible light fraction while the other half occurs in the infrared region hence a minor portion of this radiation is absorbed by the earth's atmosphere while up to 90% of the remaining radiation passes through gaps in the ozone layer to reach the earth's surface. The latter fraction is known as global or total solar radiation. It is absorbed by the earth, vegetation and other objects near the earth's surface. The total energy that is transferred between a given surface and the surrounding environment is expressed by Equation 2-1 (Larsson and Thelandersson, 2011):

$$q = q_s + q_r + q_c \qquad \text{(Equation 2-1)}$$

where:

q = Heat energy absorbed (W)

q_s = Solar radiation flux (W)

q_r = Longwave radiation (W)

q_c = Convective heat flux (W)

Equation 2-1 is, however, wavelength specific and is applicable when the absorptivity is equal to the emissivity of the radiated surface. This does not apply to visible light or solar radiation, for which a dimensionless absorptivity coefficient that is dependent on surface texture and colour must be taken into account using Equation 2-2 (Larsson and Thelandersson, 2011). The solar absorptivity coefficient is also time dependent as the colour of concrete and painted surfaces changes with age. It is known that the solar absorption coefficient of unsurfaced concrete ranges from 0.5 to 0.8. In instances where concrete is covered by a bituminous overlay, such as on bridge superstructures and roofs where asphalt is used for waterproofing, the coefficient increases to 0.9 (Emerson, 1973; Branco and Mendes, 1993).

$$q = \alpha_{SR} \cdot I \qquad \text{(Equation 2-2)}$$

where:

q = Heat energy absorbed (W)

α_{SR} = Solar absorption coefficient between 0 and 1

I = Total solar radiation received on a surface (W/m^2)

The intensity of global radiation varies with latitude and longitude, time of day and year, and the orientation and inclination of a surface, ranging from 1000 W/m² on clear sunny days to 300 W/m² on cloudy days. The global radiation that is received by a horizontal surface is defined by Equation 2-3, while the global radiation received by a tilted surface is defined by Equation 2-4:

$$I_n = I_b + I_d + I_g \qquad \text{(Equation 2-3)}$$

where:

I_n = Global radiation (W/m²)

I_b = Direct light (W/m²)

I_d = Diffuse light (W/m²)

I_g = Light that is reflected from another surface (W/m²)

$$I = I_n \cos \theta_n \qquad \text{(Equation 2-4)}$$

where:

I = Global radiation (W/m²)

I_n = Radiation on a surface normal to the sun (W/m²)

θ_n = Angle between the tilted surface and the earth (Degrees)

The earliest research investigating the effect of climatic actions on concrete bridge structures was conducted during the 1960s when reliable measurements of global radiation intensity were unavailable or limited by the technology that was accessible. Several researchers proposed models based on the total daily global radiation to predict hourly global radiation intensity. Examples of such models were proposed by agricultural scientists, structural and pavement engineers including Monteith (1965), Gloyne (1972), Elbadry and Ghali (1983), as well as Hulsey and Powell (1993).

Equation 2-5 shows the hourly global radiation intensity model that was proposed by Gloyne (1972). This function produced a modified sine wave as shown in Figure 2-1, where the global radiation intensity is equally distributed with a maximum value at the local apparent noon (LAN) and approaches zero global radiation at sunrise and sunset times. This model was found to be in good agreement with measured global radiation intensity. Figure 2-2 shows a comparison between measured global radiation on bridges in the United Kingdom and global radiation intensity predicted using Equation 2-5.

$$I(t) = \frac{2S}{T_{sd}} \, sin^2(\theta)$$

(Equation 2-5)

where:

$I(t)$ = Solar radiation intensity (W/m²)

t = Time after sunrise (Hours)

S = Total radiation for a single day (W/m²)

T_{sd} = Length of solar day (Hours)

θ = $2\pi/t$ (Radians)
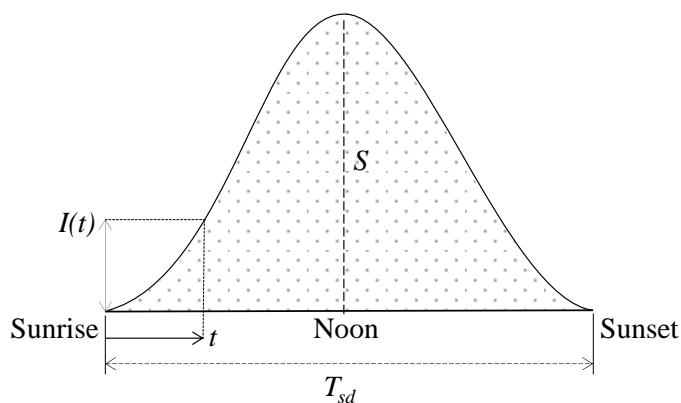
Figure 2-1: Estimation of global solar radiation (Adapted from Gloyne, 1972)
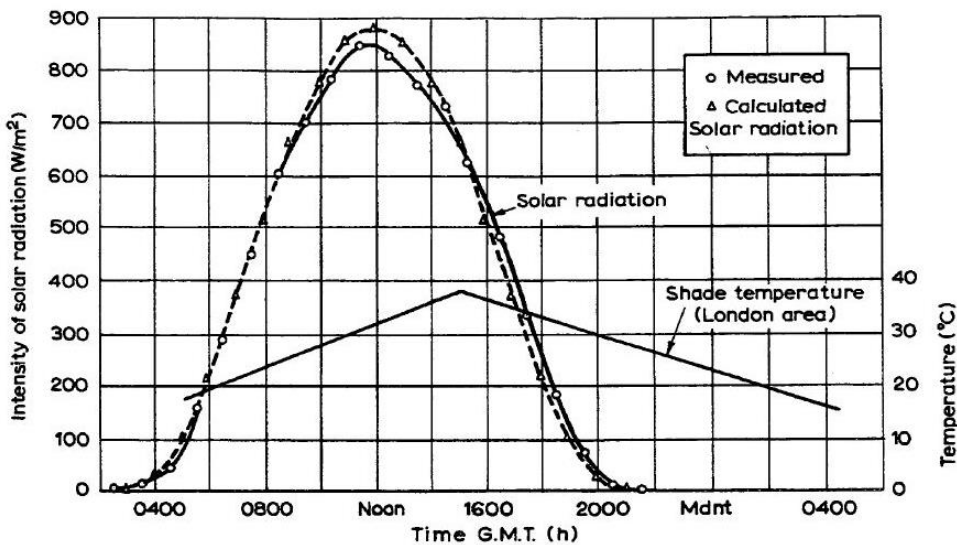
Figure 2-2: Comparison of predicted and calculated solar radiation intensity (Emerson, 1973)

2.2.2 Longwave Radiation

Longwave radiation is the outgoing radiation that is emitted by the surfaces of objects near the earth's surface and absorbed by the surrounding atmosphere. Longwave radiation is constantly emitted, however, the largest effect of this heat transfer component occurs at night in the absence of solar radiation. Several authors published typical values of longwave radiation from concrete structures ranging from -95 W/m² to -125 W/m² with a mean value of -110 W/m² which was assumed to be a constant value from 18:00 to 06:00 (Emerson, 1973).

The heat transfer between the emitting surface and the surrounding environment is governed by the Stefan-Boltzmann law as shown in Equation 2-6 (Larsson and Thelandersson, 2011).

$$q_r = q_s - q_{sky} = \sigma_{SB} \cdot \varepsilon_c \, (T_s^4 - T_{sky}^4) \qquad \text{(Equation 2-6)}$$

where:

q_r = Total longwave radiation emitted (W/m²)

q_s = Long wave radiation from the concrete surface (W/m²)

q_{sky} = Long wave radiation from the sky (W/m²)

σ_{SB} = Stefan-Boltzmann constant (5.97 x 10⁻⁸ W·m⁻²·K⁻⁴)

ε_c = Emissivity of the concrete surface

T_s = Surface temperature (°C)

T_{sky} = Equivalent sky temperature (°C)

The emissivity of concrete is typically between 0.8 and 0.9 (Branco and Mendes, 1993). The equivalent sky temperature is determined by considering the surrounding air as a surface and rewriting the Stefan-Boltzmann law (Equation 2-6) as Equation 2-7, or by using the simplified relationship shown in Equation 2-8 (Larsson and Thelandersson, 2011).

$$T_{sky} = \sqrt[4]{\frac{q_{sky}}{\sigma_{SB} \cdot \varepsilon_c}} \qquad \text{(Equation 2-7)}$$

$$T_{sky} = T_{air} - 6 \qquad \text{(Equation 2-8)}$$

where:

T_{sky} = Equivalent sky temperature (°C)

T_{air} = Ambient air temperature (°C)

2.2.3 Air Temperature

Ambient air temperature varies according to two cycles, namely the annual cycle and diurnal cycle. Globally, annual trends are observed as changes in season, with summer and winter accounting for extreme temperatures, while diurnal trends account for daily variation (warm days and cool nights). Annual trends show little variation from year to year, however, daily trends can be altered by variable cloud cover, wind speeds, and precipitation (Hulsey and Powell, 1993). Given historical annual average temperatures, it is valid to assume that annual trends follow periodic cycles of the form shown in Equation 2-9 in which the annual lag factor was determined by trial-and-error and represented the time elapsed between the maximum and minimum daily temperatures. The temperature data produced with this model can be applied at other sites with confidence if the sites are in close proximity or in zones of similar climatic and geographical characteristics (Hulsey and Powell, 1993).

$$T_d = A_d \sin\left[\frac{2\pi\,(d-\gamma)}{365}\right] + B_d \qquad \text{(Equation 2-9)}$$

where:

T_d = Daily average temperature (°C)

A_d = Annual average temperature fluctuation about yearly average (°C)

B_d = Average yearly temperature (°C)

γ = Annual lag factor ($100 \leq \gamma \leq 110$ Days)

d = Day of the year ($0 \leq d \leq 365$)

If historical daily maximum and minimum daily temperatures were known, diurnal temperature trends could be predicted using Equation 2-10. The daily lag factor in this equation represented the time elapsed between the surmise hour, which was assumed to be 05:00, and the time at which the maximum daily temperature occurred (14:00) (Hulsey and Powell, 1993).

$$T_{air\,i} = A \sin\left[\frac{2\pi\,(t_i - \zeta)}{24}\right] + B \qquad \text{(Equation 2-10)}$$

where:

$T_{air\ i}$ = Air temperature at time i (°C)

A = Half of daily temperature range (°C)

B = Average daily temperature (°C)

ζ = Daily lag factor (9 Hours)

t_i = Time of day ($0 \leq t \leq 24$)

T_{max} = Maximum daily temperature (°C)

T_{min} = Minimum daily temperature (°C)

2.2.4 Convection

Heat transfer between surfaces of concrete structures and the air in the immediate vicinity of the surfaces occurs by convection. The convective heat transfer process consists of two phenomena, namely, advection and diffusion. Near the surface, heat energy is transferred between the randomly and slow-moving air particles by diffusion. Further away from the surface, where the large air mass moves uniformly, heat transfer occurs by advection (Incropera et al., 2007).

For convection to occur, a temperature gradient is required between the material surface and the surrounding air. The air temperature can be predicted by the sinusoidal functions for daily and annual cycles (See Equation 2-9 and Equation 2-10). The quantity of convective heat flow is governed by Newton's law of cooling which is shown in Equation 2-11:

$$q_c = h_c(T_s - T_{air}) \qquad \text{(Equation 2-11)}$$

where:

q_c = Convective heat flux (W/m^2)

h_c = Convection coefficient (W/m^2·°C)

T_s = Surface temperature (°C)

T_{air} = Ambient air temperature (°C)

The convective heat transfer coefficient for slabs can be approximated by Equation 2-12, which was proposed for slabs with surface areas less than or equal to 0.5 m^2 and Equation 2-13 which was proposed for slabs with areas greater than 0.5 m^2 (Larsson and Thelandersson, 2011):

For surface area ≤ 0.5 m^2 :

$$h_c = 5.7 + 3.8u \qquad \text{(Equation 2-12)}$$

For surface area > 0.5 m^2 :

$$
\begin{aligned}
h_c &= 6 + 4u & \text{If } u \leq 5 \text{ m/s}\\
h_c &= 7.4u^{0.78} & \text{If } u > 5 \text{ m/s}
\end{aligned}
\qquad \text{(Equation 2-13)}
$$

where:

h_c = Convection coefficient (W/m$^2\cdot$°C)

u = Wind speed (m/s)

2.2.5 Annual Climate Trends

In research conducted by Emerson (1968, 1973), large temperature gradients were observed on days with high solar radiation, high maximum and minimum ambient temperatures, shade temperature ranges between 15 °C and 20 °C, and low wind speeds (8 m/s to 11 m/s). The above conditions were referred to as ideal conditions, however, high wind speed increased the convective heat transfer coefficient, h_c. This increase in convective heat loss could result in the cooling of the top surface and negative temperature gradients (Emerson, 1973; Potgieter and Gamble, 1989).

Emerson (1973) found that ideal conditions occurred on four to six days during summer months with the day on which the largest quantity of total solar radiation would be absorbed by a surface under ideal conditions being the summer solstice, December 21st and June 21st in the Southern and Northern hemispheres respectively. The minimum daily temperature was assumed to occur at 05:00 $\pm$ 1 hour, and the maximum daily temperature at 15:00 $\pm$ 1 hour. These assumptions were applicable to all summer months and they formed the basis for the estimation of hourly air temperatures and hour solar radiation (Emerson, 1973).

During winter months, large reversed temperature gradients were observed on nights with minimal wind speed, low shade temperature range, low cloud cover, and maximum outgoing radiation. These conditions occurred on three to five nights during winter months (Emerson, 1973).

2.3 Climate Change and Climate Variability

Global population growth and the subsequent increase in energy requirements have resulted in rapid increases in atmospheric aerosol concentrations and emissions of greenhouse gases, the majority of

which is carbon dioxide, CO_2. Climate models indicate that these increases in the atmospheric CO_2 composition have resulted in an increase in the average earth temperature. The aforementioned process is known as anthropogenic heat that is climate forcing and has resulted in the warming of ambient air along with two other processes, namely, the direct absorption of solar radiation and the convection of thermal energy from warm surfaces (Akbari, 2012). The latter process is discussed in greater detail in Section 2-4. The climate change phenomenon which includes global warming is unequivocal, however, it is not within the scope of this study. This section of the literature study serves to provide context for the future climatic exposure of engineering structures with emphasis on the Southern African Climate.

Over the last decade, several researchers have attempted to understand climate change in order to forecast future climate trends. Jones et al. (2001) published a review of climate trends over the last millennium. At the time of publication, climatic records since the 1850s showed that global warming had occurred in two main time periods, 1920 to 1945, and 1975 to 2000. Average temperatures had increased by 0.6 °C, with marked seasonal differences: 0.4 °C in summer and 0.8 °C in winter. However, from 1945 to 1975, global cooling was observed. The study showed that global warming is a misnomer for climate change, as the scope of climate change includes the cooling of average air temperatures and the increased occurrences of extreme events such as flooding, tropical cyclones, and seismic sea waves.

Hulme et al. (2001) evaluated changes in the climate of Africa from 1900 to 2000 as well as the possible future climatic trends for the years 2000 to 2100. These researchers investigated the aspects of regional climate change related to the diurnal temperature range and rainfall variability with the latter including an investigation of areas where rainfall is sensitive to El Niño climate variability. It was found that the continental temperature increased at a rate of 0.5°/century, with moderately higher rates of warming during summer months. These continental rates of warming were not dissimilar to the global rates published by Jones et al. (2001). The climates of Africa were described as being varied with regard to geography and the degree of temporal variability. The analysis of changes in mean temperature and rainfall between 1901 and 1995 are shown in Figure 2-3.

Power and Mills (2005) investigated solar radiation changes in Southern Africa. It was found that annually averaged global radiation decreased by 1.7% or 4.4 W/m^2 per decade in major cities in South Africa including Bloemfontein, Cape Town, Durban, and Pretoria. The researchers posited that a simultaneous decrease in daily sunshine duration and the increased use of aerosols in the region contributed to the decrease in global radiation.
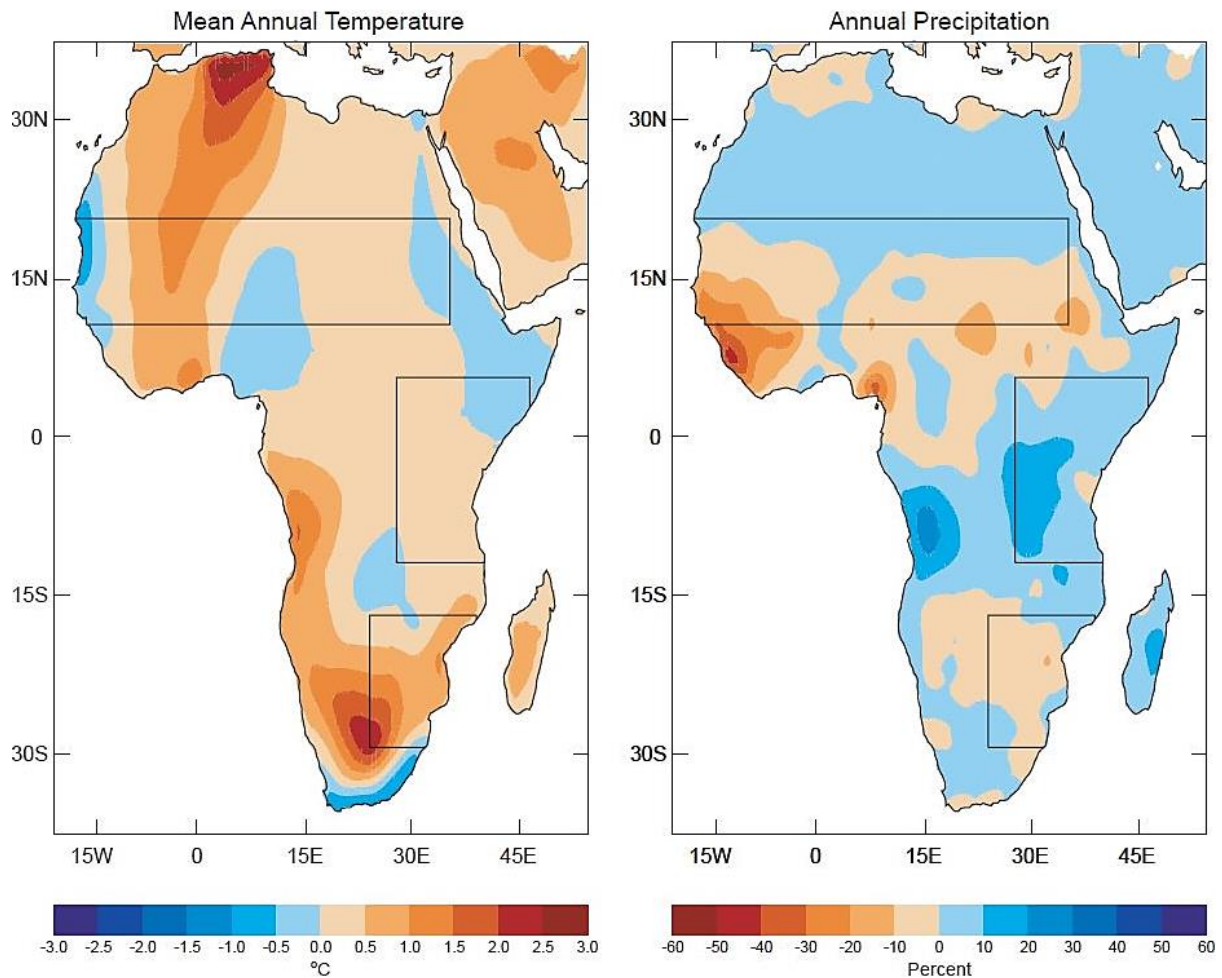
Figure 2-3: Average linear change in temperature and rainfall from 1901 to 1995 on the African continent (Adapted from Hulme et al., 2001)

The review of past climate change provides the context for future anthropogenic climate change as future increases in global temperatures and occurrences of extreme events are forecast to exceed the changes observed during the previous millennium. Under the Paris Agreement, 197 countries agreed to limit the increase in the global average temperature to *"well below 2 °C above pre-industrial levels"* (UNFCCC, 2015). The Intergovernmental Panel on Climate Change (IPCC) developed a special report on the impacts of global warming of 1.5 °C above pre-industrial levels and related greenhouse gas emissions. The report indicated that the occurrence and intensity of extreme events would substantially worsen if the global average temperature increased by 1.5 °C and that this limit could be exceeded as early as 2030 or by 2038 if CO_2 emissions did not decrease. Beyond the 2 °C threshold, the impacts of climate change would become irreversible (IPCC, 2018).

2.4   The Urban Heat Island Effect

The ambient air temperature in urban areas is much higher than that found in suburban and rural settlements. This is primarily due to convective heat transfer from the surfaces of two engineering materials: concrete and asphalt. These construction materials are the dominant materials in urban areas, with pavement materials making up between 29% and 45% of urban footprints (Akbari, 2012). Concrete and bituminous materials are thermal mass materials that have high volumetric heat capacities and are largely impervious to moisture ingress. The increased storage and release of thermal energy results in an increase of the surrounding air temperature throughout diurnal cycles while the impervious surfaces are associated with increased runoff, lower water quality and reduction in the quality of vegetation. The increase in air temperature is pronounced at night when concrete releases the energy absorbed during the day.

This phenomenon is known as the urban heat island effect (Barnes et al., 2001; Oke, 2002). As a result of this effect, cooling requirements increase and energy consumption increases by 2% to 4% for every 1 °C rise in the daily maximum air temperature above a threshold of 15 °C to 20 °C (Akbari, 2009). Additionally, the high urban temperatures are associated with increased production of ozone, which presents environmental, health and economic challenges (Rosenfeld et al., 1996). Figure 2-4 (Oke, 2002) is a generalised cross-section of an urban area which shows that the greatest increase in temperature occurs in the transition zone from rural to suburban spatial planning as vegetation and open greens are reduced. These ambient temperatures are maintained in suburban areas and reach peak temperatures above urban areas where the largest difference between urban and rural temperatures, $\Delta T_{\text{u-r}}$ is observed.
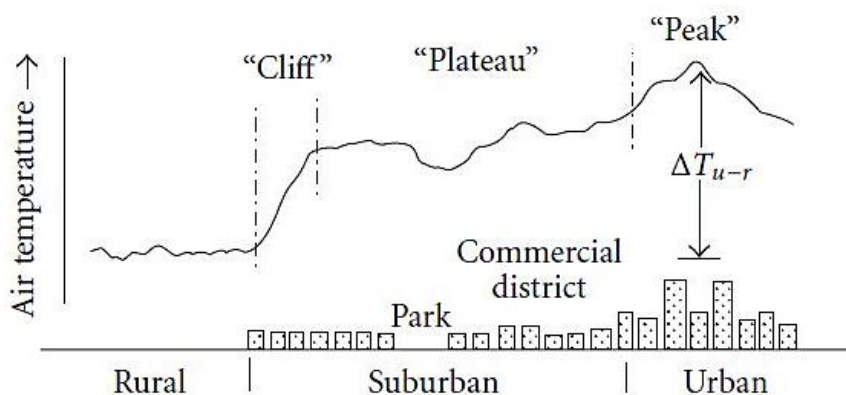
Figure 2-4: Generalised cross-section of an urban heat island (Oke, 2002)

The demand for cooler cities has resulted in increased research and development of cooling technologies which include blue roofs, sky gardens, cool pavement technology, and the usage of light-coloured surfacing on concrete structures. The aforementioned cooling technologies have been found to reduce ambient and structural temperatures, however, the capital and maintenance costs often render such methods unfeasible. This is the case with blue roofs and sky gardens, which require the provision of specialised waterproofing and increased strength in structural components as the increased weight supported by these roofs must be accounted for.

In studies performed in North American cities, it was found that cooling a city by 3 °C would reduce smog by 12%, resulting in annual energy savings of US$ 360 000 000 (approximately US$ 579 983 000 NPV), of which US$ 76 000 000 (approximately US$ 122 440 000 NPV) was a result of cooling the pavements (Rosenfeld et al. 1996). The net present values (April 2019) of the aforementioned monetary savings are parenthesised. Increasing the reflectivity of buildings by whitewashing resulted in direct energy savings of up to 14% and 19% on cooling peak power and electrical cooling energy respectively (Taha et al, 1988). These researchers showed that the use of reflective materials to cool urban areas is not only feasible but would result in significant future economic benefits.

The potential benefits of cool pavement technology and light-coloured surfacing for concrete structures require further research including the prediction of surface temperatures, structural response to thermal gradients, the choice of construction materials, and cost-effective implementation measures.

2.5   Mass Concrete

Concrete has been used as a building material for many centuries, with the most common form currently being ordinary Portland cement concrete which consists primarily of Portland cement, fine and coarse aggregates, and water. In structural applications, steel reinforcement is often provided for additional tensile and compressive resistance, as well as for the control of crack propagation due to thermal and moisture movements. The roles of Portland cement, aggregates and water in the composite concrete material are described below.

2.5.1   Portland Cement

Portland cement is a fine powder produced through an energy-intensive process that uses natural materials with substantial limestone and silica composition as raw materials. It is commercially available in various forms that are specified in the European Standard EN 197-1 (2000), with the most common type being known as ordinary Portland cement (OPC or CEM I). This type of cement contains a minimum of 95% Portland cement. Other types of cement such as CEM II, CEM III, CEM IV and CEM V are classified based on the compositions of Portland cement, and materials such as fly ash, blast furnace slag and Pozzolanic materials.

The main chemical compounds in cement react with water forming a bonding agent that surrounds and binds the fine and coarse aggregate particles together. These reactions are exothermic, with the rate of reaction and quantity of thermal energy evolved begin determined by the quantity of cement and its chemical composition. The heat evolved, known as the heat of hydration, is also dependant on the size of the concrete element. Through cement hydration, the paste hardens, resulting in strength gain and loss of free water from the concrete matrix. Within seven days of the concrete being placed, up to 70% of the design strength can be obtained (Domone & Illston, 2010).

2.5.2   Aggregates for Concrete

Aggregate particles normally contribute between 65% and 85% by volume of hardened concrete (Marshall, 1972). While advancements in concrete technology have resulted in reductions of aggregate proportions and increased variety of aggregate types used in the production of concrete, the large volumetric proportion and mineralogy of aggregates typically determines the mechanical, and thermal characteristics of the hardened concrete while physical properties such as density, ρ, determine the corresponding properties of the hardened concrete. The scope of this study is limited to thermal properties which include thermal expansion, specific heat and thermal conductivity. The thermal characteristics of aggregates and concrete are discussed in Section 2.6.

Aggregates are derived as mechanically crushed stone or naturally weathered from solid rock and are classified according to the manner in which the parent rock was formed. The common aggregate groups are thus igneous, sedimentary and metamorphic rocks. In South Africa, the most used aggregates include quartzite, dolerites and dolomitic rocks, basalts, granite and tillite (Addis, 1986). In recent times, there has been an increase in the use of lightweight, synthetic, and recycled aggregates for specific applications, mostly to achieve sustainability demands (Owens, 2009)

Aggregates can also be classified according to their particle shape and size. When classification is done in accordance to particle size, aggregates are divided into two groups, namely coarse aggregates or stone with sizes ranging from 6.7 mm to 37.5 mm, and fine aggregates or sand with a maximum particle sizes less than 4.75 mm. The grading, particle shape, and particle size have an influence on the properties of fresh concrete (workability), hardened concrete, as well as the durability of concrete. For example, using small, well-graded aggregates results in an efficiently packed concrete will low void content. The mechanical, thermal, and durability characteristics of such concrete will be largely uninfluenced by the properties of voids and are thus predictable (Kearsley, 2017).

2.5.3 Water in Concrete

Water is required for the cement hydration reactions to occur. The quantities of cement and water are related by the water-to-cementitious materials ratio. This ratio is used in the design of concrete mixes to optimise strength, workability and durability. Increasing water content leads to a more workable concrete that is easier to place while reducing water content usually results in higher compressive strength due to the reduced porosity of the final concrete product (Domone and Illston, 2010).

When excessive mixing water is provided or inadequate compaction takes place during placement, large volumes of entrapped air remain in the concrete after it is dried. It is known that the addition of 1% air by volume results in a reduction of up to 6% of the compressive strength (Neville and Brooks, 1987). The increased quantity of air voids also results in a reduction of thermal conductivity of dry concrete and subsequent increase when the same concrete is wetted due to water replacing the air voids. The loss of water before cement hydration can be mitigated through the selection of an appropriate curing regime. Curing is the process by which concrete is protected from moisture loss during the first 28 days after placement. Various methods, including submersion in water, water misting, covering with plastic sheeting and direct exposure to the environment are used. The selection of a curing regime is dependent on the element type, location, construction, and economic demands.

2.6   Thermal Properties of Concrete

In most published works the concrete material is classified as a thermal conductor, that is, as having a positive response to external thermal energy (Marshall, 1972). In order to understand the thermal behaviour of concrete, it is important to form an understanding of the thermal characteristics of the composite material as well as its constituent elements. Aggregate particles can make up between 60% and 85% by volume of concrete. Therefore, the thermal characteristics of aggregates largely determine the characteristics of the final composite.

This section presents the thermal properties of normal-weight concrete and its constituents. The properties that are of primary interest are the specific heat (c), thermal conductivity (k), thermal diffusivity (h^2), and thermal expansion coefficient (α). Thermal inertia or thermal mass, a geometric property, is briefly discussed. It is known that these complex properties vary with age, temperature, and humidity, thus the information presented in this chapter is qualified on the basis of the conditions under which it was obtained. The thermal characteristics are enumerated and discussed from three approaches: the hardened cement paste, the aggregates, and the composite mass concrete material.

2.6.1   Density

The density of concrete is influenced mostly by the unit weight and volumetric proportion of the coarse aggregate or stone used in production. Typically, aggregates with high bulk density are used as they result in more economical mix proportions and improved compressive strength. The density of concrete, together with water content and temperature, has a significant influence on the thermal conductivity. Increasing density will tend to increase the thermal conductivity of a specific concrete (Tatro, 2006).

The relative density of typical South African aggregates used for the production of normal-weight concrete is shown in Table 2-1. The bulk density can be determined by multiplying the relative density by 1000 kg/m^3 (the reference density of water at room temperature). For normal-weight concrete produced with South African aggregates, the density ranges between 2400 kg/m^3 and 2600 kg/m^3 while the density of a specific concrete will moderately increase with increasing moisture content (Alexander, 2014).

Table 2-1: Relative density of South African aggregates (Adapted from Alexander, 2014 and Addis, 1986)

Aggregate type	Apparent relative density
Quartzite	2.69
Quartz	2.70
Granite	2.65
Dolerite	2.86
Dolomite	2.86
Limestone	2.66

2.6.2 Specific Heat

Specific heat as defined by Equation 2-14, is the ratio of the amount of energy required to change the temperature of 1 kg of a material by 1 °C to the amount of energy required to increase the temperature of 1 kg of water by 1 °C (Tatro, 2006). Typical values of heat capacity for ordinary Portland cement concrete range between 840 J/kg·°C and 1170 J/kg·°C (Neville, 2011). These values are determined through elementary principles of physics.

$$c = q/\Delta T \qquad \text{(Equation 2-14)}$$

where:

c = Specific heat (J/kg·°C)

q = Heat flow (J/kg)

ΔT = Change in temperature (°C)

The specific heat of concrete is largely unaffected by changes in the mineralogy and type of aggregates, however, it increases with increasing mixing water content and in-service moisture content. In the Boulder Canyon studies (USBR, 1940), it was found that specific heat increased from 921 J/kg·°C to 1005 J/kg·°C when mixing water by weight of concrete was increased from 4% to 7%.

The specific heat of mass concrete is directly proportional to temperature over the range of typical ambient air temperatures as shown in Table 2-2, which shows the average values determined from several concrete mixtures with different aggregate types, while the specific heat of aggregates and hydrated cement paste continue to vary with temperature up to 400 °C and 1000 °C respectively (Harmathy and Allen, 1973). For design purposes at ordinary temperatures, the specific heat of concrete made with normal-weight and light-weight aggregates can be assumed to be 940 J/kg·°C.

Table 2-2: Typical variation of concrete specific heat with temperature (Adapted from Tatro, 2006)

Temperature (°C)	Specific heat (J/kg·°C)
10	917
38	971
66	1038

2.6.3   Thermal Conductivity

Conductivity is defined as the ratio of heat flux to the temperature gradient across a unit length in W/m·°C or J/m·s·°C, where heat flux is the rate of energy flow per unit area per unit time. This property determines the rate of heat gain and loss, as well as the thermal amplitude (temperature) attained by a concrete element. The conductivity of concrete is influenced by the mineralogy and quantity of aggregates (Marshall, 1972; Kim et al., 2003; Tatro, 2006). The thermal conductivity of both the hydrated cement paste and the mature concrete are largely dependent on fluctuations in moisture content, however, the conductivity of cement paste is independent of the initial mixing water content (Campbell-Allen and Thorne, 1963). The conductivity of air is approximately twenty times lower than that of water, thus a higher moisture content increases conductivity and concrete designed with lower mixing water content will have higher conductivity due to the reduction in air voids. The following section presents a discussion of the conductivity of the constituents, which is necessary to develop a comprehensive understanding of thermal conductivity in the composite concrete material.

Conductivity of rocks and minerals

The thermal conductivity of aggregates is determined by the mineralogy of the parent rock and is independent of formation and location as rocks from different sources with similar mineral compositions have similar conductivities (Marshall, 1972). This is shown in Table 2-3 which lists the conductivities of dry rocks and rock-forming minerals as published by different researchers (USBR, 1940; Robertson, 1988; Cavanaugh et al., 2002; Kim et al., 2003; Côté and Konrad, 2005). The size and shape of aggregate particles also influence conductivity. In most published work, thermal conductivity was determined using crushed aggregates. Although the crushing process produces aggregates with random fracture planes, it has been assumed that the aggregates, which act as a randomly dispersed filler material in cement mortar, would retain the thermal characteristics of the parent rock (Khan, 2002). Some aggregates, such as those containing carbonates, display a reduction in conductivity with increasing temperature, while diabase (dolerite) rocks display little increase or no change at all (Marshall, 1972).

Table 2-3: Thermal conductivities of rocks and granular materials (Adapted from various researchers)

Material	Relative density Côté and Konrad (2005)	Thermal conductivity (W/m·°C)				
		USBR (1940)	Robertson (1988)	Cavanaugh et al. (2002)	Kim et al. (2003)	Côté and Konrad (2005)
Rocks						
Basalt	2.90	1.47	1.70	1.4 - 2.2	2.47	1.70
Diabase	2.98		2.40	2.25		2.30
Dolomite	2.90	3.70	2.99			3.80
Gabbro	2.92	2.90	2.06			2.20
Gneiss	2.75					2.60
Granite	2.75	2.50	2.87	1.9 - 4.0	2.5 – 2.65	2.50
Limestone	2.70	2.78	1.80	1.0 - 3.0	2.29 – 2.78	2.50
Marble	2.80	2.11	2.80	2.0 - 6.0	2.11	3.20
Quartz		4.45		5.80	4.45	
Quartzite	2.65		2.93	3.2 – 5.3		5.00
Sandstone	2.80		2.70	1.3 -2.3		3.00
Schist	2.65		2.40			1.50
Shale	2.65		2.60			2.00
Soil and organic matter						
Coal	1.35					0.26
Silt and clay	2.75					2.90

Conductivity of hardened cement paste

Investigations into the thermal conductivity of hardened cement paste have been conducted since the early 1930s during the Boulder Canyon studies (USBR, 1940). Measurement of conductivity in hardened cement paste is difficult due to its complex physical structure and the presence of capillary and pore water (Marshall, 1972). Conductivities ranging between 1.1 W/m·°C and 1.3 W/m·°C, with an average value of 1.2 W/m·°C were measured in moist cement pastes with water-to-cementitious materials ratios ranging from 0.3 to 0.6 (Campbell-Allen and Thorne, 1963; Lentz and Monfore, 1966). The conductivity of cement paste increases with increasing moisture content and also increases linearly with temperature up to 30 °C at constant moisture content. Increasing mixing water results in cement paste with lower conductivity which is further reduced when the cement paste is dried. This due to water replacing air voids in the concrete during wetting and the opposite occurring during drying. Water has a conductivity that is many times that of air and varies with temperature as shown in Table 2-4 (Rhodes, 1978; Kim et al., 2003) while the effect of mixing water content is shown in Table 2-5 (Yuan et. al, 2012). While it is not within the scope of this study, it is of interest to note that the increased use of polymer and steel fibres in concrete has resulted in more variable concrete properties. Recent studies have found that conductivity in pastes containing graphite fibres increases linearly with up to three times that of neat cement paste at 15% content by volume at constant water/cement ratio.

Table 2-4: Thermal conductivity of water (Kim et al., 2003)

Temperature (°C)	Thermal Conductivity (W/m·°C)
0	0.494
10	0.507
20	0.521
30	0.533
40	0.545

Table 2-5: Effect of initial water content and heating on cement paste conductivity (Yuan et al., 2012)

Water/cement ratio	Thermal Conductivity (W/m·°C)	
	Before heating	After heating
0.30	0.741	0.405
0.33	0.65	0.392
0.36	0.562	0.349
0.40	0.483	0.338

Conductivity of concrete

Normal-weight concrete can consist of up to 85% aggregates by volume. Therefore, the thermal characteristics of aggregates largely determine the characteristics of the final composite material. The conductivity of porous materials such as concrete can be determined in a laboratory in accordance with the ASTM C177 or ASTM C 236 test methods (Cavanaugh et al., 2002). Steady-state methods such as the hot box test or the flat plate test yield similar results for dry concrete, however, they underestimate the conductivity of moist concrete due to moisture movement into the dry test environment. Transient methods such as the hot wire test are more suitable for moist concrete (Brewer, 1967; Neville, 2011). Typical values of the conductivity of moist concrete are shown in Table 2-6, where it can be seen that conductivity increases as aggregates increase in crystalline mineralogy and as the concrete density increases.

Table 2-6: Conductivity of concrete made with various aggregates (Tatro, 2006)

Aggregate type	Wet density (kg/m^3)	Conductivity (W/m·°C)
Hematite	3040	4.10
Quartzite	2400	4.10
Quartzite	2440	3.50
Dolomite	2500	3.30
Quartzite	-	3.30
Limestone	2450	3.20
Quartzite	2350	3.10
Sandstone	2130	2.90
Sandstone	2400	2.90
Granite	2420	2.60
Limestone	2420	2.60
Marble	2440	2.20
Limestone	2440	2.20
Basalt	2520	2.00
Rhyolite	2340	2.00
Barite	3040	2.00
Dolerite	2350	2.00
Basalt	2350	1.90
Expanded Shale	1590	0.85

Influence of moisture

In-service concrete seldom exists in a moisture-free condition thus when using calculated values or oven-dry measurements of conductivity, corrections should be made for moisture effects (Valore, 1958; Tatro, 2006). Table 2-7 shows the variation of thermal conductivity with moisture content at normal working temperatures for concrete produced with various aggregate types. It can be seen that the conductivity of concrete increases with moisture content for all aggregate types.

Table 2-7: Typical variation in thermal conductivity with moisture (Tatro, 2006)

Aggregate type	Moisture Condition	Conductivity (W/m·°C)
Limestone	Moist	2.2
	50% relative humidity	1.7
	Dry	1.4
Sandstone	Moist	2.9
	50% relative humidity	2.2
	Dry	1.4
Quartz gravel	Moist	3.3
	50% relative humidity	2.7
	Dry	2.3
Expanded shale	Moist	0.85
	50% relative humidity	0.79
	Dry	0.62

Where measured data for conductivity at various moisture conditions is unavailable, it is necessary to make use of prediction models. Valore (1980) developed a method for estimating the oven-dry conductivity of concrete (Equation 2-15). It was found that the equation was suitable for concrete with dry densities ranging from 320 kg/m^3 to 1600 kg/m^3, however, this equation did not account for varying mineralogy at constant dry density.

To account for variations in moisture content, it was proposed that conductivity should be increased by 6% for every 1% of moisture by weight as shown in Equation 2-16. When concrete is used in vertical elements such as walls, Equation 2-15 was modified by a factor of 1.2 to account for an average 20% moisture increase in air-dry, in-service concrete. The resulting formulation is shown in Equation 2-17.

$$k_c = 0.072e^{0.00125\,\rho_d} \hspace{4cm} \text{(Equation 2-15)}$$

where:

k_c = Thermal conductivity of oven-dry concrete (W/m·°C)

ρ_d = Oven-dry density (kg/m³)

$$k_{c\,\text{corrected}} = k_c \cdot \left[1 + \frac{(6\rho_m - \rho_d)}{\rho_d} \right] \hspace{2cm} \text{(Equation 2-16)}$$

where:

k_c = Thermal conductivity of oven-dry concrete (W/m·°C)

ρ_d = Oven-dry density (kg/m³)

ρ_m = Density in moist condition (kg/m³)

$$k_c = 0.0865e^{0.00125\,\rho_d} \hspace{4cm} \text{(Equation 2-17)}$$

where:

k_c = Thermal conductivity of oven-dry concrete (W/m·°C)

ρ_d = Oven-dry density (kg/m³)

Valore (1980) also developed the cubic model, shown in Figure 2-5, in which it was assumed that concrete is a two-phase material consisting of cement paste and aggregate particles. The conductivity of the composite material could thus be calculated from the volumetric fractions of the phases. This model was appropriate for concretes with dry density above 1600 kg/m³. In this model, it was assumed that the composite concrete material was a cube of unit volume consisting of a smaller cube of aggregate with volume V_a insulated by a layer of cement paste.

The oven-dry conductivities of concrete based on the cubic model could be calculated in accordance with Equation 2-18 and were in good agreement with measured data for normal-weight concrete. Additionally, these calculated oven-dry conductivities could be modified for moisture effects using Equation 2-16.

2-23
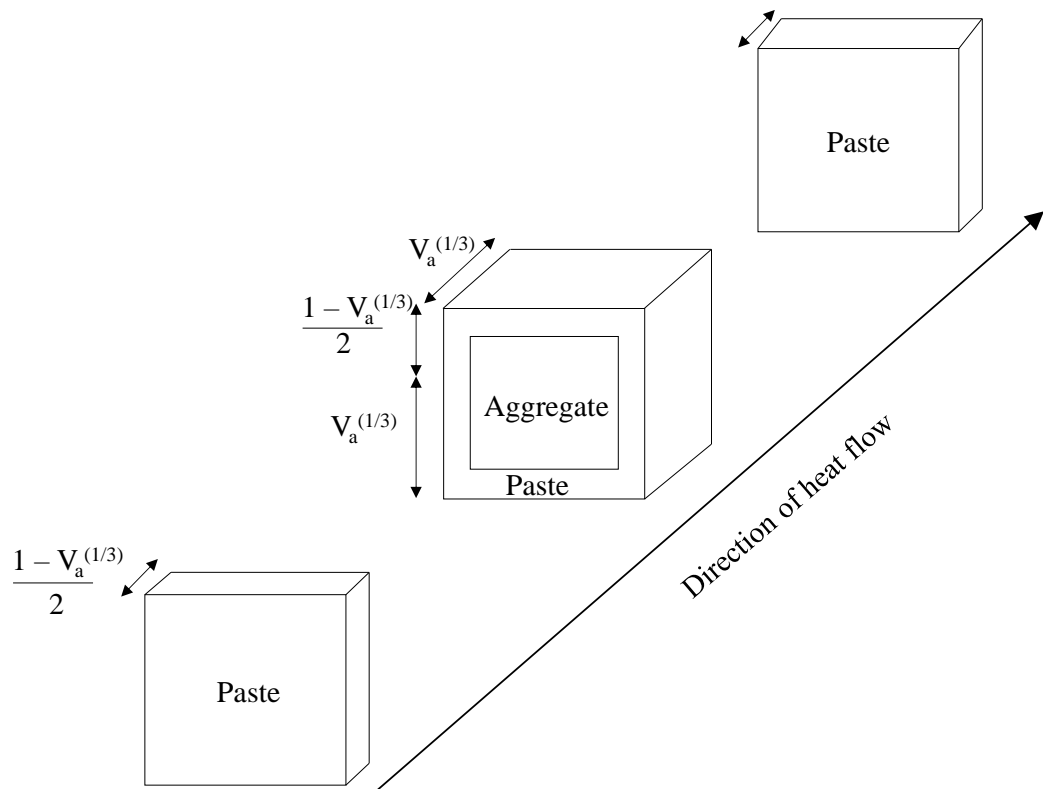
Figure 2-5: Cubic model for concrete thermal conductivity (Redrawn from Valore, 1980)

$$k_c = k_p \cdot \cfrac{V_a^{2/3}}{V_a^{2/3} - V_a + \left(\cfrac{V_a}{\left(\cfrac{k_a V_a^{2/3}}{k_p}\right) + 1 - V_a^{2/3}}\right)} \qquad \text{(Equation 2-18)}$$

where:

k_c = Thermal conductivity of oven-dry concrete (W/m·°C)

k_p = Thermal conductivity of hardened cement paste (W/m·°C)

k_a = Thermal conductivity of aggregate (W/m·°C)

V_a = Volume fraction of aggregate

2.6.4 Thermal Diffusivity

Thermal diffusivity represents the rate at which temperature change occurs across a temperature gradient and is a function of conductivity, specific heat and density as shown in Equation 2-19. When thermal diffusivity is calculated for design purposes, the values of the parameters used should represent the condition of in-service concrete. Thermal diffusivity can be determined experimentally by measuring the time required for the interior temperature of a sample to become equal to the outer surface temperature. Common test methods include the flat plate and hot box test (Neville, 2011).

$$h^2 = k / \rho \cdot c$$
<div align="right">(Equation 2-19)</div>

where:

h^2 = Diffusivity (m^2/h)

k = Thermal conductivity (J/m·°C)

ρ = Density (kg/m^3)

c = Specific heat (J/kg·°C)

Thermal diffusivity varies according to the different influences on conductivity, specific heat, and density. The thermal diffusivity of cement paste increases moderately with moisture content as both conductivity and specific heat increase with moisture content (Marshall, 1972). The Boulder Canyon studies (USBR, 1940), found that thermal diffusivity ranged from 0.0012 m^2/h to 0.0016 m^2/h at room temperature, with negligible variation over typical working temperatures. The diffusivity of concrete is largely determined by the volume and mineralogy of the coarse aggregate, with values ranging from 0.00186 m^2/h to 0.00744 m^2/h for basalt and chert aggregates respectively (USBR, 1940), while values for normal-weight and light-weight aggregates are shown in Table 2-8.

Table 2-8: Typical thermal diffusivity of aggregates for concrete (Adapted from Tatro, 2006)

Aggregate type	Thermal diffusivity (m^2/h)
Quartz	0.0079
Quartzite	0.0061
Limestone	0.0055
Basalt	0.0025
Expanded shale	0.0015

2.6.5 Thermal Expansion

Thermal expansion is a measure of the volumetric response of a material to temperature change. Concrete has a positive coefficient of thermal expansion thus it expands when the temperature increases and contracts when the temperature decreases. This quantity is influenced by concrete mix proportions, aggregate type and moisture content. The coefficient of thermal expansion of most aggregates is lower than that of hardened cement paste. Thus the thermal expansion of concrete decreases with increasing aggregate content as shown in Figure 2-6 (Neville, 2011).
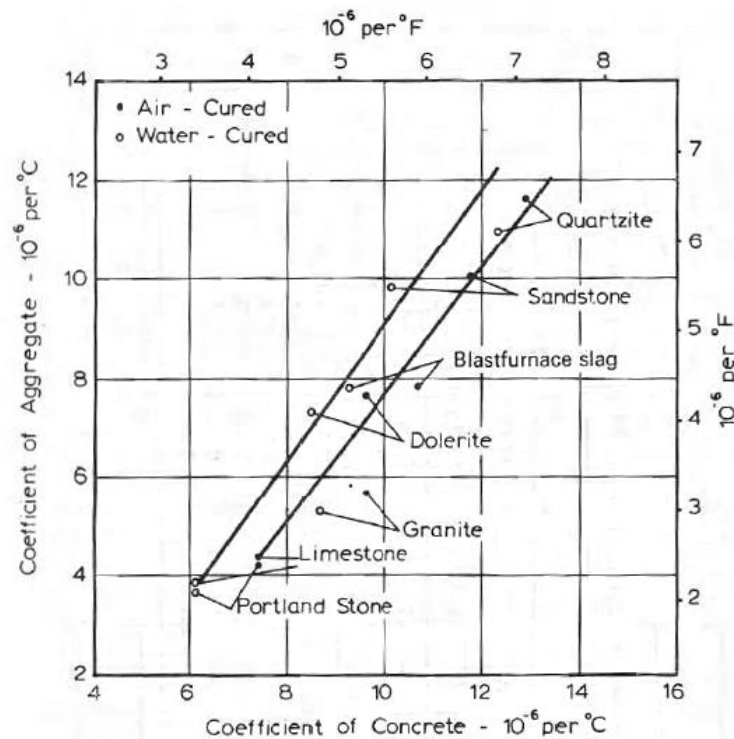
Figure 2-6: Influence of aggregate type on thermal expansion coefficient of concrete (Neville, 2001)

The coefficient of thermal expansion is of interest in structures where large temperature gradients are present or where the possibility of thermal shock exists. For example, in concrete roof slabs where the top is at a higher temperature than the bottom, the top expands more than the bottom resulting in curling, warping and the opening and closing of crack and joints. Thermal shock can occur when the interior (core) and surface temperatures of a structural element differ by 50 °C or more (Cavanaugh et al., 2002). The most widely used test method for determining the coefficient of thermal expansion is the AASHTO T336-11 in which the change in length of a saturated cylinder is measured when the temperature is increased from 10 °C to 60 °C.

The coefficient of thermal expansion is highly dependent on the test method and sample size used. Marshall (1972) stated that large samples required longer times before a thermal equilibrium was

achieved and during this time, changes could occur to the material structure and dimensional changes could occur in small samples due to moisture exchange with the atmosphere if measurements were not recorded in the saturated state (submerged in water). In these extreme cases, there would be an underestimation or overestimation of the expansion coefficient. Table 2-9 shows the coefficient of thermal expansion for concrete produced with various aggregates.

Table 2-9: Coefficient of thermal expansion of concrete by aggregate type
(Adapted from Hall and Tayabji, 2011)

Primary aggregate class	Average CTE(/°C x 10^{-6})	Standard deviation (/°C x 10^{-6})
Andesite	7.78	0.75
Basalt	7.8	0.77
Chert	10.83	0.75
Diabase	8.35	0.94
Dolomite	8.92	0.73
Gabbro	8.00	0.75
Gneiss	8.77	0.15
Granite	8.50	0.71
Limestone	7.80	0.94
Quartzite	9.34	0.90
Rhyolite	6.91	1.47
Sandstone	9.58	0.94
Schist	7.98	0.70
Siltstone	9.03	0.56

Influence of moisture

In-service concrete rarely exists in the oven-dry or saturated state. The influence of moisture content applies mostly to the hardened cement paste, however, it is mitigated by coarse aggregates which often have low water retention properties, that is, porosity and permeability (Hall and Tayabji, 2011). The coefficient of thermal expansion is lowest when the cement paste moisture content is at a minimum (oven-dry) or maximum (saturated), while it is the highest at a relative humidity of approximately 70% as shown in Figure 2-7 (Neville, 2011).
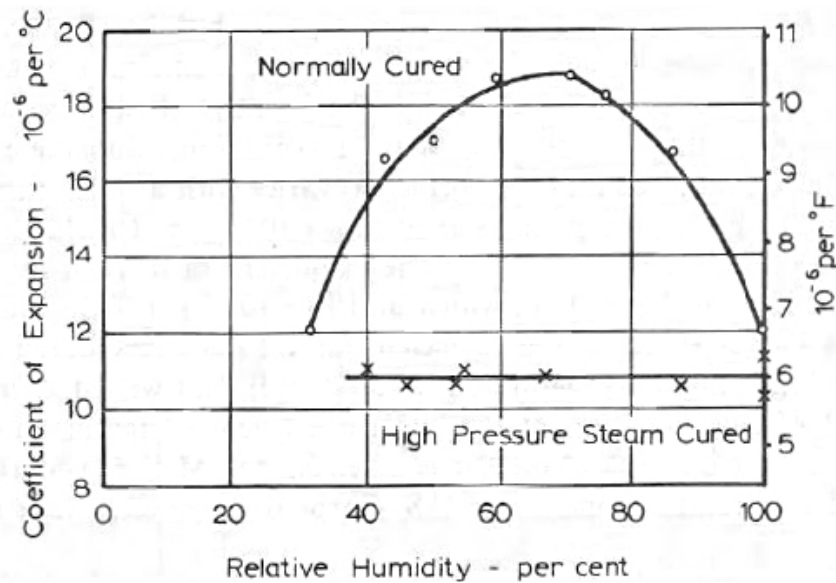
Figure 2-7: Influence of ambient relative humidity of expansion coefficient (Neville, 2011)

2.6.6 Summary of Thermal Properties of Concrete

The relative effects of major variables on the thermal properties of concrete are shown in Table 2-10 while the properties are best summarised by reiterating some of the conclusions determined by the Boulder Canyon studies (USBR, 1940):

- Thermal properties of concrete are not affected by age.
- Rock type of coarse aggregate is the most important variable affecting conductivity.
- Original water content has much less effect on the conductivity than the type of coarse aggregate. Increasing (mixing) water content produces decreased conductivity.
- High conductivities decrease with an increase of temperature, average conductivities show little change with variation of temperature, and low conductivities increase with an increase of temperature.
- Rock type of coarse aggregates produces small variation in specific heat.
- Specific heat varies with original water content. This variation, per unit of weight, is several times greater than for other materials. However, since the variation in weight of water is limited, the total effect of varied water content is limited to about 10%. Specific heat increases as water content increases.
- Specific heat increases as temperature increases.
- Diffusivity varies over a wide range due to change in rock type.
- Diffusivity decreases as (original) water content increases.
- Diffusivity decreases as temperature increases.

Table 2-10: Relative effects of major variables on the thermal properties of concrete (USBR, 1940)

Test conditions	Conductivity	Specific heat	Diffusivity
Type of coarse aggregate varied through range of tests	Varied as much as 41%	Varied as much as 8%	Varied as much as 47%
Water content increased from 4% to 8% of the concrete weight	Decreased as much as 10%	Increased as much as 12%	Decreased as much as 16%
Mean temperature of concrete increased from 10% to 65%	Increased as much as 12% and decreased as much as 6%	Increased as much as 24%	decreased as much as 21%

2.7   Thermal Inertia

Thermal inertia or thermal mass describes the ability of a material to absorb and store significant amounts of thermal energy. Concrete is a thermal mass material, which warms and cools slowly, and maintains warm (or cool) internal temperatures for long time periods. As such, the thermal inertia of concrete is of interest in the transient analysis of structural behaviour. The thermal mass effect is observed as a lag in heat transfer, which results in a reduction of the total heat gain or loss through a concrete element as shown in Figure 2-8. The lag indicates that the material stores thermal energy and later releases it into the surrounding environment. This property is beneficial where concrete is used in buildings, as outdoor temperature cycles have a reduced effect on indoor temperatures and the thermal mass results in increased structural and indoor temperatures at night (Cavanaugh et al., 2002).

The thermal mass effect is dependent on several factors, which include the amount of concrete, insulation, orientation, and climate. Some thermal properties described earlier in this chapter can be used to determine thermal mass (Cavanaugh et al., 2002):

- *Thermal diffusivity* is a measure of how rapidly a material changes temperature. A high diffusivity indicates fast heat transfer and minimal storage, while low diffusivity indicates slower heat transfer and larger quantities of heat storage. Concrete, which has low diffusivity, is an effective thermal mass material.

- *Heat capacity* is also used in several design codes as an indicator of thermal mass. Concrete absorbs heat slowly thus it has a high heat capacity. Heat capacity is a product of mass per unit area and specific heat measured in $J/m^2 \cdot °C$.

- The *thermal resistance* (R-value), or *thermal transmittance* (U-value) are used to specify the thermal mass requirements of building thermal envelopes. Concrete elements exhibit superior thermal performance than other materials with the same R-value, as these properties are determined under steady-state temperature conditions.

- The *thermal performance* of a building can be quantified by energy savings made by reducing the demand for electrical heating and cooling in a building.
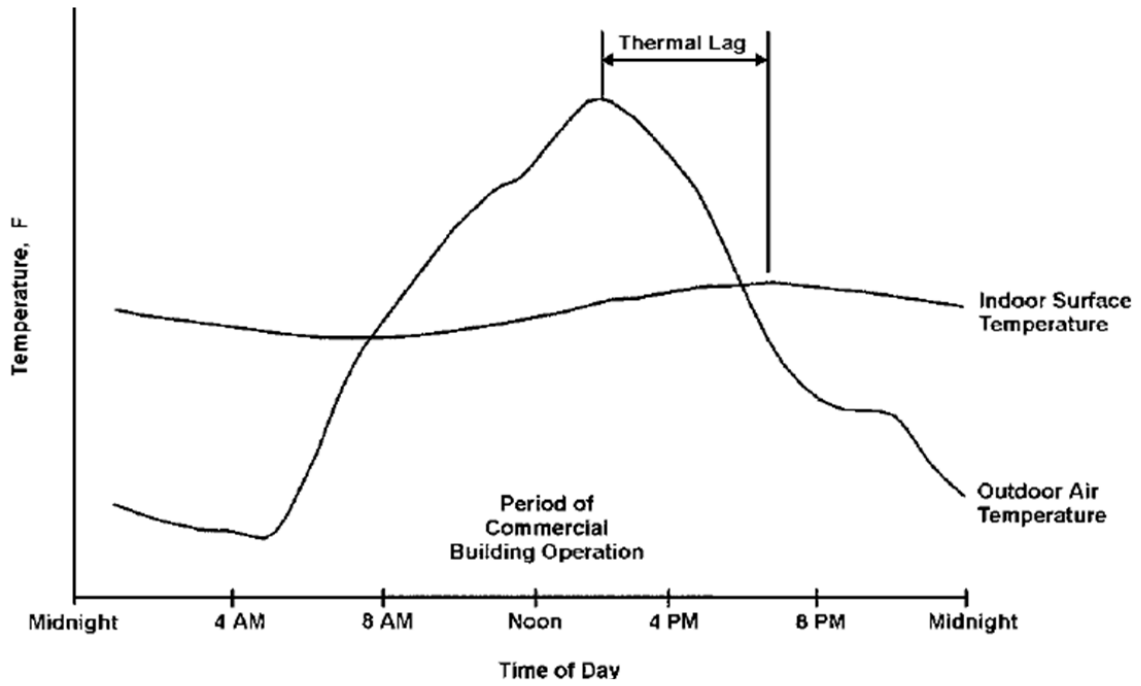
(a)
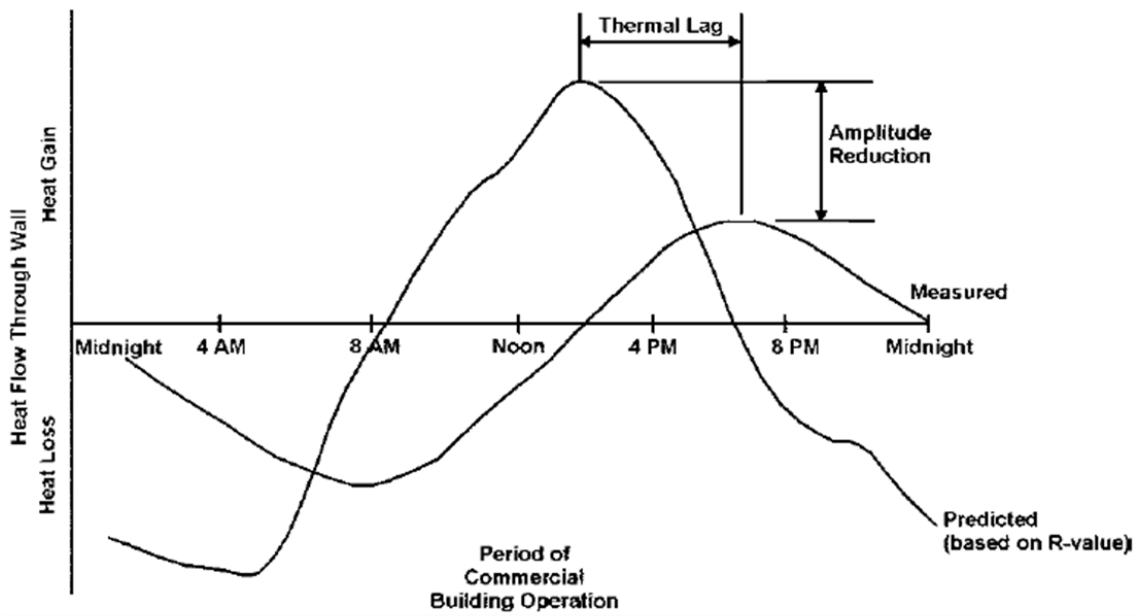
(b)

Figure 2-8: Thermal mass effect on a concrete wall (Cavanaugh et al., 2002)

2.8   Surface characteristics of concrete

In this section, the surface properties of concrete structures and elements that are associated with heat transfer are discussed and enumerated. The properties presented include albedo or reflectivity, solar absorptivity, and emissivity.

2.8.1   Albedo

Solar radiation has the largest effect on the temperature distributions in concrete elements. Air is transparent to light and allows approximately 90% of the visible light and some of the infrared fractions of the electromagnetic spectrum to pass through it. The albedo, or reflectivity, r of a surface is a non-dimensional parameter which represents the ratio of the reflected light to the total available light. That is the quantity of visible light or global radiation that is reflected by the surface. This property is measured relative to the reflectivity of a black body which would absorb all visible light wavelengths on the electromagnetic spectrum. A high albedo value indicates that the surface reflects a large proportion of light and absorbs little energy (Doulos et al., 2004). During the day, the thermal balance of a construction material is determined by the reflection and absorption of solar radiation. The use of high albedo materials results in reduced absorption of thermal energy which is characterised by lower surface and mean temperatures during the day, and lower air temperatures at night as less thermal energy is stored and subsequently released as longwave radiation.

In most engineering applications, the parameter that is used to determine the influence of solar radiation on the thermal energy balance of a surface is the solar absorptivity, α_{SR}. The solar absorptivity can be calculated from the albedo or reflectivity, r using Equation 2-20:

$$\alpha_{SR} = 1 - r \qquad \text{(Equation 2-20)}$$

where:

α_{SR} =   Solar absorptivity

r =   Solar reflectivity

The solar absorptivity of concrete according to published work by several researchers is shown in Table 2-11. Figure 2-9 shows the effect of solar absorptivity or albedo on the surface temperature of some widely used construction materials.

Table 2-11: Solar radiation of concrete (Adapted from several researchers

Author	Albedo	Solar absorptivity
Emerson ,1973	0.2 - 0.5	0.5 - 0.8
Elbadry and Ghali, 1983	0.5	0.5
Potgieter and Gamble, 1989	0.3	0.7
Branco and Mendes, 1993	0.3	0.7
Larsson and Thelandersson, 2011	0.3 - 0.5	0.5 - 0.7
Li et al., 2014	0.26 - 0.29	0.71 - 0.74
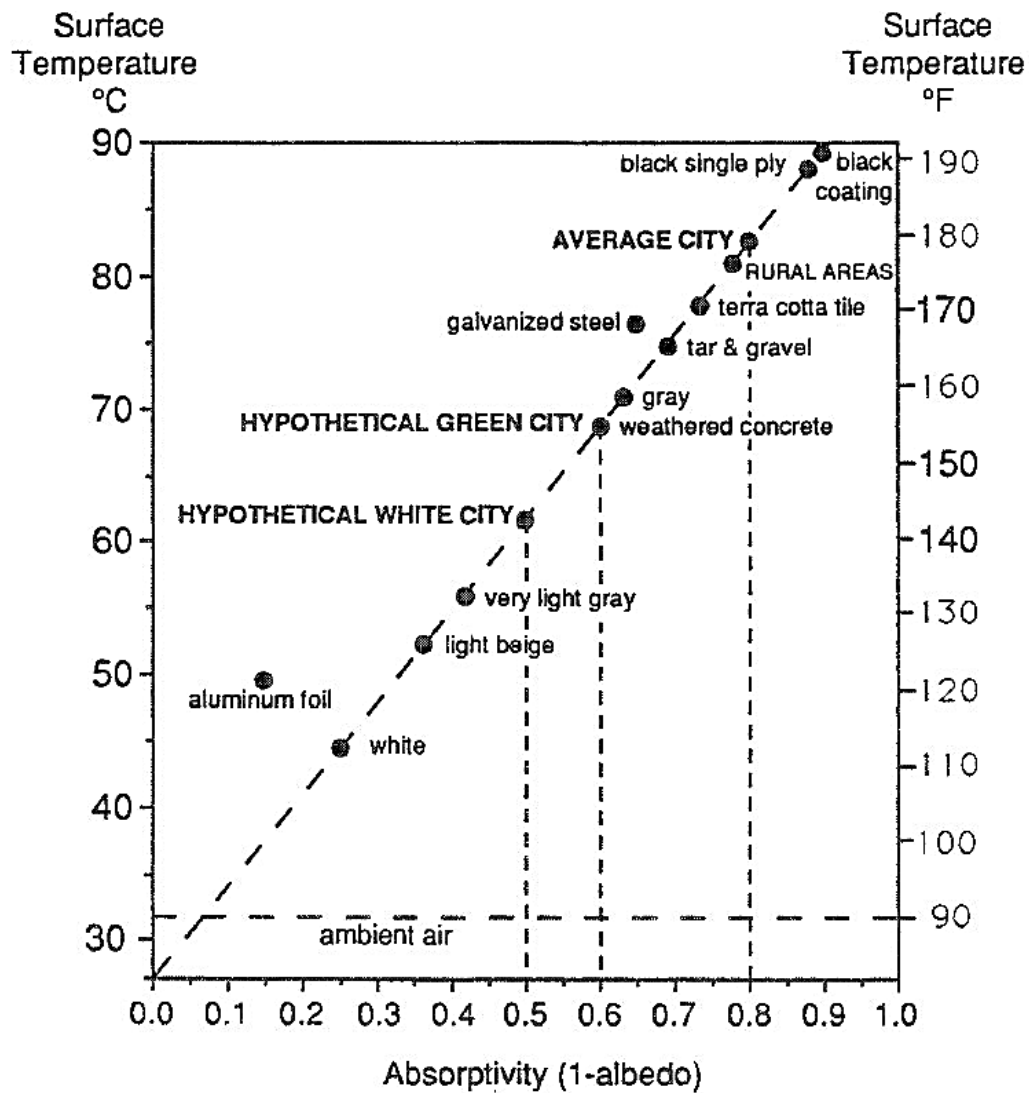
Figure 2-9: Effect of albedo on the temperature of horizontal surfaces (Taha et al., 1992)

2.8.2 Emissivity

Emissivity is defined as the ratio of radiation emitted to radiation emitted by an ideal black body. During the day incoming radiation nullifies heat loss by irradiation however, the thermal energy balance at night is determined by the amount of longwave radiation that is emitted by the surface. Emissivity thus affects minimum temperatures more than maximum temperatures, which are governed by the solar absorptivity. The solar emissivity of concrete according to published work by several researchers is shown in Table 2-12.

Table 2-12: Typical emissivity of concrete (Adapted from several researchers)

Author	Emissivity
Emerson, 1973	0.85 - 0.9
Elbadry and Ghali, 1983	0.88
Branco and Mendes, 1993	0.9
Larsson and Thelandersson, 2011	0.9
Li et al., 2014	0.8

2.9   Design of Concrete Structures for Thermal Actions

Thermal actions contribute to the deterioration of buildings, pavements, and other types of concrete structures as temperature variations contribute to several distress modes including fatigue, deflection, and block cracking. This section presents a discussion of the effect of climatic actions on concrete structures and elements as well as current design guidelines used by bridge, pavement and structural engineers.

2.9.1 Bridge Structures

Concrete bridge structures are subjected to complex environmental loads that include floods and variable thermal loads. Thermal loads are of interest to bridge design engineers due to the typical shape of bridge superstructures. Bridges have large horizontal surface areas that absorb solar radiation and often have varying cross-sections (deep beams and thin flanges). Thermal movement of superstructures is of interest in two instances:

- Where the cross-section varies, greater thermal gradients in flanges would result in large free strains but the flanges are restrained by the deep beams. This can lead to transverse cracking in extreme conditions, and

- In integral structures, where expansion and contraction of the bridge superstructure leads to rotation of the piers and/or abutments. This phenomenon is not common in well maintained simply supported bridge structures as expansion joints and bearings facilitate unrestrained longitudinal movement.

In general, bridge structures undergo three types of temperature induced volume change: uniform expansion of an entire cross-section due to uniform increase in the temperature, linear expansion and contraction whereby volume change occurs equally but in opposite directions around a neutral axis and lastly, non-linear changes due to uneven heating and cooling through a cross-section, (Larsson and Thelandersson, 2011; Elbadry and Ghali, 1983). The linear and non-linear components of expansion cause rotational changes in the form of warping, even in simply supported superstructures. If the element is unrestrained with respect to movement, no stresses will be generated. However, if these movements are restrained, compressive and tensile stresses will be generated in the case of expansion and contraction respectively. In most structural applications, this restraint occurs due to changes in cross-section or thermal gradients.

Several studies have been performed to determine methods of approximating temperature distributions in concrete structures. Most of these methods require hourly ambient air temperature and hourly solar radiation as inputs. Emerson (1973) developed an iterative method for the calculation of temperature distributions in for concrete, steel box, and composite bridge. The method used linear heat flow across the depth and material properties across different layers were assumed to be constant. Emerson's method was developed using conditions in Western Europe, therefore, modifications were required for use in other regions.

The European Standard EN-1991-1-5 (CEN, 2004) provides guidelines on the design of bridge structures for thermal actions. Temperature effects are considered in three parts: uniform components, linear and non-linear temperature difference components in the vertical and horizontal directions, and temperature differences between structural components. The uniform, linear and non-linear components are shown in Figure 2-10. The Swedish national annexe to this European Standard, SS-EN 1991-1-5 (SIS, 2005) recommends design temperatures based on local climatic conditions and provides formulae for the generation of site-specific temperature loads using statistical data.

Uniform component   Linear component   Non-linear component
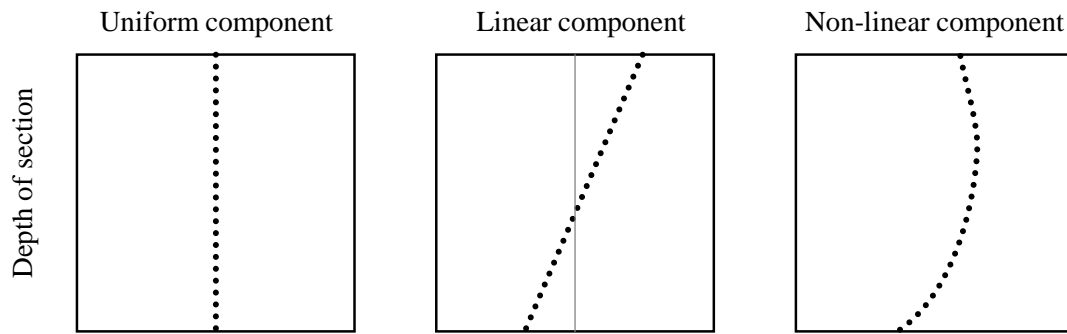
Figure 2-10: Temperature components in a concrete structure

Figure 2-11, adapted from the European Standard EN-1991-1-5 (CEN, 2004), shows the relationship between shade temperatures and effective bridge temperature where the effective bridge temperature is a weighted mean temperature of the cross-section at any given time. The functions shown were developed in studies conducted on bridge structures in the United Kingdom. Of particular interest, is the relationship marked Type 3. This function was developed based on the mean shade and effective bridge temperatures measured over 48 hours on bridges with concrete superstructures.
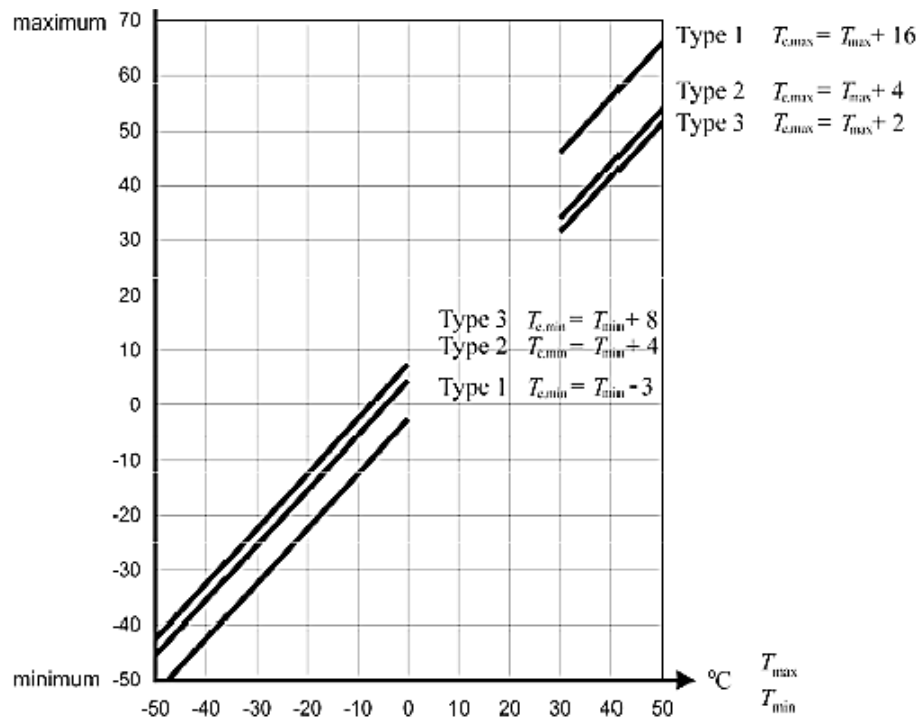
Figure 2-11: Correlation of shade and effective bridge temperature (CEN, 2004)

Temperature differences between components are considered in both the vertical and horizontal directions, however, EN-1991-1-5 (CEN, 2004) does not provide adequate guidelines on conditions for which the horizontal temperature component should be considered for design. The horizontal component is most relevant to the vertical faces of bridge structures where one side is exposed to more global radiation than the opposite face. EN-1991-1-5 (CEN, 2004) specifies a maximum temperature difference of 5 °C between the outer edges of the bridge. The vertical component is more pronounced and temperature differences between the upper and lower surfaces of a bridge are likely to cause differential expansion or contraction of the extreme edges. Additionally, the vertical components may also cause non-linear geometric effects and increase maintenance costs due to the induced friction at rotational bearings.

EN-1991-1-5 (CEN, 2004) provides two methods for the modelling of vertical temperature differences. These methods, Approach 1 and Approach 2, are applicable to concrete, composite and steel bridge superstructures. In Approach 1, a vertical linear temperature gradient is applied to the bridge and cross-sectional stress distributions equivalent to those produced by a non-linear temperature distribution are produced. The linear gradient must be applied with positive and negative gradients. That is, with the top warmer than the bottom, and with the bottom warmer than the top. The recommended temperature differences are shown in Table 2-13. Approach 2 combines the linear and non-linear temperature components with load cases for heating and cooling. The recommended temperature profiles for different concrete bridge cross-sections are shown in Figure 2-12.

Table 2-13: Recommendations for temperature difference components in bridge decks (Adapted from CEN, 2004)

Type of deck	Top warmer than bottom	Bottom warmer than top
	$T_{M,heat}$ (°C)	$T_{M,cool}$ (°C)
Type 1: Steel deck	18	13
Type 2: Composite deck	15	18
Type 3: Concrete deck		
– Concrete box girder	10	5
– Concrete beam	15	8
– Concrete slab	5	8

NOTE 1: The values given in the table represent upper bound values for the linearly varying temperature difference component for representative sample of bridge geometries

NOTE 2: The values given in the table are based on depth of surfacing of 50 mm for road and railway bridges. For other depths of surfacing these values should be multiplied by the factor k_{sur}.
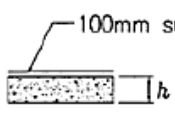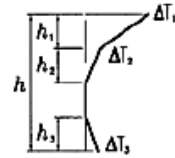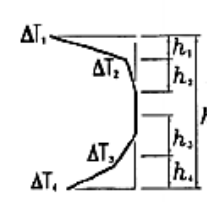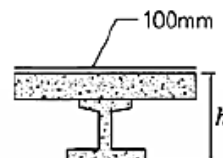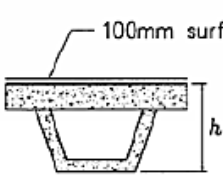
Type of Construction	Temperature Difference (ΔT)	
	(a) Heating	(b) Cooling

Figure 2-12: Recommended temperature distributions for concrete bridges (CEN, 2004)

EN-1991-1-5 (CEN, 2004), specifies that temperature differences should be applied to critical sections between different elements where thermal gradients may cause adverse load effects. The code recommends a maximum difference of 15 °C between structural elements and 10 °C to 20 °C respectively between light-colour and dark-colour suspension/stay cables and bridge superstructures if the surface colours are different.

Calculation of effective temperature

Emerson (1968) defined the effective bridge temperature as the temperature which governs the longitudinal movement of a bridge superstructure and developed a method for the calculation of an effective temperature of a bridge section (See Equation 2-21). The total cross-section was divided along isotherms with the modulus of elasticity of each constituent area assumed to be constant. The effective bridge temperature was calculated by summing the products of the areas and their mean temperature and dividing by the total cross-section area.

$$T_{mean} = \frac{\sum_1^n T_i \cdot A_i}{\sum_1^n A_i}$$
(Equation 2-21)

where:

T_{mean} = Effective temperature (°C)

T_i = Temperature of cross-section area i (°C)

A_i = Area of cross-section area i (m^2)

If the thermal expansion coefficient of concrete is known, the difference between the temperature at any point in the cross-section and the effective temperature could be used to calculate thermal strain and stress using fundamental principles. Temperature induces strain and stress are computed based on one-dimensional elastic beam theory and includes the following assumptions as stated by Thepchatri et al. (1977):

- Temperature variation is constant along the length of the bridge but in any manner over the cross-section;
- Thermal strains vary linearly with temperature changes;
- The principle of superposition is valid;
- Material is isotropic with properties that are independent of temperature, and
- Plane sections remain plane after deformation.

The unrestrained compressive strain due to a positive temperature change in the cross-section is given by Equation 2-22 and the associated stress can be calculated using Equation 2-23:

$$\varepsilon_{x,y} = -\alpha \cdot \Delta T_{xy}$$
(Equation 2-22)

$$\sigma_{x,y} = -\varepsilon_{x,y} \cdot E$$
(Equation 2-23)

where:

ε = Thermally induced strain (m/m)

α = Coefficient of thermal expansion (°C^{-1})

ΔT = Change in temperature (°C)

σ = Thermally induced stress (MPa)

E = Modulus of elasticity (GPa)

2.9.2 Pavement Structures

Pavement temperature distributions are of interest in both flexible bituminous pavements and rigid Portland cement concrete pavements (Williamson and Marais, 1975). Thermal loading is associated with reductions in the stability of bituminous surfaces, resistance to permanent deformation in flexible pavements, and moisture ingress in all types of pavement. However, in concrete pavement structures, thermal variations result in thermal stress due to the restraint of free movement. The restraint is provided by the self-weight of the pavement, the underlying pavement layers and frictional resistance between the concrete pavement layer (slab) and the underlying layers. Curling occurs due to temperature differences between the top and bottom of the pavement as shown in Figure 2-13. Only the linear component of temperature variation is responsible for curling. During summer months, daytime gradients cause downward curling, while upward curling is observed at night.

(a) Downward curling   (b) Upward curling
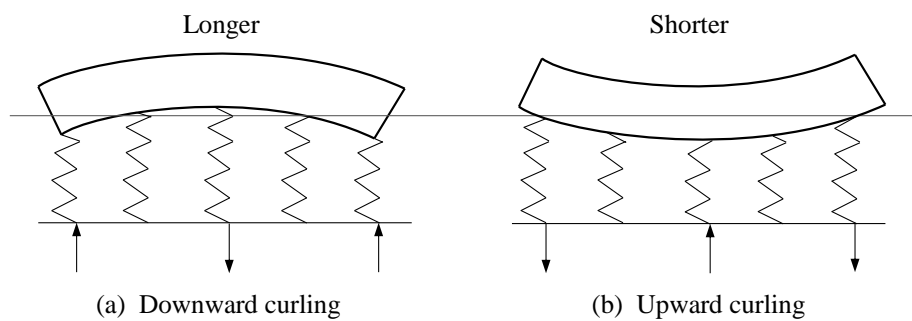
Figure 2-13: Curling of concrete pavement structures (Huang, 2004)

Several studies have been performed to determine approximate values of temperature gradients. These include the Arlington Road test (Teller and Sutherland, 1936), in which the largest recorded temperature difference on a 152 mm slab was 12.2 °C or a gradient of 0.08 °C /mm. In the AASHO Road Test (HRB, 1962), the standard temperature differential was taken as the difference in temperature between points 6.4 mm below the top and 12.7 mm above the bottom of a 165 mm slab. Results of this study found maximum standard differentials in summer of 10.2 °C (0.07 °C/mm) during the day and 4.9 °C (0.03 °C/mm) at night. Although temperature differentials are not proportional to slab thickness, larger thermal gradients are expected for thinner slabs.

A study investigating temperature distributions in asphalt and concrete pavements in Southern Africa was performed by Williamson and Marais (1975). These authors found that the mean temperature range at the surface of concrete pavements varied annually by between 11 °C and 31 °C and that of flexible

pavements varied by 10 °C to 15 °C. The measured temperature gradients in concrete pavements were approximately half of those measured in flexible pavements while the minimum surface temperatures experienced by concrete pavements were higher than those in flexible pavements. The authors attributed this temperature variation to the lower emissivity of mass concrete which was 0.68 compared to 0.87 for bituminous surfaces. A review of the thermal characteristics of concrete indicates that this difference was more likely due to the superior volumetric heat capacity of concrete. The maximum temperature gradients varied between 9 °C and 13 °C, or 0.06 °C/mm to 0.086 °C/mm.

Pavement engineers often assume values of 0.055 °C/mm to 0.077 °C/mm during day-time hours and 0.027 °C/mm to 0.035 °C/mm at night. It is assumed that day-time gradients are twice the magnitude as those seen at night (Huang, 2004). A summary of thermal gradients measured in the studies reviewed above is given in Table 2-14.

Table 2-14: Maximum temperature differentials in concrete pavements

Author	Pavement Depth (mm)	Temperature Differential (°C)	Gradient (°C/mm)
Teller and Sutherland (1936)	152	12.2	0.08
Highway Research Board (1962)	165	10.2	0.07
Williamson and Marais (1975)	150	9 to 13	0.06 to 0.086
Huang (2004)	-	-	0.055 to 0.077

2.10 Cracking in Concrete

From the time of placement and throughout their service life, concrete structures and elements are subjected to various degrees of volume change that are dependent on material composition, geometry and exposure conditions (Tatro et al., 2007). Uniform volume changes do not cause cracking if the concrete element is relatively free to undergo volumetric changes. However, this seldom occurs in practice as restraint is provided either internally by temperature and moisture gradients or eternally by changes in geometry, stiffness and fixity. Restraint induces both tensile and compressive strains, however, it is the tensile strains and corresponding stress that result in cracking when the tensile strain capacity or strength of concrete is exceeded (Tatro et al., 2007).

In the ultimate limit state design of reinforced concrete it is assumed that concrete has no tensile strength, however, tensile strength is of great importance when designing concrete for tensile stresses due to internal restraint. The tensile strength of concrete is determined by the concrete splitting test and is known to develop at the same rate as the compressive strength albeit much lower in magnitude. The tensile strength is highly dependent on the properties, size, and shape of the aggregate used. The development of tensile stress in a restrained concrete section is shown in Figure 2-14 (Neville and Brooks, 1987). Immediately after the concrete has been placed, the modulus of elasticity is insignificant thus volume changes occur without the development of stress. As the concrete gains strength and stiffness, volume changes occur with an associated induced stress. At early ages, creep or stress relaxation relieves thermally induced and drying shrinkage stresses in large and small concrete elements respectively. This stress relieving effect can be understood as the effective reduction of the modulus of elasticity and reduces with age resulting in the formation of cracks when the net tensile stress exceeds the tensile strength of the concrete. The two forms of internal restraint are discussed in the following sections.
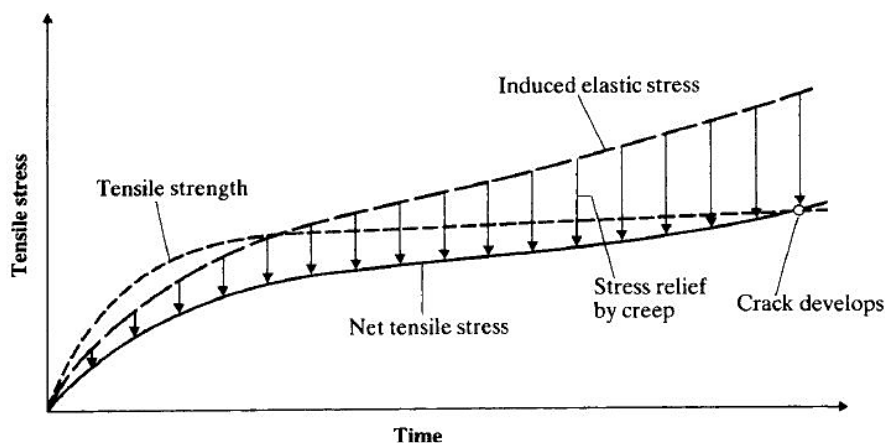
Figure 2-14: Development when tensile strength due to restrained shrinkage (Neville and Brooks, 1987)

2.11 Shrinkage in Concrete

In concrete structures, shrinkage refers to the transient reduction in volume due to the loss of water. This process occurs in several ways including cement hydration and moisture movement from the cement paste matrix that occurs after the hydration process begins, at a rate that is initially high and decreases with time as shown in Figure 2-15. There are four main types of shrinkage, namely: plastic, autogenous, carbonation and drying shrinkage (Gibranik et. al, 2013). In this study, only autogenous and drying shrinkage are discussed.
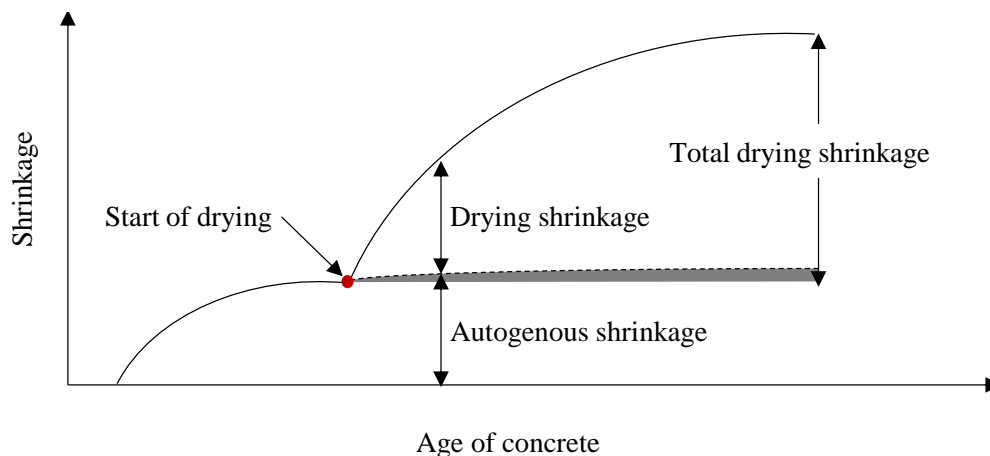
Figure 2-15: Shrinkage in concrete (Adapted from Gribniak et al., 2013)

Autogenous shrinkage

This is the early age shrinkage that occurs due to the loss of capillary water that is required to satisfy the cement hydration reaction water demand. The rate of autogenous shrinkage is increased by increasing cement content (Gibranik et.al, 2013).

Drying shrinkage

Barth et al. (2001) defined drying shrinkage as the time-dependent linear strain on an unloaded concrete element. In unrestrained structures, the total shrinkage with time is referred to as free shrinkage. A typical value for free shrinkage (total shrinkage) in concrete structures is 600 x 10^{-6} m/m while the

tensile strain capacity is approximately 150×10^{-6} m/m, indicating that cracking would occur if the free shrinkage is restrained (see Figure 2-16).
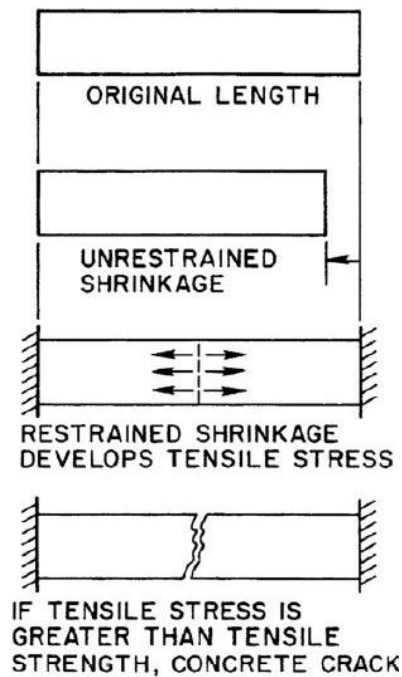
Figure 2-16: Cracking of concrete due to drying shrinkage (Barth et al., 2001)

Prior to moisture equilibrium being achieved, internal shrinkage restraint occurs due to non-uniform shrinkage or moisture gradients. This internal restraint results in the development of internal stresses with tension on the surfaces and compression on the interior (core) of the concrete element (Barth et al., 2001), with up to 30% of free shrinkage occurring within 14 days after the concrete is placed. Shrinkage cracking occurs when the tensile stresses are not relieved by creep and exceed the tensile capacity of the concrete. Several factors including initial water content, water-to-cementitious materials ratio, aggregate type, surface area-to-volume ratio, and relative humidity influence the quantity of free drying shrinkage.

Relative humidity has a large effect on the rate and amount of drying shrinkage that occurs. Troxell et al.,(1958) showed that the rate and quantity of drying shrinkage increased with decreasing relative humidity due to a large moisture gradient between the concrete and the surrounding environment, while concrete that was continuously exposed to water expanded or swelled (See Figure 2-17). However, the amount of swelling is small in comparison to that of shrinkage. In practice, a variety of curing methods are used to prevent the excessive loss of moisture at early ages.
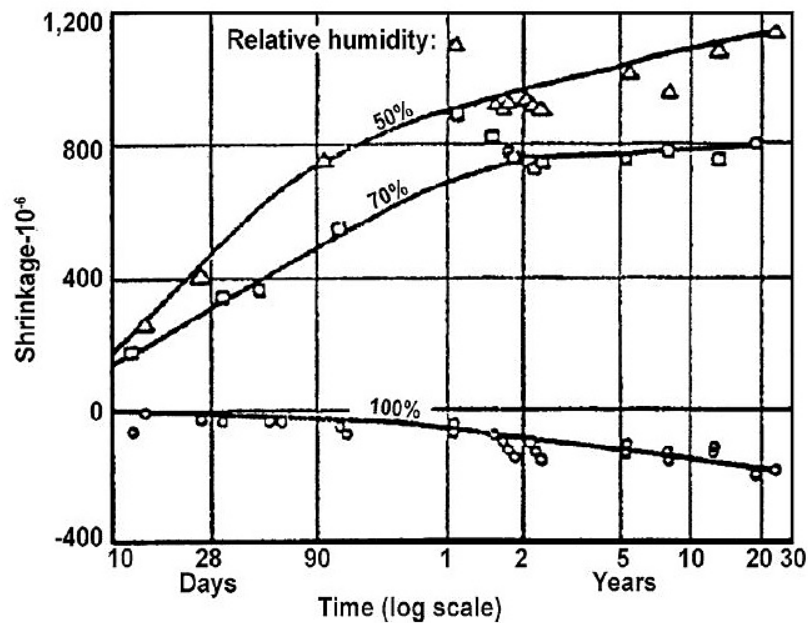
Figure 2-17: Effect of relative humidity on drying shrinkage (Troxell, et al., 1958)

The shape and size of a concrete element have an influence on the amount of drying shrinkage that occurs. Elements with a high surface area to volume ratio, which is indicative of a short migration path for moisture, such as pavements and slabs are susceptible to excessive drying shrinkage. The quantity and rate of drying shrinkage can be mitigated by reducing the initial water content or cementitious materials content. Crack propagation can be controlled through the provision of expansion and construction joints. In structural concrete, the distribution of steel reinforcement can be used to distribute cracks (Tatro et al., 2007).

2.12 Thermal Gradient in Concrete

A thermal gradient is defined as the temperature profile along a specific path through a concrete element or structure (Tatro et al., 2007). The initial temperature condition is determined by the heat evolved during the cement hydration process. The dissipation of this heat occurs over several days in small concrete elements and over several years in large structures such as dams. The exposed surfaces, which are influenced by daily and seasonal cycles of temperature, undergo cooling at significantly faster rates than the core. This non-uniform cooling results in thermal gradients. Concrete has a positive coefficient of thermal expansion thus it increases in volume when the temperature increases. Thermal gradients result in uneven expansion and contraction resulting in internal restraint. When the core is warmer than the surface, there is tension on the surface and compression at the core as shown in Figure 2-18.
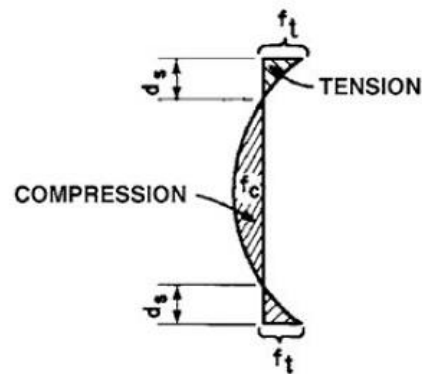
Figure 2-18: Stress profile due to temperature induce internal restraint (Tatro et al., 2007)

The stress state is valid when the temperature at a given point along the thermal gradient deviates from the stress-free temperature. Several researchers determined methods for the prediction of the stress state due to thermal gradients. (Equation 2-24 and (Equation 2-25 can be used to determine temperature gradient at which concrete will crack and the thermal stress at any point in a concrete slab with internal restraint only (Tatro et al., 2007, Zhu 2018).

$$\sigma = -E_c \, \alpha \, \Delta T \qquad \text{(Equation 2-24)}$$

where:

σ = Stress (MPa)

E_c = Modulus of elasticity (GPa)

α = Coefficient of thermal expansion (10^{-6}/°C)

ΔT = Difference in temperature between outermost fibre and centroid (°C)

$$\sigma = \frac{E_c \, \alpha}{1 - \mu} \cdot \left[T_m + \frac{T_d}{d} - T \right] \qquad \text{(Equation 2-25)}$$

where:

σ = Stress (MPa)

E_c = Thermal conductivity (J/m·°C)

α = Coefficient of thermal expansion (10^{-6}/°C)

μ = Poisson ratio

T_m = Effective temperature (°C)

T_d = Specific heat (J/kg·°C)

T = Temperature (°C)

2.13 Numerical simulation of Concrete

This section provides a summary of heat transfer modelling. The text proceeds "in a logical order of complexity" (Lewis et. al, 1996). The advent of the modern computer has increased the use of numerical simulations, leading to their acceptance as a reliable analysis and design tool. There are various applications for heat transfer modelling in the civil engineering industry, ranging from prediction of thermal stress where road structures are susceptible to frost heave to the design of insulation materials in building structures.

The numerical methods, combined with high speed computing, can be used as an economically viable optimization tool. The type of analysis can be tailored to solve specific problems, as summarised by Lewis et al. (1996):

> *"For the simulation of problems involving porous capillary materials, such as timber and ceramics, a coupled heat and mass transfer analysis is required. The optimal drying rate to ensure a reasonably stress-free end product will be tied in with the energy cost of the kiln schedule. Mathematical models, which can accurately predict the movement of moisture and heat in porous materials, are often the only means of gaining a better insight into the physical process. Similar models prove useful in designing geothermal energy extraction systems or in the analysis of advanced oil recovery by thermal methods."*

2.14 Summary

A review of the literature relevant to the subject matter of this research project was presented in this chapter. The following conclusions were drawn from the published works:

- Concrete structures are subjected to highly variable and varied climatic loads including solar radiation, ambient air temperatures, wind and various forms of precipitation. The economical design of future infrastructure will require that the aforementioned factors be considered together with the permanent and variable actions as they will contribute to the behaviour of the infrastructure throughout its lifecycle.

- The abovementioned climatic factors vary with geographic locations and time. Daily variations are observed as warm days and cool nights while annual variations are observed as changes in season. In summer, structures are exposed to high global radiation intensities resulting in large temperature differentials. In winter temperature differentials decrease, however, large negative temperature gradients are not uncommon.

- Climate change is an unequivocal global challenge that will have catastrophic effects on the economies of developing countries by 2030 if adequate mitigation measures are not implemented with immediacy.

- Urban areas consist of large volumes of concrete and bituminous materials. These materials have high thermal inertia and have resulted in the increase of ambient temperatures that contribute to the climate change problem through increased carbon dioxide emissions and production of smog.

- Portland cement concrete is an evolving material that is the most widely used construction material in the world by volume. The production of Portland cement contributes 5% of anthropogenic carbon dioxide emissions. Its thermal properties are highly variable and largely dependent on the types of aggregates which make up to 85% (by volume) of concrete. These characteristics influence rates of heat transfer, thermal gradients and the storage of thermal energy which is an important factor in urban areas.

- The surface characteristics of concrete, namely solar absorptivity and emissivity, influence the energy balance within and surrounding the structure or element.

- Climatic factors influence all concrete structures, however, the adverse effects are most pronounced on structures with large horizontal components such as bridges, buildings and pavements.

- Concrete structures constantly undergo volume changes due to variations in moisture content and temperature. When these volume changes are restrained, compressive and tensile strains and associated stresses are induced and may result in cracking if the tensile capacity of concrete

is exceeded. Restraint may be internal or external where the former is induced by moisture or thermal gradients.

- Numerical simulation provides an economical solution for the shortcomings of experimental modelling. Simulations can be used to predict and optimise the behaviour of engineering systems.

Many of the previous studies related to the subject matter of this dissertation were performed in Europe in the late 20th century. A validation of the assumptions and outcomes of this research is required in a world with rapidly changing climate and construction technology. The development of guidelines for the design of concrete structures in the Southern African climate would be valuable. Consequently, research performed in this field can contribute towards a fundamental understanding of what such guidelines would require.

Chapter 3   Experimental Investigation

3.1   Introduction

Concrete structures and elements are subjected to complex and highly variable climatic loads that contribute to the stress states experienced by the structures and increase the rates of deterioration, thereby reducing the lifespan of such infrastructure. The economical design of future concrete structures requires an understanding of climatic factors as well as the consideration of such factors along with the permanent and variable load actions used in the conventional design of concrete structures. Climate change and climate variability were discussed in the literature study (Chapter 2), where it was found that anthropogenic heat and convective heat transfer from the warm surfaces of engineering structures have and continue to contribute to the long-term increase of the global average temperature and short-term increase of urban air temperatures. The latter effect was termed the *urban heat island effect* and it was posited that this effect could be reduced through the use of reflective surfacing on concrete structures and pavements. The urgency of the climate change problem, confirmed by the commitment of 197 countries to limit the increase of the global average temperature to *"well below 2 °C above pre-industrial levels"*, motivated the need for an experimental investigation of the effects of surface characteristics on the thermal response of concrete structures. This chapter presents a discussion of the various stages of an experimental program in which the effects of surface characteristics, and daily and seasonal climatic variations on the thermal behaviour of three instrumented concrete beams were investigated.

The purpose of the experimental investigation was twofold:
- To obtain long-term, full depth temperature data for the concrete elements in the Pretoria climate; taking into account the extent to which surface colour affects thermal gradients and differential thermal expansion in concrete structures;
- To use the data collected to develop and validate a thermal prediction model (Chapter 4), and to perform a parametric study in which the effects of physical properties and climatic factors are investigated (Chapter 5 and Chapter 6).

The chapter begins with a discussion of the concrete specimens prepared and the mix composition thereof, followed by details of the instrumentation layout and characteristics of each instrument. Finally, the results of the various stages of monitoring are presented.

3.2   Concrete Beams

Three identical concrete beams were cast, dried and surfaced with white, black and grey paint. The elements were then embedded in a sand sink and exposed to climatic factors. This section provides details about the concrete specimens produced for the experimental study, the materials used, and the properties of these materials.

3.2.1 Mix Design and Materials

The concrete mix composition to be used in this investigation was selected in order to produce experimental specimens representative of structural elements produced for the construction of typical concrete structures. Additionally, the concrete required durability characteristics suitable for the intended exposure conditions which included direct exposure to climatic elements and wetting and drying cycles. Thus, a high durability ordinary-strength concrete mix composition with a 28-day target strength of 40 MPa was designed for this experimental investigation. High strength cement (CEM II 52.5N) was used with crushed dolomite aggregates sourced from a local supplier (see Figure 3-1). The concrete mix composition that was used is shown in Table 3-1.

a) Dolomite stone   b) Dolomite crusher sand
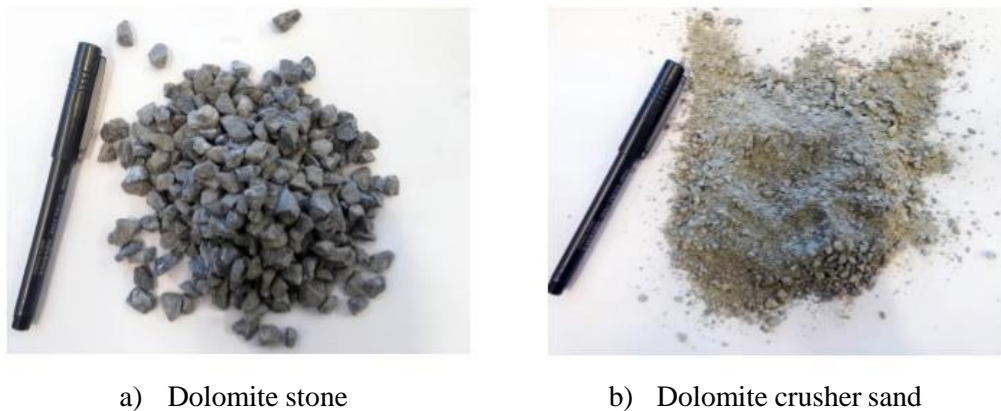
Figure 3-1: Crushed dolomite aggregate.

Table 3-1: Concrete mix design.

Component	Relative Density	Quantity (kg/m³)
CEM II 52.5N	3.02	382
Dolomite stone (9.5 mm)	2.84	880
Dolomite crusher sand	2.84	1004
Water	1.00	210
Theoretical concrete density	2.48	2476

3.2.2 Casting of Concrete Specimens

The shape and size of the concrete specimens to be used in the experimental study was representative of typical structural elements in full-scale structures. Concrete beams with cross-sections measuring 0.23 m x 0.15 m were selected as these dimensions were representative of typical columns, slabs, and traditional concrete pavements. A length of 1 m was selected as this was predicted to be sufficient to satisfy the assumptions made in the thermal analysis of concrete structures (see Section 2.9 of the literature study).

Standard steel moulds measuring 2 m x 0.23 m x 0.15 m were modified by placing steel plates at the midpoints of each mould. The moulds were further sealed using polyethylene coated industrial tape. After sealing, the moulds were lubricated with mould release oil to ensure that the specimens would be unaffected by the de-moulding process. The specimens produced included three 1 m long concrete beams, eight 300 mm long cylinders measuring 150 mm in diameter for stiffness (E-value) and tensile strength testing (Split cylinder), and eight 100 mm cubes for compressive strength testing. The concrete, with a total volume of 175 litres, was produced using rotary drum concrete mixers. The fresh concrete was then placed with continuous compaction using an industrial poker vibrator for the large specimens while the cubes and cylinders were compacted on a vibrating table. The purpose of compaction was to minimise the volume of entrapped air in the concrete as this would greatly influence the thermal and mechanical properties of the concrete. Figure 3-2 shows a single beam immediately after the concrete was placed.

Figure 3-2: Concrete beam immediate after placement of concrete.

3.2.3 Curing Regime

Immediately after the concrete was placed, polyethylene sheeting was placed over the samples and secured in place as shown in Figure 3-3(a). This was done to prevent excessive moisture loss from the samples as this would result in reduced compressive strength and excessive cracking on the beam surface. The sheeting was left in place for 48 hours, after which the specimens were removed from the moulds as shown in Figure 3-3(b). This method of curing was comparable to modern construction practices, whereby forms are removed within two to seven days after the concrete has been cast.

All of the concrete specimens remained under laboratory conditions (room temperature) for a further 5 days after which they were moved to a roofed external testing area where the specimens were exposed to variable hygrothermal conditions (moisture and temperature). During this period the density, modulus of elasticity, compressive and tensile strength were measured. The aforementioned results are presented in Section 3.7. The concrete beams were stored on the outdoor test area for a further six weeks to ensure that drying in each beam occurred before the subsequent stages of the experimental study commenced.

| (a) Curing during first 48 hours | (b) Air curing after first 48 hours |

Figure 3-3: Curing regime.

3.3 Instrumentation

In this section, the instrumentation and data acquisition methods used in the experimental study are described. The instrument types, characteristics and their locations are described. A steel wire mesh with 100 mm apertures and 3.55 mm diameter wires was formed into a rectangular frame on which the instrumentation was fixed in place. It was assumed that the quantity of steel used was negligible and would have no effect on the thermal response of the concrete beams.

3.3.1 Temperature Probes

Thermistor probes were manufactured using negative temperature coefficient (NTC) resistors with a base resistance of 5000 Ω at approximately 25 °C. The negative temperature coefficient indicated that the measured electrical resistance decreases as the temperature increases. These resistors have a working range of -40 °C to 67 °C with an accuracy of ± 1.0 °C within the -40 °C to 40 °C range.

A total of forty-eight thermistor sensors were placed on six separate sensor cables using a soldering process. Outer sensor cables had six sensors while central sensor cables had six or five sensors. Figure 3-4 shows the general layout of the thermistors as they were cast into each beam. Details regarding the spacing and locations of the temperature sensors as they were cast into each beam may be found in Appendix A of this dissertation. During the fabrication process, verification of each sensor was performed using the base resistance of 5000 Ω at 25 °C in a LAUDA-Brinkmann® RP 1840 water bath using a steady state verification time of twenty minutes. Moisture proofing was provided at the location of each individual probe as well as for the complete cable by using an industrial grade heat-shrink tubing. The verification procedure indicated that the insulation had no observable effect on the sensitivity of the thermistor sensors.
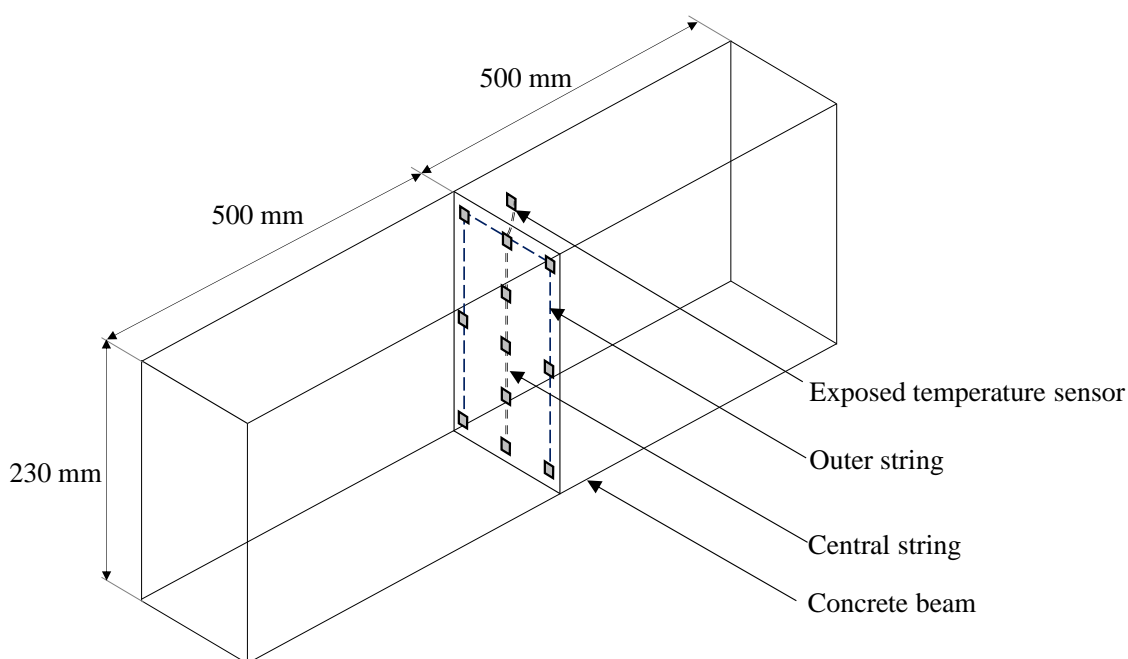
Figure 3-4: Beam elevation showing temperature sensor layout.

3.3.2 Embedded Concrete Strain Gauges

Vishay Precision Group, Inc. EPG-Series 350 concrete embedment strain gauges (See Figure 3-5) were placed in the centre of each specimen to measure mechanical strain. The strain gauges consist of a nickel-chromium alloy sensing grid with a gauge length of 100 mm, this allows strain adjacent to multiple aggregate particles to be measured and averaged. The sensing grid is cast into a polymer concrete casing with a grid to ensure full bonding to concrete to be measured (VPG, 2017). These gauges were selected for their self-temperature compensating characteristic which is favourable for the thermal monitoring of concrete structures. Figure 3-6 shows the schematic and final positions of each strain gauge.

Figure 3-5: EPG-Series concrete embedment strain gauge (VPG, 2017).
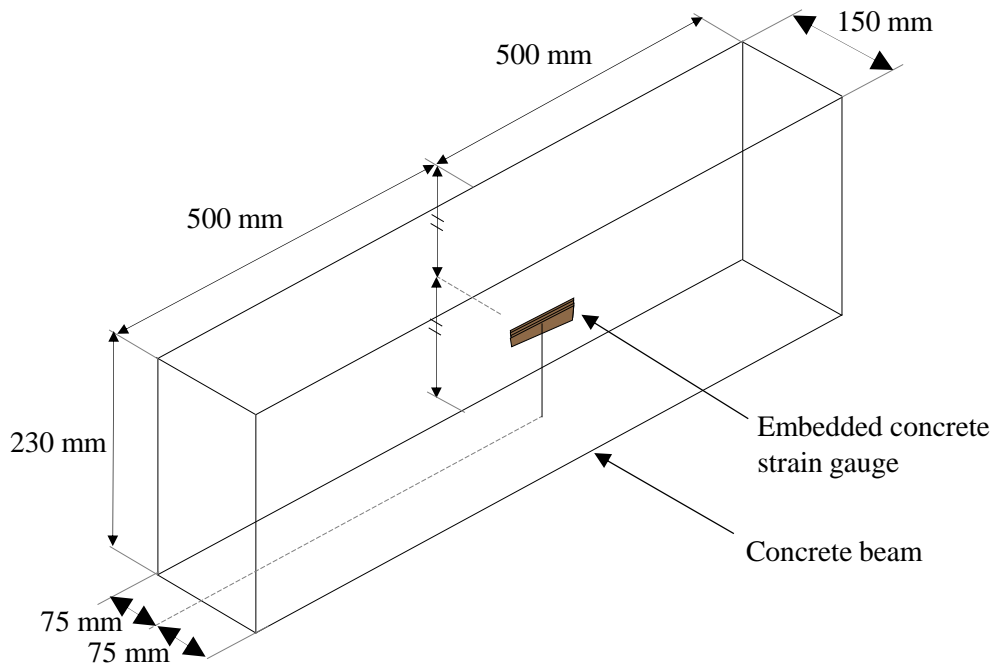
Figure 3-6: Beam elevation showing location of concrete strain gauge.

3.3.3 Concrete Surface Strain Gauges

TML FLA-6-11-3l linear foil strain gauges were placed on the surfaces of each specimen to measure axial strain. The gauges had a nominal resistance of 120 Ω, a gauge length of 6 mm, and a gauge factor of 2.12. The gauges were temperature compensated from 15 °C to 30 °C with a correction coefficient of 0.1 ± 0.5% per 10 °C. An excitation voltage of 5 Volts was used. A Wheatstone bridge configuration with a single strain gauge (Quarter Bridge) was used for each strain gauge as shown in Figure 3-7 (Hoffman, 1974). Temperature effects were compensated for in accordance to Equation 3-1.
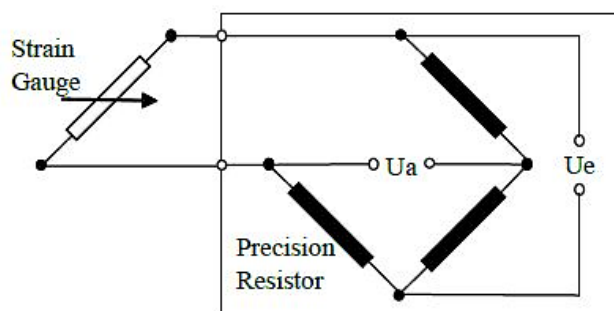
Figure 3-7: Wheatstone quarter bridge (Hoffman, 1974).

$$\varepsilon_{corrected} = \varepsilon_{test} - \varepsilon_{app} \qquad \text{(Equation 3-1)}$$

where:

ε_c = Corrected strain (μm/m)

ε_{test} = Measured strain (μm/m)

ε_{app} = -26.8 + 2.42T - 6.16 x 10^{-2} x T^2 + 3.93 x 10^{-4} x T^3 - 8.68 x 10^{-7} x T^4 (μm/m)

T = Surface temperature (°C)

The unpainted beam surfaces were prepared and smoothed using industrial sanding paper. Quarter bridges were carefully fixed on opposite faces of the beam at the location shown in Figure 3-8 using a methylmetacrylate adhesive that cures within ten minutes at room temperature. Figure 3-9 shows the process used to prepare the surfaces, place the strain gauges, and an example of a fully bonded strain gauge after the adhesive had cured.
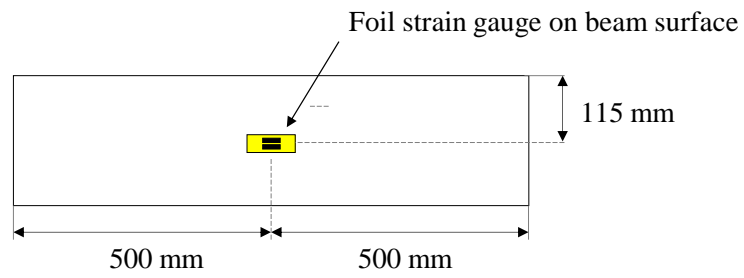
Figure 3-8: Plan view showing location of foil strain gauges on surfaces of the concrete elements.

a) Preparation of concrete surface
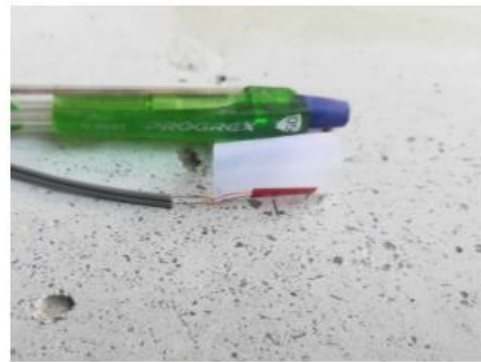
b) Placement of strain gauge
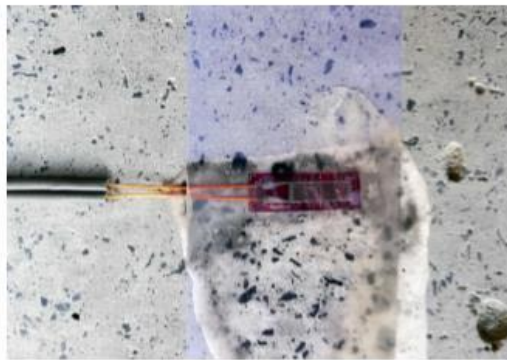
c) Fully bonded strain gauge

Figure 3-9: Preparation of surface and placement of foil strain gauges.

3.4 Data Acquisition System

Temperature and strain data were measured and recorded throughout the casting, curing, and the long-term monitoring of three concrete beams. These measurements were recorded through an acquisition system with a total of forty-two individually logged channels. A schematic layout of the data acquisition system is shown in Figure 3-10. The temperature data was recorded through a Campbell Scientific CR6 data logger, while the embedded and surface strain gauge data was recorded with Catman® data acquisition software using HBM QuantumX strain gauge amplifiers. The aforementioned logging systems were controlled using a personal computer that was located in the adjacent laboratory.

Personal Computer

Campbell Scientific CR6 data logger   HBM QuantumX Data Acquisition System

Temperature sensors   Embedded strain gauges   Foil strain gauges

Experimental set-up
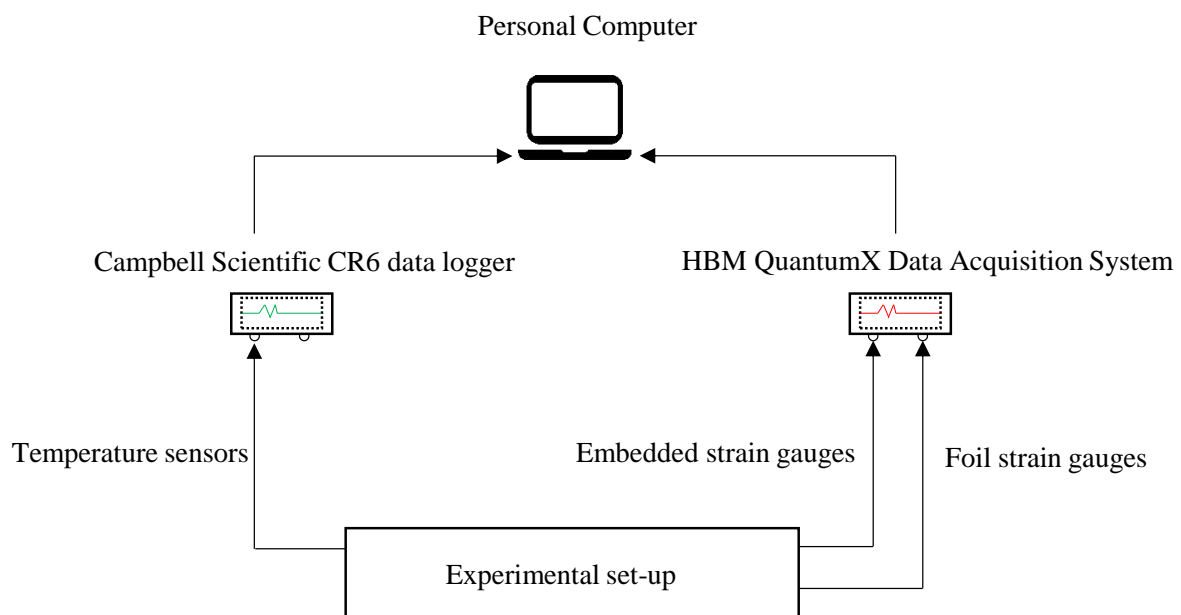
Figure 3-10: Schematic of data acquisition system.

3.4.1 Temperature Measurements

To capture temperature data, the set-up was equipped with a CR6 data logger manufactured by Campbell Scientific using the associated software. The recording capacity of the CR6 data logger was extended using two 16- channel relay multiplexers as shown in Figure 3-11. This allowed a total of 32 temperature sensors to be recorded simultaneously. An external power source was supplied to ensure uninterrupted data logging in the event of an electrical power interruption. This data was logged every second from the commencement of casting and for the first week after the specimens were cast. Following this, temperature data was logged every 15 minutes from December 2017 until July 2018.
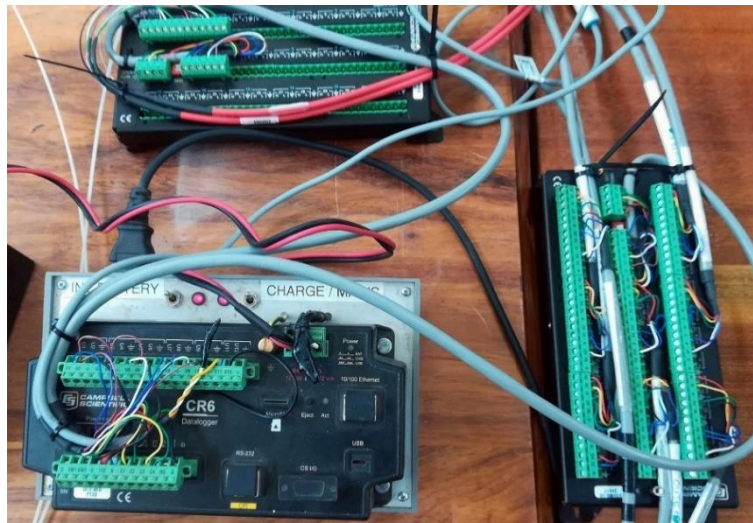
Figure 3-11: Campbell Scientific CR6 data logger and relay multiplexers.

3.4.2 Strain Measurements

Data from the embedded concrete and surface strain gauges were measured and logged throughout the duration of the study period. The experimental set-up was equipped with HBM QuantumX universal amplifiers as shown Figure 3-12. The strain gauge data was interpreted and logged using the Catman® data acquisition software every second during the first week after the casting of concrete. Subsequently, data was captured for 10 seconds, every 15 minutes from December 2017 to July 2018. It was not feasible to provide an external power source for this logging system, thus recurrent electrical power interruptions resulted in numerous discontinuities in the strain measurements.

Figure 3-12: HBM QuantumX universal amplifiers.

3.4.3 Weather Measurements

Climatic data was obtained from a weather station located on the roof of a building which has good solar exposure and largely unobstructed horizons on the University of Pretoria Hatfield campus. The weather station was installed in 2013 as part of The Southern African Universities Radiometric Network (SAURAN) Brooks et al. (2015). During the experimental study, climate data was recorded on the individual instruments that form the weather station at hourly intervals and transmitted wirelessly to a web-based platform that is accessible to the public.

The weather station, shown in Figure 3-13 (SAURAN, 2013), was equipped with multiple instruments including:

- Kipp and Zonen CMP11 tracker that measures global radiation;
- Campbell Scientific Cs215 sensor that measures air temperature and relative humidity;
- Texas TR525i sensor that measures rainfall, and
- R.M. Young 05103-5 sensor that measures wind speed.

Figure 3-13: University of Pretoria weather station (SAURAN, 2013).

3.5 Experimental procedure

3.5.1 Pretoria Climatic Conditions

During the eight-month long study period, air temperature, relative humidity, wind speed, daily rainfall, and global radiation were continuously recorded at a weather station as described in Section 3.4. The input parameters considered for the daily and seasonal analysis of thermal response, however, excluded the effects of relative humidity. Two seasons were considered, namely summer (1 December to 29 March), and winter (1 June to 31 July). Summer represented the period in which the study area had the highest air temperatures and solar radiation intensity while air temperature and solar radiation intensity were lowest in winter due to the decreased altitude of the sun during these months. The Pretoria region has a temperate climate with hot and wet summers, while sub-zero night temperatures are common in winter. The annual average temperature is 17.8 °C and the total annual precipitation averages 697 mm. The average daily temperatures, global radiation intensity, wind speed and rainfall are shown in Figure 3-14, Figure 3-15, Figure 3-16, and Figure 3-17. The maximum global radiation intensity, length of solar days, and maximum and minimum daily temperatures observed in each season are shown in Table 3-2.

It was observed that daily maximums of air temperature and solar radiation are not coincident. The highest air temperature of 34.6 °C was recorded on 8 January 2018, while the highest solar radiation intensity (1040 W/m^2) was recorded on 14 December 2017. Furthermore, the average daily time lag between peak solar radiation and peak air temperature was 3.5 hours in summer and 2 hours in winter. This is due to the earlier sunrise time in summer months and earlier sunset time in winter months.
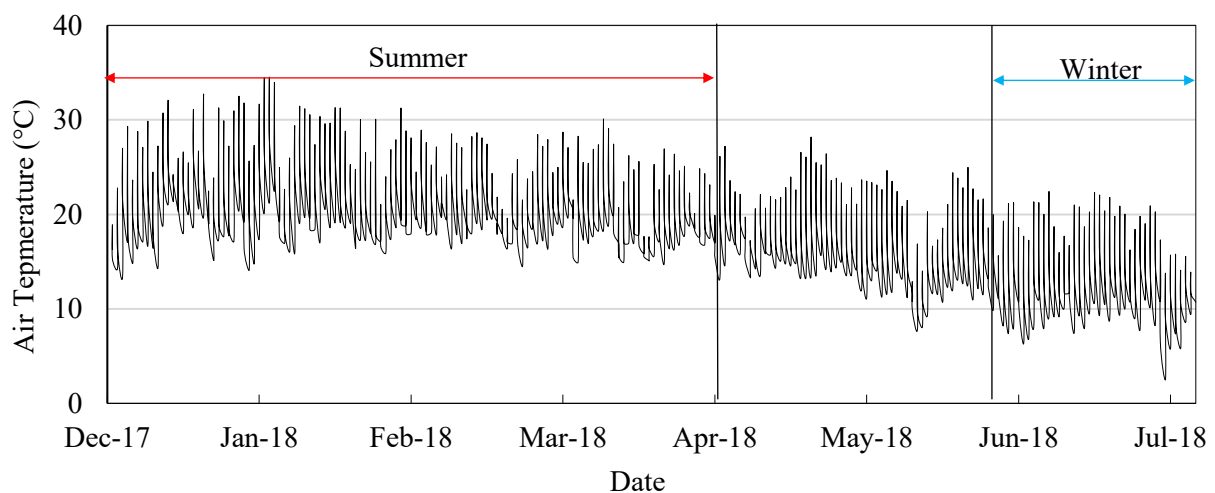
Figure 3-14: Average daily temperatures.
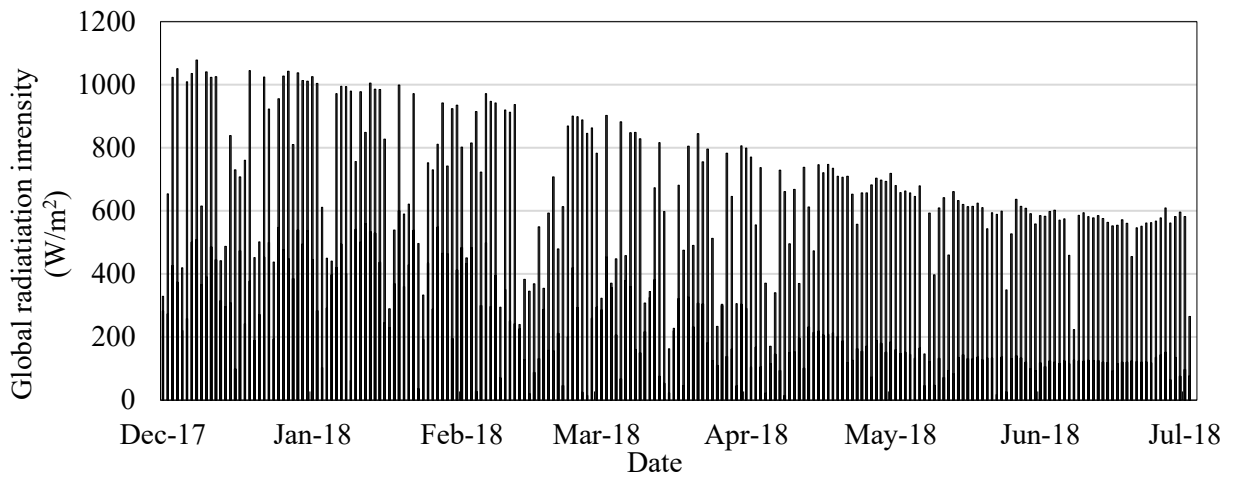
Figure 3-15: Maximum daily global radiation intensity.
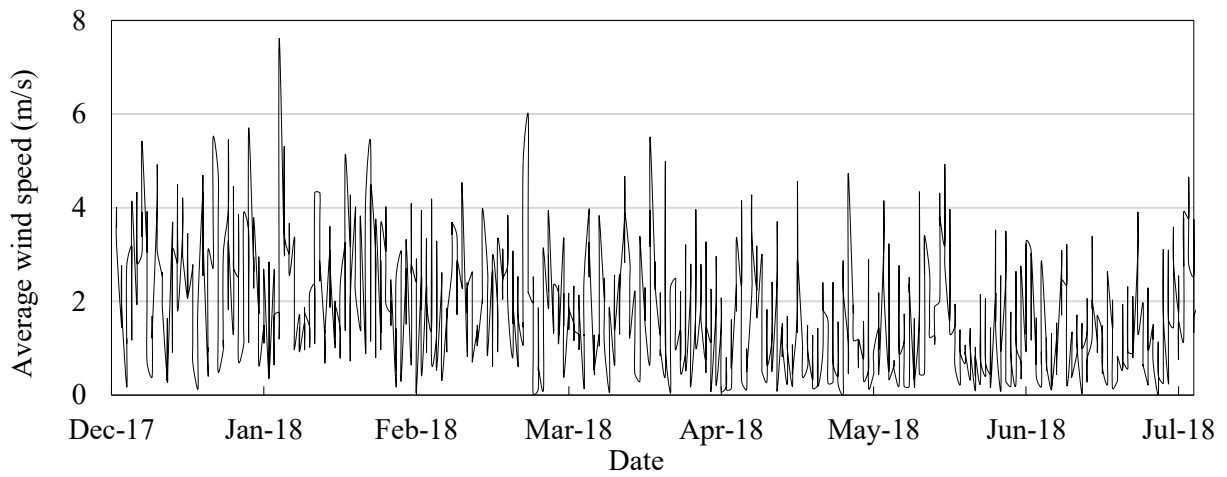
Figure 3-16: Average daily wind speed.
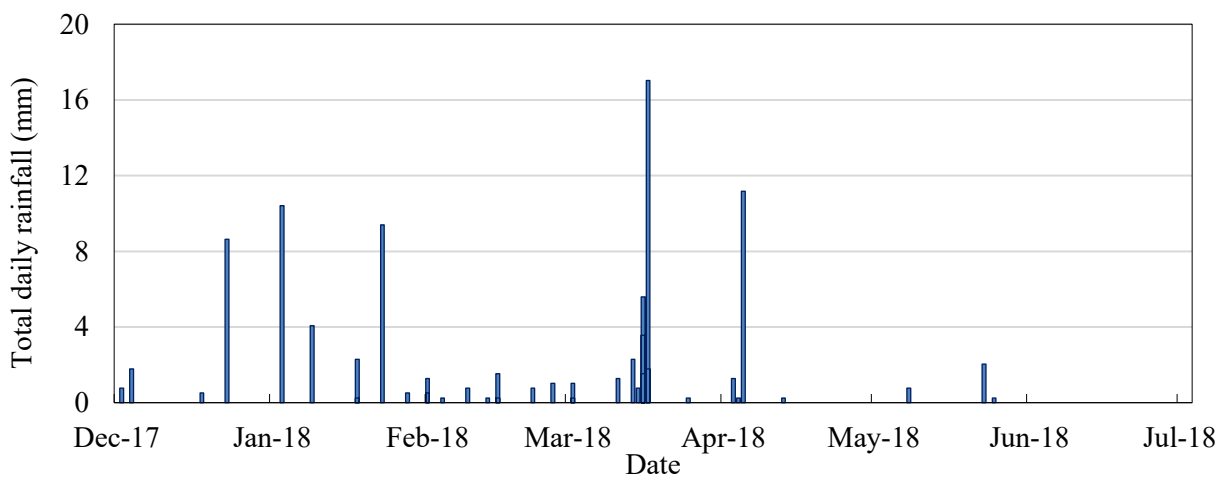
Figure 3-17: Total daily rainfall.

Table 3-2: Climatological conditions during experimental study.

Variable	Summer	Winter
Maximum Daily average solar intensity (W/m^2)	1020	660
Time at sunrise	05:00	06:00
Time at sunset	18:30	17:00
Maximum ambient air temperature (°C)	33.8	21.9
Minimum ambient air temperature (°C)	13.4	2.5

3.5.2 Curing and Drying of Concrete Beams

The concrete beams were stored in an outdoor testing area for approximately six weeks. During this time, the beams were exposed only to variations in air temperature and relative humidity as protection from direct sunlight, rainfall, and wind was provided by the roof and walls respectively. This phase in the experimental study allowed for drying shrinkage to occur thus allowing the beams to reach a constant and comparable hygrothermal state before the next phase of the experimental study commenced. Temperature and strain data were logged at 15-minute intervals during this six week period.

3.5.3 Selection of Experimental Site

The primary objective of the experimental study was to investigate the effect of climatic actions and surface characteristics on the thermal response of concrete beams. This required the selection of a location for the test set-up that would ensure that the beams were exposed to all weather components. Several criteria were taken into account, including the need for:

- An unobstructed horizon,
- Realistic exposure to solar radiation, and
- Free atmospheric moisture movement.

The laboratory roof of the Department of Civil Engineering at the University of Pretoria's Hatfield campus was selected as the experimental site as it satisfied the aforementioned criteria and was in close proximity to the weather station. The site was unimpeded with no obstructions that would cast shadows across the experimental area, unprotected from the elements. Figure 3-18 shows the skyline within the vicinity of the experimental site and Figure 3-19 shows the relative locations of the weather station and the test set-up.

Figure 3-18: Skyline around the University of Pretoria Hatfield campus (Google Maps, 2018).
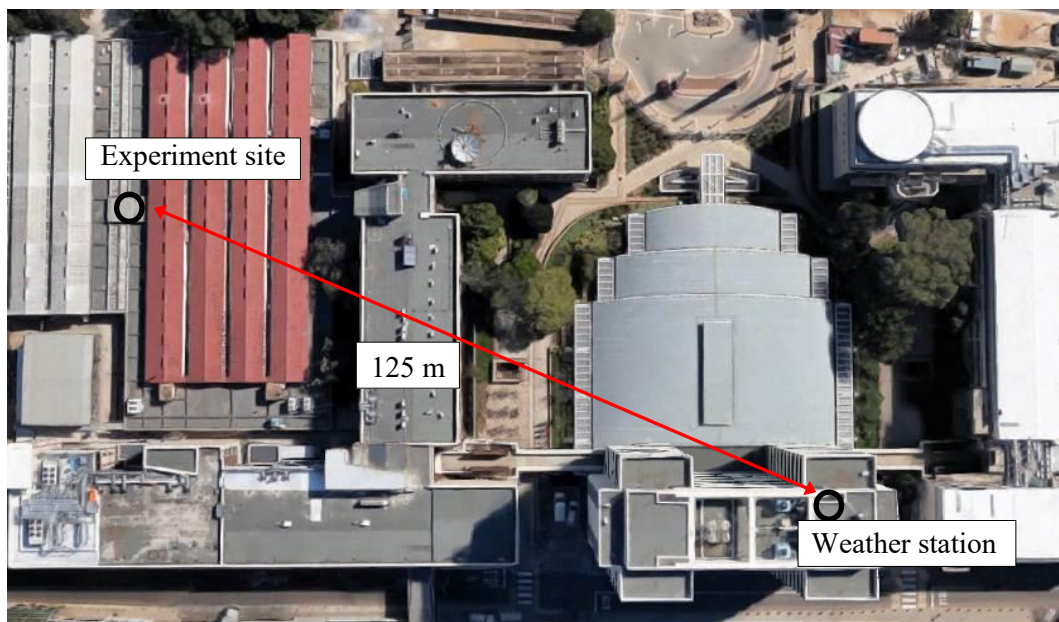
Figure 3-19: Location of test set-up and weather station (Google Maps, 2018).

3.5.4 Experimental Set-up

Three air-dried concrete beams measuring 1 m x 0.23 m x 0.15 m were placed 150 mm apart on a 50 mm layer of silica sand in a timber frame measuring 1.4 m x 1.2 m that was moderately elevated above the level of the roof with concrete plinths. The initial layer of sand was underlain with a geotextile to allow for the free drainage of water, which could flow away from the frame due to the provided plinths.

The three concrete beams were orientated such that the greater cross-sectional area was exposed to the surrounding environment. This orientation was selected to maximise the absorption and reflection of global radiation. On each concrete beam, a single strain gauge was exposed to the environment while the strain gauge on the opposite face was located at the concrete-sand interface. Silica sand was then placed around the beams to the level of the beam surface as shown in Figure 3-20. A schematic cross-section of the experimental set-up may be found in Appendix A of this dissertation. The sand was not compacted thus it was in a loose state. This was done to minimise the restraint to free lateral expansion as well as the frictional resistance at the base of each concrete beam. The exposed thermistor sensor on each beam measured the sand temperature 75 mm below surface level.

After the placement of sand, three layers of acrylic matt paint were applied to the beams resulting in surfaces that were white, grey, and black in colour. The beam surfaces were regularly cleaned and repainted to maintain the absorptivity and emissivity characteristics at thirty-day intervals, as well as after any rainfall events. Figure 3-21 and Figure 3-22 show the placement process and the surface condition before and after a rainfall event.
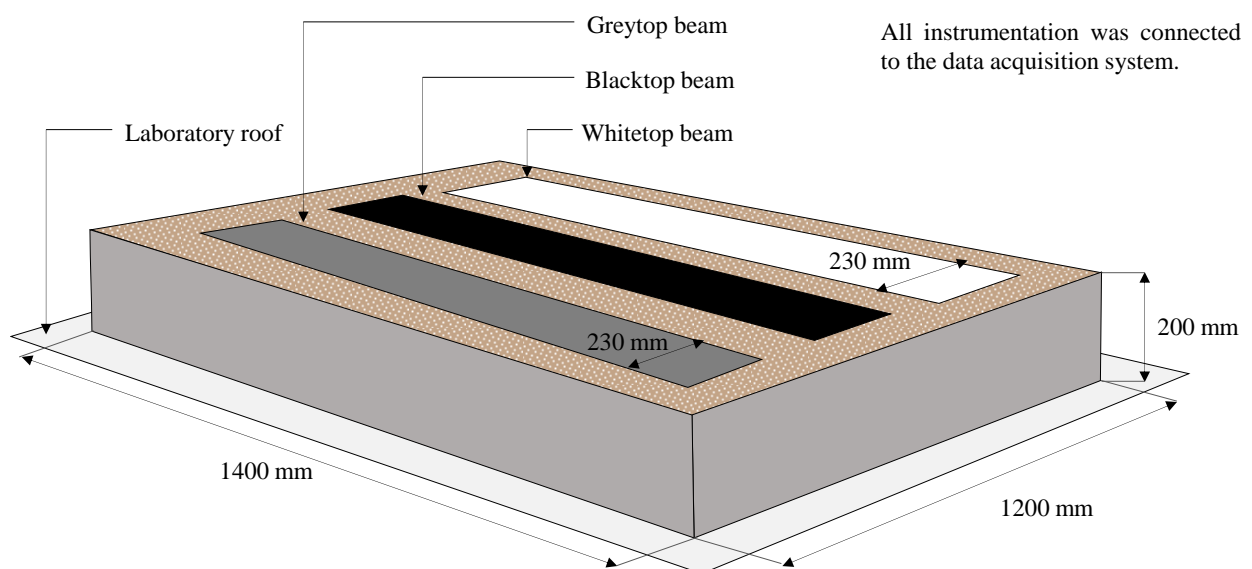
Figure 3-20: Schematic of experimental set-up.

a) Phase II of the experimental study.

b) Concrete beams on laboratory roof.

c) Concrete beams before sand was added.

d) Concrete beams fully embedded in sand

Figure 3-21: Beams before and after embedment in silica sand thermal sink.

a) Concrete beams after application of paint
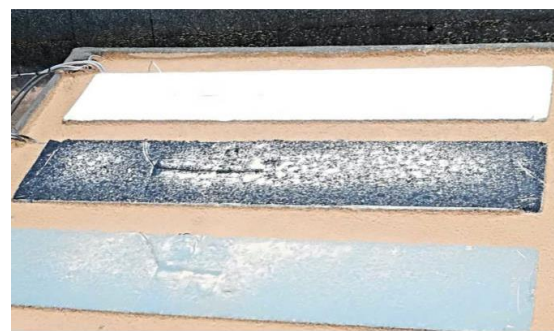
b) Concrete beams after rainfall

Figure 3-22: Surface condition of beams at different times during the experimental study.

3.6 Early-age Experimental Results

The thermal behaviour of fresh concrete was investigated during the casting process and for 24 hours after the concrete had been placed. During this initial phase, temperature and strain measurements were logged at one-second intervals. This resolution was used in order to accurately measure the effects of temperature change which is known to rapidly increase when the exothermic cement hydration reactions begin to occur. The mixing and casting of the elements were completed at midday with a placing temperature of approximately 24 °C. Thereafter, the concrete elements were sealed with polyethylene sheeting to prevent excessive moisture loss and stored in a large laboratory where the room temperature varies moderately. The physical dimensions of the main concrete elements were constant, thus volumetric effects on temperature were not investigated and it was observed that the thermal behaviour in all three concrete elements was comparable. Figure 3-23 shows the temperature at various points in the cross-section of one concrete beam, as well as at a point that was 25 mm above the concrete surface and covered by the polyethylene sheeting.
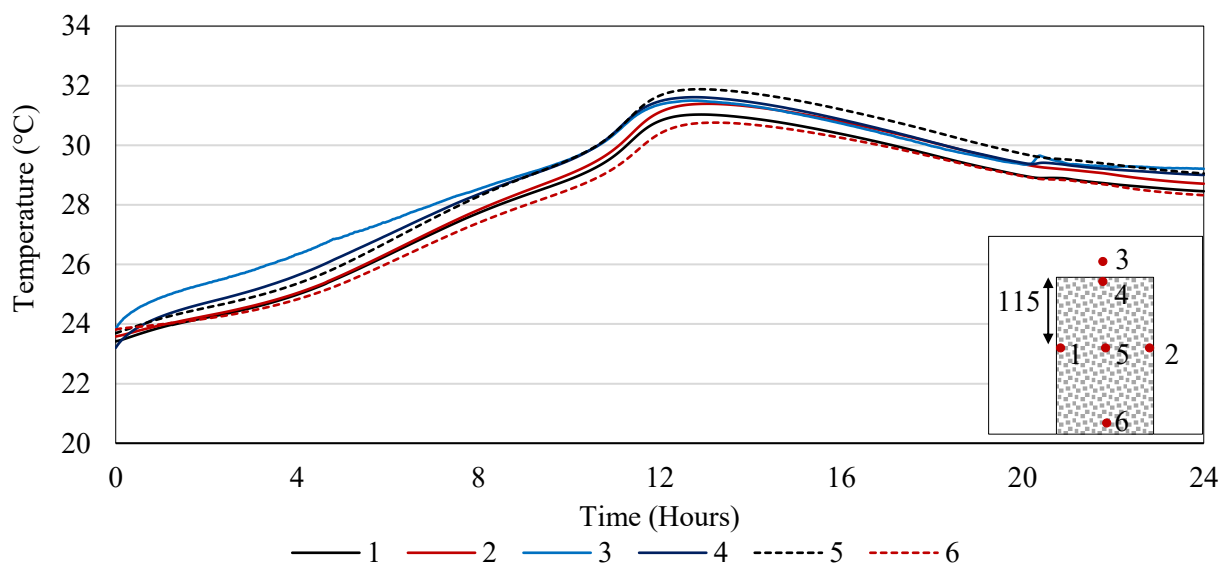
Figure 3-23: Variation in internal beam temperature due to cement hydration

These results show that the temperature in each element increased linearly from the placing temperature of 25 °C during the first ten hours, with the heat evolved causing an increase in the temperature above the sample. This temperature reduced gradually due to the rate of heat evolution reducing as well as the room temperature decreasing during the transition from day to night. This was followed by a rapid increase to a maximum of 31.6 °C after 12 hours. This trend was expected as the rate of heat evolution in fresh concrete increases rapidly approximately 10 hours after mixing when some products of the hydration reaction begin to crystallise (Domone and Illston, 2002). The temperature decreases with

increasing distance from the centre of the element due to heat transfer with the uninsulated steel mould and surrounding air. Due to the large surface area-to-volume ratio of the concrete beams, the heat of hydration escaped readily from the boundary surfaces thus the maximum temperature rise was not substantial.

The strains measured at the centre points in each concrete element are shown in Figure 3-24. The initial increase in strain was due to the increase in temperature experienced by the embedded strain gauge. These strains reach a maximum value after 12 hours when the concrete begins to increase in strength and stiffness. The subsequent plateau and slow decrease in strain was probably due to the concrete being restrained from free movement resulting in the development of compressive stresses.
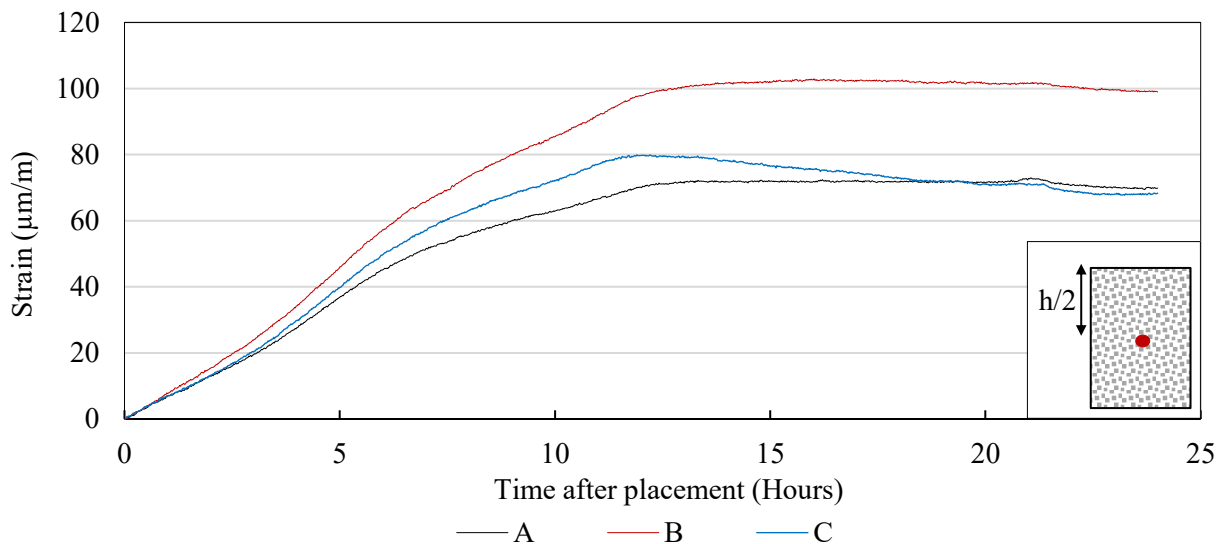
Figure 3-24: Core strain measurements during the first day after concrete placement

3.7 Mechanical Properties

The mechanical properties of the concrete were determined in accordance with standard test methods 1, 2, 4, and 7 days after the concrete elements were cast. At each interval, two 100 mm cubes were used to determine the compressive strength in accordance with the South African Standard SANS 5863:2006 (SABS, 2006) and two 200 mm diameter cylinders were used to test for the modulus of elasticity and indirect tensile strength (split cylinder strength) in accordance to ASTM C469-02 and SANS 6253:2006 respectively. The average results for each mechanical property as determined from the two specimens are shown in Table 3-3. The results indicate that the concrete beams had sufficient stiffness and tensile strength when they were demoulded after 2 days.

It is known that the 7-day strength of concrete is typically 60% to 70% of 28-day strengths for concrete produced with CEM I and CEM II (Tatro et al., 2007, Domone & Illston, 2002.The 28-day compressive and tensile strength were calculated assuming a conservative ratio of 70%, and are shown in the rightmost column of Table 3-3. The results show that the design strength of 40 MPa after 28 days was likely achieved. The bottommost row of Table 3-3 shows the predicted tensile capacity of the concrete at various ages. These values were calculated from the corresponding split-cylinder strength and modulus of elasticity.

Table 3-3: Measured mechanical properties of concrete.

Component	1 Day	2 Days	4 Days	7 Days	28 Days
Air cured density (kg/m^3)	2462	2466	2469	2483	-
Compressive strength (MPa)	13.0	21.0	31.8	37.2	(53.1)
Split cylinder strength (MPa)	1.33	2.21	2.74	3.03	(4.33)
Modulus of elasticity (GPa)	23.4	31.2	33.0	34.9	-
Cracking Strain (µm/m)	57	71	83	87	(124)

Transient thermal analysis requires the knowledge of material properties which include the specific heat (c), thermal conductivity (k), thermal diffusivity (h^2), and thermal expansion coefficient (α). As shown in the literature study, these properties could be predicted on the basis of concrete mix composition. In Table 3-4, the thermal properties of concrete made with dolomite aggregate published by a cement and aggregate producer operating the vicinity of the aggregate source are compared with values published by several researchers (Afrisam, 2016; Marshall, 1972; Tatro 2006). These published values compare well with the measured density of the air cured 100 mm cubes as shown in Table 3-4.

Table 3-4: Thermal properties of concrete produced with dolomite aggregate.

Author	Conductivity (J/m^2 °C m)	Thermal expansion coefficient (10^{-6}/°C)	Density (kg/m^3)
Tatro (2006)	2.60	9.50	2500
Marshall (1972)	2.71	10.60	2650
Afrisam (2016)	-	9.00	2570

3.8 Long Term Thermal Behaviour

This section presents the experimental results obtained from the commencement of the six-week drying phase in December 2017 until the end of the experimental study in July 2018. Three concrete beams were transferred from the laboratory building to an outdoor testing facility where they were stored for a further six weeks from December 2017 to January 2018. The purpose of this phase in the experiment was to ensure that the elements would reach a constant hygrothermal state that was comparable since the exposure conditions were the same. Figure 3-25 shows ambient air temperature and the effective temperatures measured in each beam during this period. The effective temperature governs the longitudinal movement of a concrete section and is a weighted mean of the temperature distribution in that section An example illustrating the calculation of effective temperatures from measured temperature data is shown in Appendix B. The results show the correlation of effective temperatures to changes in ambient air temperature throughout this period. This was likely due to the beams being protected from solar radiation, wind and rainfall by the roof and walls that were adjacent to the storage location.
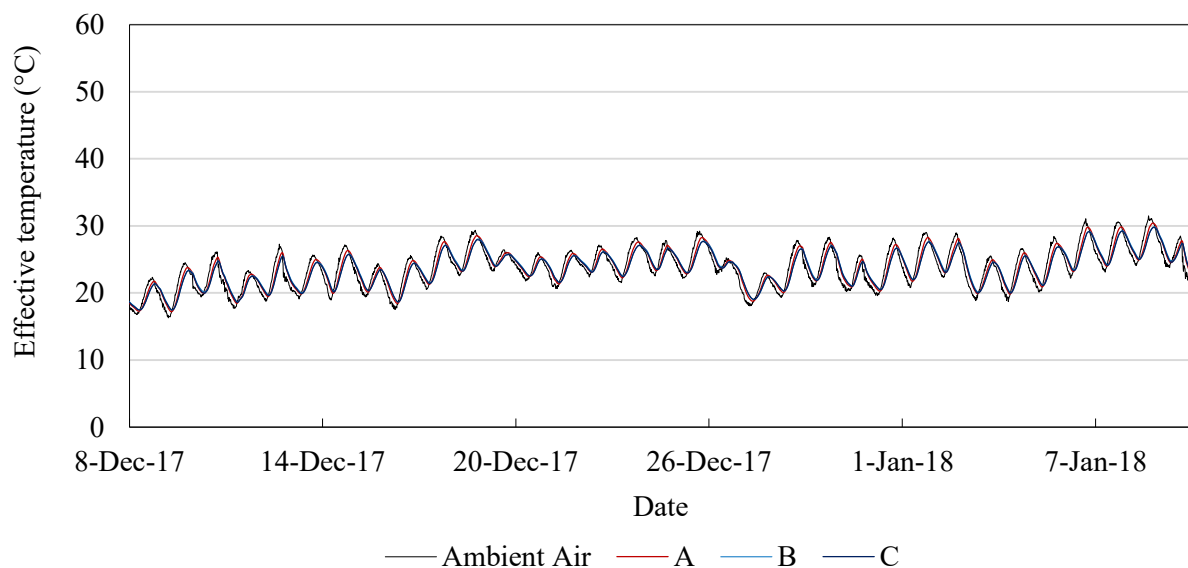
Figure 3-25: Effective temperatures during drying on outdoor test area.

In January 2018, the beams were relocated to the roof of the Civil Engineering laboratory on the University of Pretoria Hatfield campus where they remained until the commencement of the main experimental phase. Figure 3-26 shows the core and surface temperatures recorded in each beam for one week prior to and immediately after the start of the experiment. The concrete temperatures on the first four days shown in Figure 3-26 were measured before the beams were painted while they were in an upright position. The high temperatures recorded from 18 January to 22 January coincide with the

highest recorded ambient temperatures during the study. The concrete temperatures were further increased by the beams being exposed to solar radiation on multiple faces.
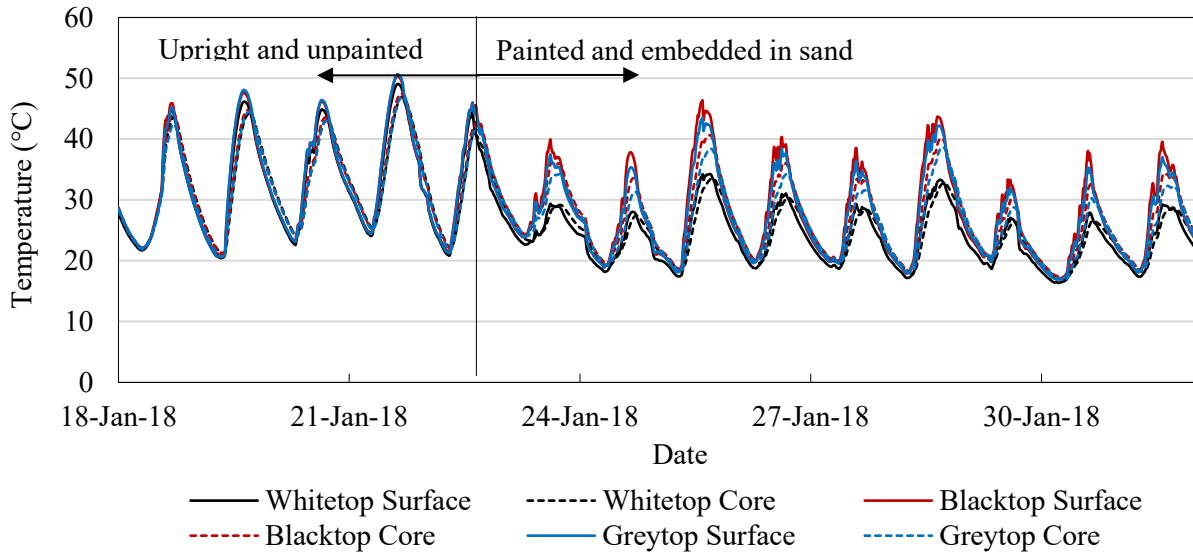
Figure 3-26: Core and surface temperatures before and after start of main experimental study.

The experimental set-up was completed with the white, grey and black surfacing applied on 23 January. The temperatures recorded on the following day show the effect of surface colour and the change in orientation which resulted in a reduction from 5 faces to only 1 which was exposed to climatic elements. The maximum temperatures following the start of the final experimental phase were recorded on 25 January, with a difference in maximum temperatures of 12 °C between the whitetop and blacktop beams. The surface and core temperatures recorded for the duration of the study are shown in Figure 3-27 and Figure 3-28 respectively. These results show the seasonal variation in the temperature of concrete beams from summer to winter conditions.
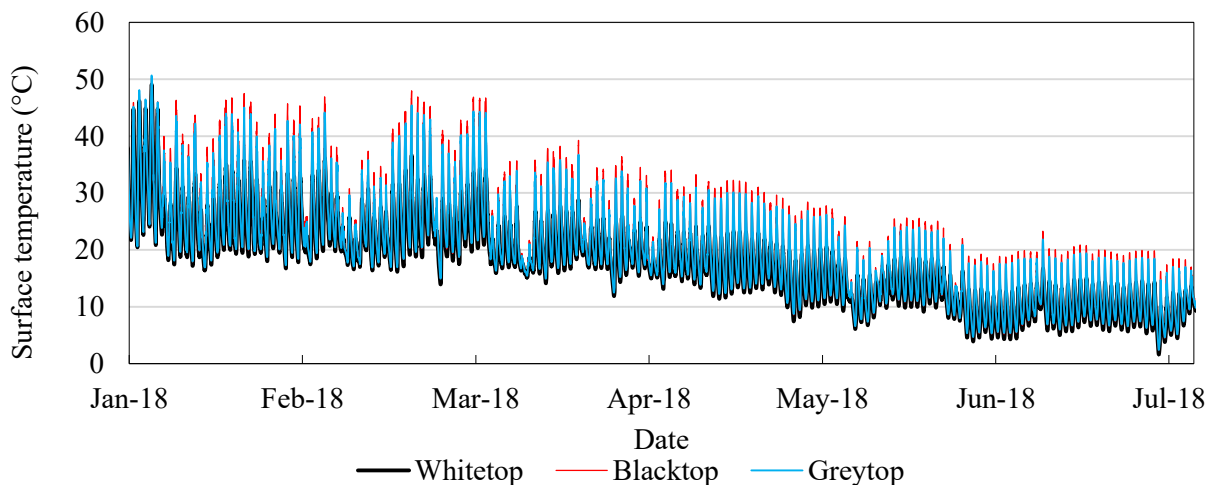
Figure 3-27: Surface temperatures measured during the study period.
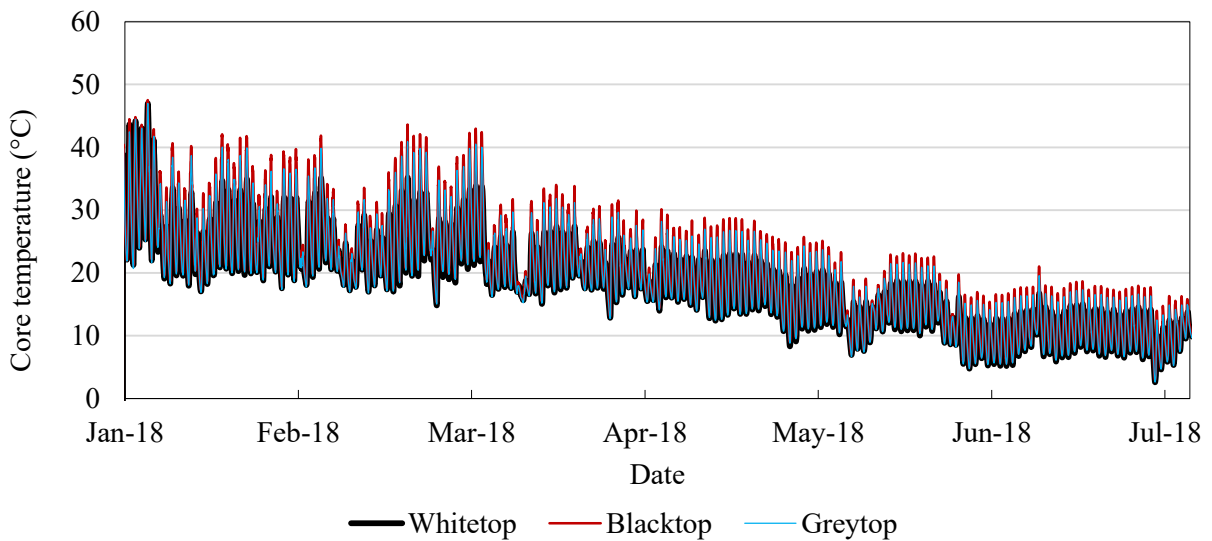
Figure 3-28: Core temperatures measured during the study period.

Figure 3-29 shows the correlation of the effective temperature in each concrete beam to the ambient air temperature. These relationships were determined using a statistical analysis of hourly temperature data recorded throughout the study. It can be seen that the gradient of each curve increases with increasing solar absorptivity, however, within a 3 °C range from approximately 11.5 °C to 13.5 °C the effective temperatures in all three concrete beams are similar. Figure 3-30 shows a comparison between the ambient air temperature and the average temperature measured 75 mm below the surface of the sand. The observed trends likely occurred due to the conductivity of silica sand being many times that of air. This relationship was used in the development of a two-dimensional heat transfer model in Chapter 4.
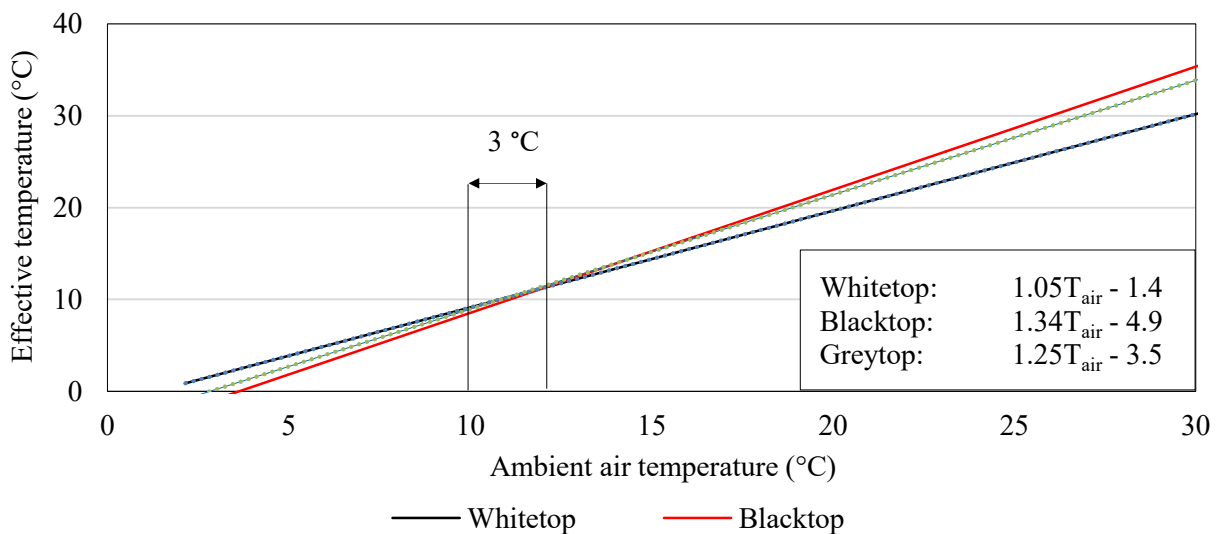
Figure 3-29: Correlation of effective temperature to ambient temperature.

3-24
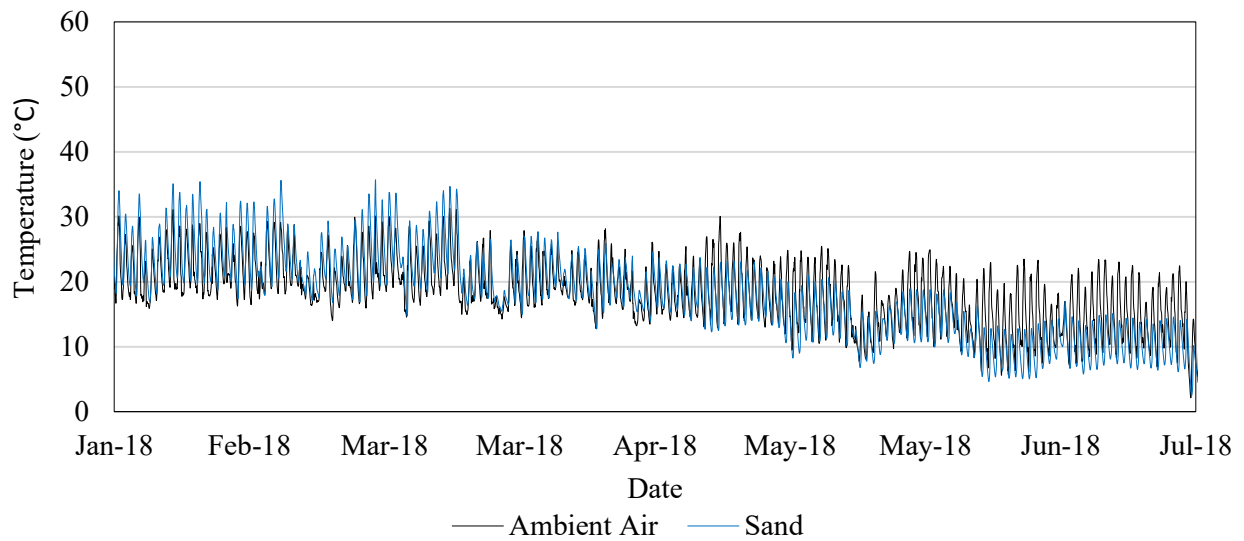
Figure 3-30: Comparison of ambient air temperature and average sand temperature.

The monthly maximum and minimum near-surface temperatures (top surface) measured during the experimental study are shown in Table 3-5. Additionally, the average monthly maximum near-surface and core temperatures measured during the study period are shown graphically in Appendix B.

Table 3-5: Average maximum, minimum, and diurnal range of near-surface temperature.

Month	Whitetop (°C)			Blacktop (°C)			Greytop (°C)		
	Max	Min	Range	Max	Min	Range	Max	Min	Range
January	34.8	16.6	18.2	46.3	17.0	29.3	44.4	16.7	27.7
February	36.1	16.4	19.7	47.5	17.0	30.5	45.0	16.9	28.1
March	36.6	13.9	22.7	48.0	14.9	33.1	45.4	14.9	30.5
April	25.9	11.4	14.5	36.4	12.3	24.1	33.9	12.2	21.7
May	21.3	6.1	15.2	29.6	6.6	23.0	27.6	6.6	21.0
June	16.7	3.9	12.8	23.3	4.7	18.6	21.8	4.7	17.1
July	14.3	1.6	12.7	19.8	2.4	17.4	18.4	2.4	16.0

3.9   Comparison with Previous Studies

The results obtained from the third phase of the experimental study can be compared with previous studies in which the thermal response of pavement structures was investigated. The basis for these comparisons is the similarity in the thermal loads to which the structural elements were subjected, the similarity between the sand thermal sink and in-situ subgrade material, and lastly the physical properties such as cross-section depth.

In order to form an understanding of climatic variation in the Pretoria region, a comparison was made between historical climate data and the climate records obtained during the experimental study. Figure 3-36 shows the maximum and minimum air temperatures recorded in 1978 by the South African Weather Bureau (SAWB, 1978) and 2018 for the months of January to July. The variation in temperature over 40 years indicates a reduction in air temperatures. While a longer record of complete climate data, which is a scarce resource, would be required to support this assertion, studies have shown that solar radiation intensity over Pretoria has decreased steadily by 1.7% (4.4W/m^2) per decade since the 1990s (Power and Mills, 2005). This reduction in solar radiation would be coupled with a reduction in air temperature, thereby, supporting this observation.
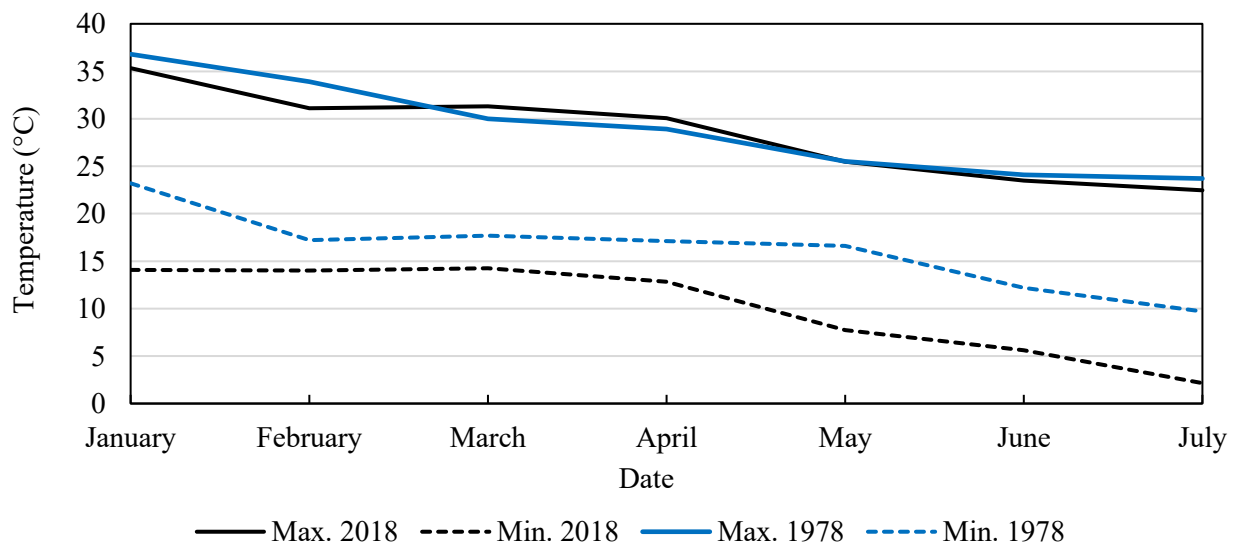
Figure 3-31: Pretoria Air temperatures in 1978 and 2018

Williamson and Marais (1975) conducted investigations into the temperature distributions in bituminous and concrete pavements in Southern African cities. Results obtained from the blacktop concrete beam compare well with experimental results obtained on bituminous pavements in Pretoria (1955), and in Cape Town (1961). These results of the maximum and minimum temperatures measured

25mm below the surface are shown in Figure 3-37 and Figure 3-38 for Pretoria and Cape Town respectively. The results show that surface colour has a larger effect on near-surface temperatures than the thermal characteristics of the material below the surface. It should be noted that the bituminous pavement surface areas were much larger than the blacktop concrete beam thus it was expected that the pavement temperatures would be higher.
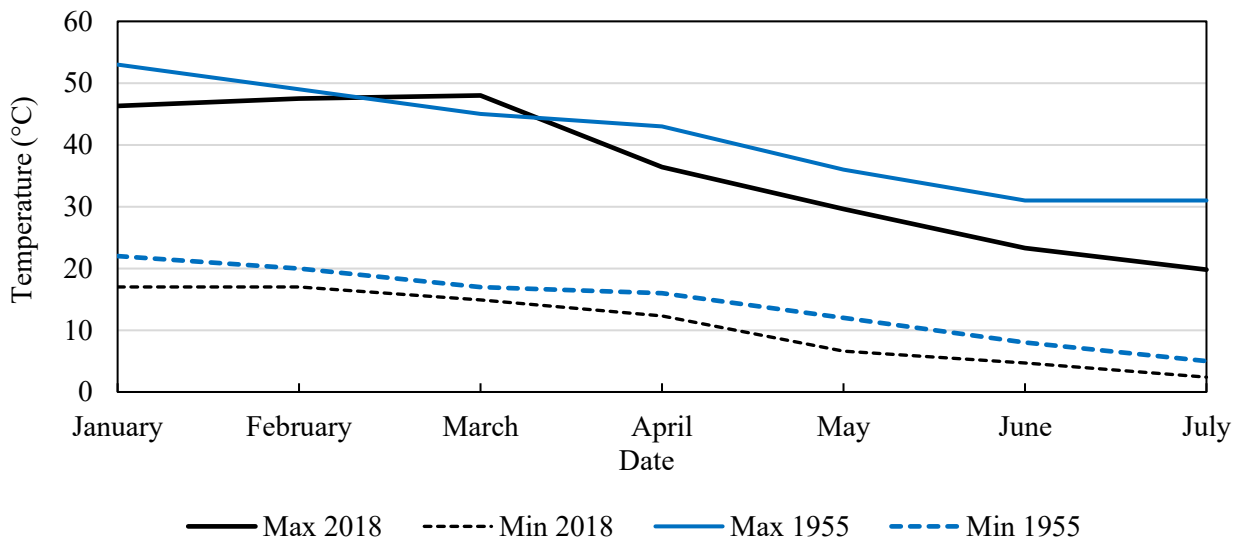
Figure 3-32: Comparison of blacktop near-surface temperature with Pretoria, 1955
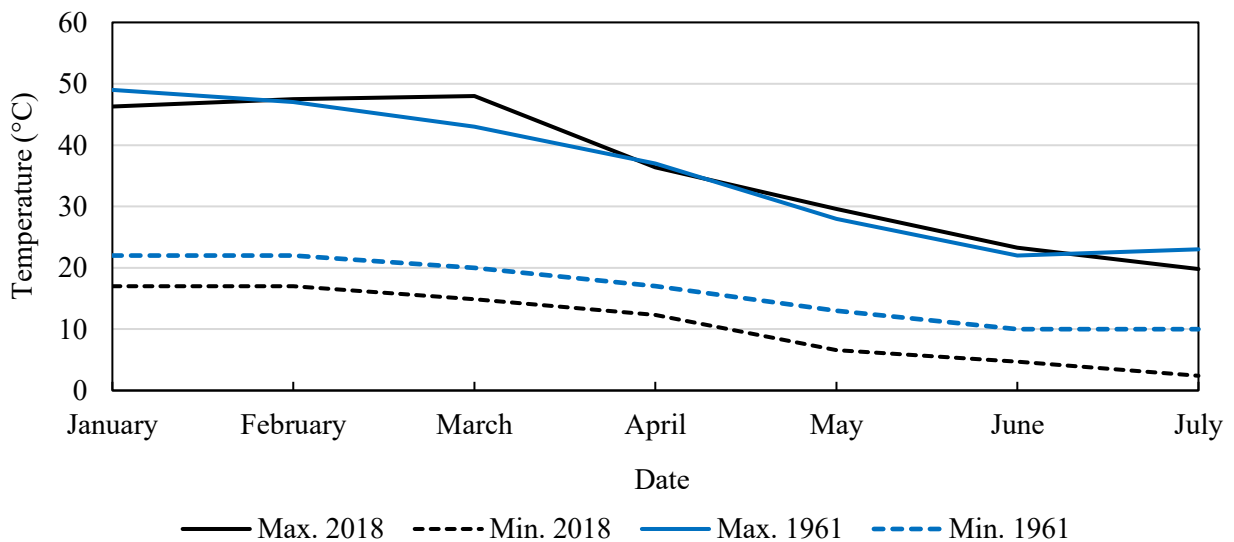
Figure 3-33: Comparison of blacktop near-surface temperature with Cape Town, 1961

Table 3-7 shows the maximum and minimum near-surface temperatures measured in the greytop concrete beam and the temperatures measured in a 150 mm deep concrete pavement in Pretoria in the studies by Williamson and Marais (1975). The results compared well, indicating that the greytop beam provided a good approximation of the thermal behaviour of a concrete pavement.

Table 3-6: Comparison of concrete pavement temperatures

Month	Concrete Pavement 1972 (°C)			Greytop Beam 2018(°C)		
	Maximum	Minimum	Full depth range	Maximum	Minimum	Full depth range
April	34	23	12	33.9	23	13
June	21	17	9	21.8	19.4	13

3.10 Shrinkage Strain

Figure 3-34 shows the load related or shrinkage strain in each concrete beam during the study period. The positive values indicated swelling and the negative strain values indicated shrinkage. It can be seen from the figure that there was positive volume change in all three concrete beams immediately after casting due to cement hydration. This was followed by a reduction in volume that continued to occur up to 200 days after the concrete was cast. Excessive shrinkage that is not adequately mitigated by creep can result in tensile cracking of the concrete.

Figure 3-35 shows an example of a shrinkage crack that was observed on the surface of the unpainted beams approximate seven days after the beams were cast. It is known that cracking occurs when the tensile capacity of concrete is exceeded by internal tensile strains. In the absence of external restraint, compressive and tensile strains and the associated stresses are induced by internal restraint. Thus, the crack shown in the Figure 3-35 was likely caused by either:

- A thermal gradient as the beam cooled following the completion of cement hydration reactions;
- A moisture gradient due to drying shrinkage, or
- A combination of the abovementioned forms of internal restraint.
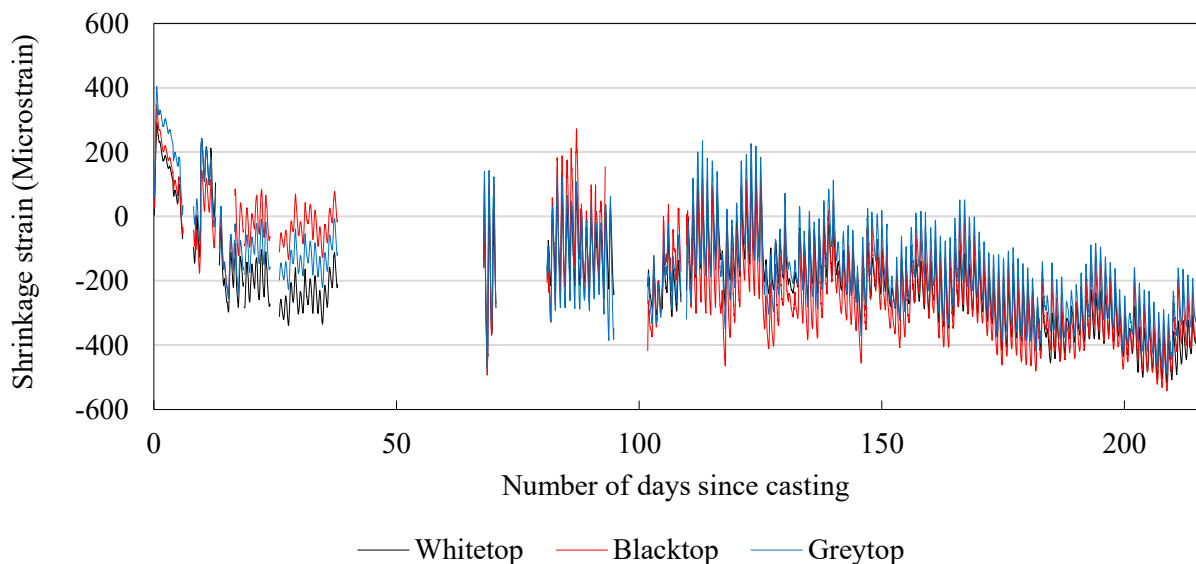
Figure 3-34: Shrinkage strain in concrete beams.
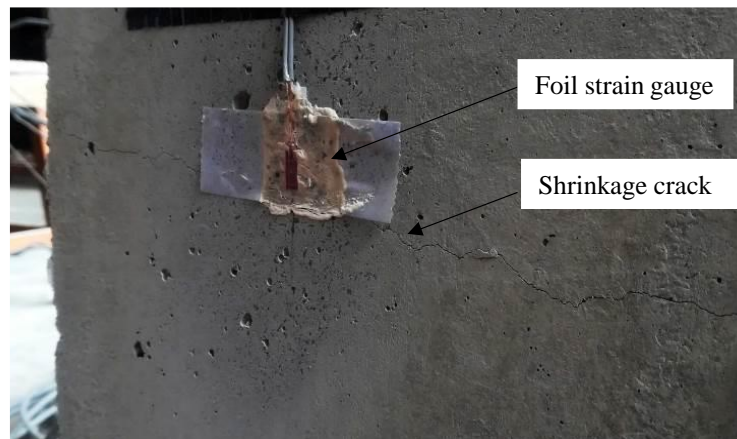
Figure 3-35: Shrinkage crack near centre of beam

The typical variation in the surface strain profiles during summer is shown in Figure 3-36. It was observed that strains varied diurnally with increasing day temperatures and cooling at night. At the strains indicated, cracking would likely have occurred in the concrete specimens, however, no visible cracks were observed. The sudden deviation of the strain profile on the lower surface of the concrete beam was likely due to a shrinkage crack forming in the vicinity of the strain gauge.
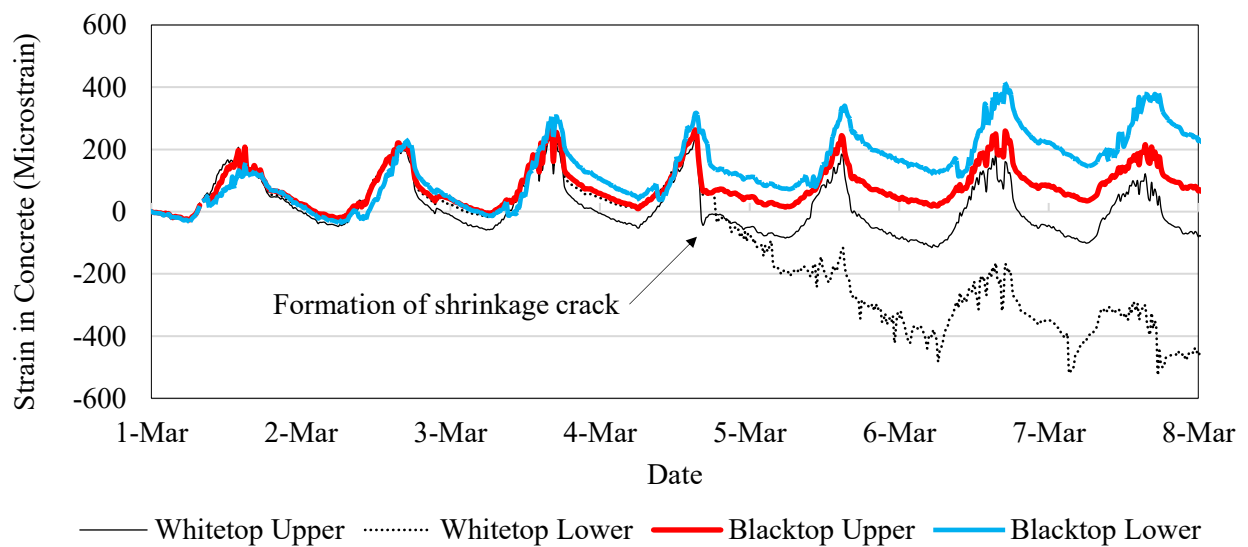
Figure 3-36: Thermal strains on concrete beam surfaces.

Due to shrinkage cracking occurring at the midpoints of each beam, it was found that reliable results could not be obtained from the surface strain gauges. Consequently, strain profiles would be calculated using the elasticity theory for the remainder of the study.

3.11 Thermal Gradients

Thermal gradients were defined as positive if the top exposed surface is warmer than the bottom surface and negative when the bottom is warmer than the top. The thermal gradients of the three beams on 25 January 2018 were compared as this was the warmest day recorded after the beams had been painted. These results showed uniform gradients through the depth of each beam between 04:00 and 08:00 when the lowest temperature in each beam is recorded (See Figure 3-37). The exposed surface increases in temperature rapidly and remains warmer than the bottom throughout the day until 20:00 when gradient reversal is observed. These trends are seen in both the whitetop and blacktop beam, however, a deviation from the trend is observed in the grey beam. The maximum gradients measured were 0.03 °C/mm, 0.068 °C/mm, and 0.075 °C/mm in the whitetop, greytop and blacktop beams respectively. Thermal gradients of 0.068 °C/mm and 0.075 °C/mm are comparable to the maximum temperature gradient of 0.077 °C/mm (Huang, 2004) that pavement engineers use for the design of rigid pavements.
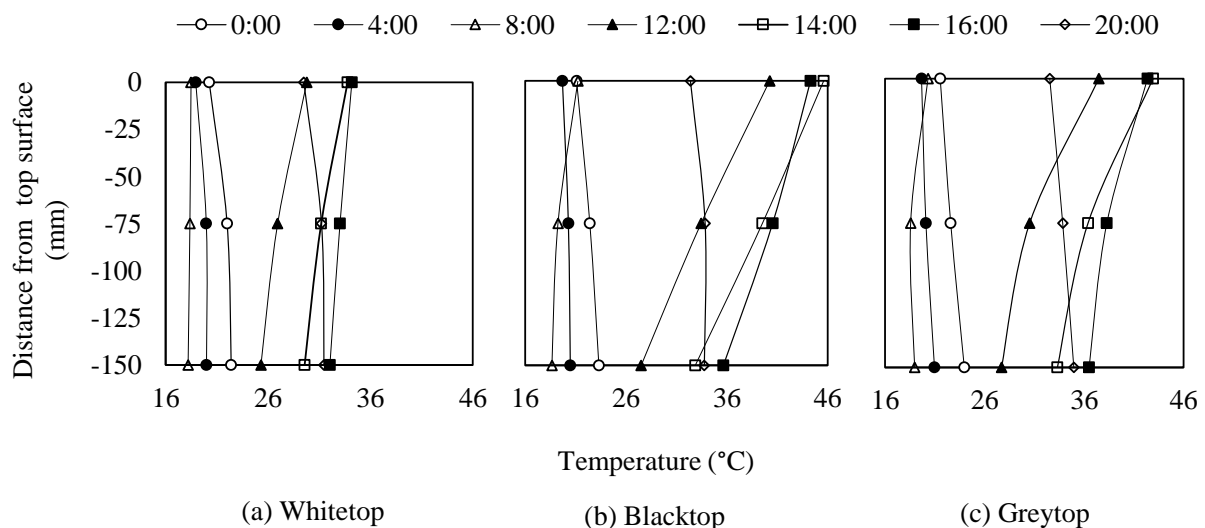
Figure 3-37: Thermal gradients on a typical summer day.

3.12 Summary

In this chapter, the details of an experimental program and results thereof were presented. Three mass concrete beams with a single concrete mix composition were instrumented and cast. The instrumentation used include thermistor sensors, embedded and surface strain gauges. The beams were stored for six weeks to allow drying to occur such that a constant moisture condition was achieved. An experimental set-up was designed such that the concrete beams would be located on the roof of a laboratory on the University of Pretoria Hatfield campus with unobstructed horizons and exposure to

climatic elements. Following this, the beams were embedded in uncompacted sand and surfaced with several layers of matt acrylic paint with varying solar absorptivity characteristics.

The beams were monitored from January 2018 to July 2018 for hourly measurements of temperature and strain. Comparisons to previous studies of pavement structures within the vicinity of the experimental area indicated that this experimental program was a good representation of full-scale pavement structures. These results were used to develop and validate a two-dimensional model that is described in the following chapters.

Chapter 4   Finite Element Model Development

4.1   Introduction

This chapter presents the development and validation of a two-dimensional heat transfer model for homogenous concrete sections The objective of the model was to simulate daily and seasonal temperature variation and thermal gradients in concrete sections by taking into account climatic factors, surface characteristics and conductive heat transfer within the material.

4.2   The Complete Abaqus Environment

The Abaqus package of finite element analysis modules was used to develop a two-dimensional heat transfer model that was validated using measured data from the experimental investigation that was described in Chapter 3. This section presents a discussion of the functionality and work flow used by the Abaqus package. The package consists of two complementary analysis modules, namely Abaqus/Standard and Abaqus/Explicit. The former is a general purpose module while the latter is tailored for dynamic analyses (Simulia, 2011). These analysis modules are incorporated into the Complete Abaqus Environment (CAE) which facilitates the modelling, management of analyses and the visualization of results. A summary of the work flow within the complete Abaqus environment is shown in Figure 4-1.
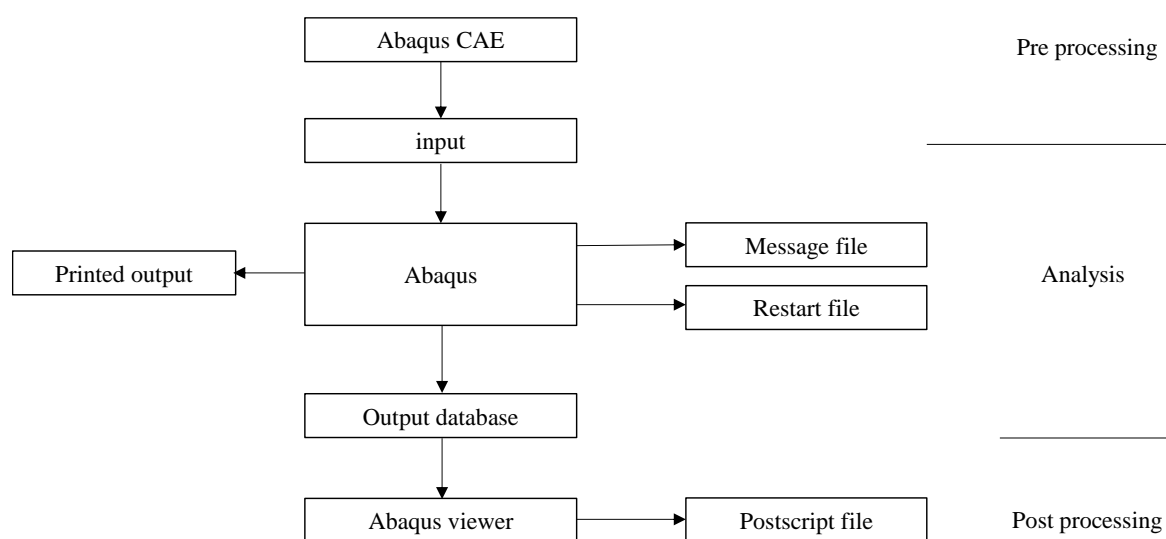
Figure 4-1: Analysis procedure in Abaqus.

4.3   Heat Transfer Algorithm for Finite Element Modelling

Information regarding the general solution to heat transfer problems was presented in the literature study. The Abaqus/Standard analysis module that was used to develop a two-dimensional heat transfer model makes use of a backwards difference algorithm programmed in the Complete Abaqus Environment (Simulia, 2011). For a complete discussion of the heat transfer algorithm used in Abaqus/Standard, the reader is advised to study the Abaqus v 6.11 theory manual (Simulia, 2011).

4.4   Energy Balance in Heat Transfer Modelling

The heat transfer modelling of climatic actions requires the use of complex thermal loads, heat fluxes, and interactions on surfaces between adjacent materials. The aim of the structural designer is to combine these loads, fluxes, and interactions so as to simulate the energy balance between a real structural element and its surrounding media. Concrete structures are subjected to various climatic actions, however, it is uneconomical to include every aspect of these climatic actions in the development of a numerical model. Figure 4-2 shows the loads and interactions that were used to develop the heat transfer model which included:

- Global or total solar radiation on the exposed upper surface;
- Longwave radiation emitted by the concrete element to the surrounding air;
- Convective heat transfer from the warm concrete surface to the cooler surrounding air;
- Conductive heat transfer within the concrete element, and
- Heat transfer between the concrete element and the surrounding sand.
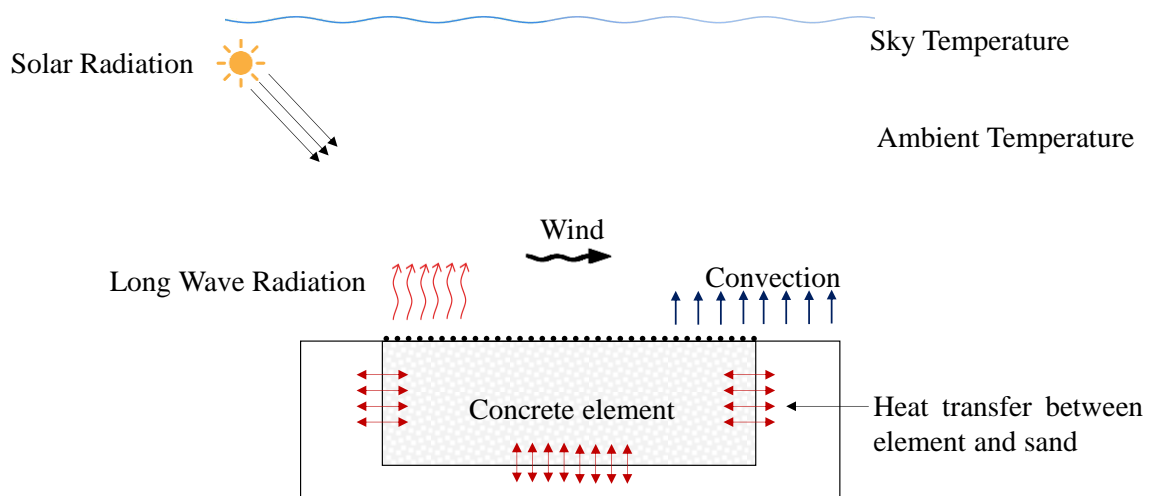
Figure 4-2: Thermal actions included in the prediction model

4.5   Abaqus Loads and Interactions

This section provides details of the loads and interactions used in the development of the thermal prediction model and their significance. Within the Abaqus CAE, interactions and loads are applied to the model geometry as shown in Figure 4-3a and Figure 4-3b respectively.

(a) Interactions on vertical edges   (b) Load on upper horizontal surface
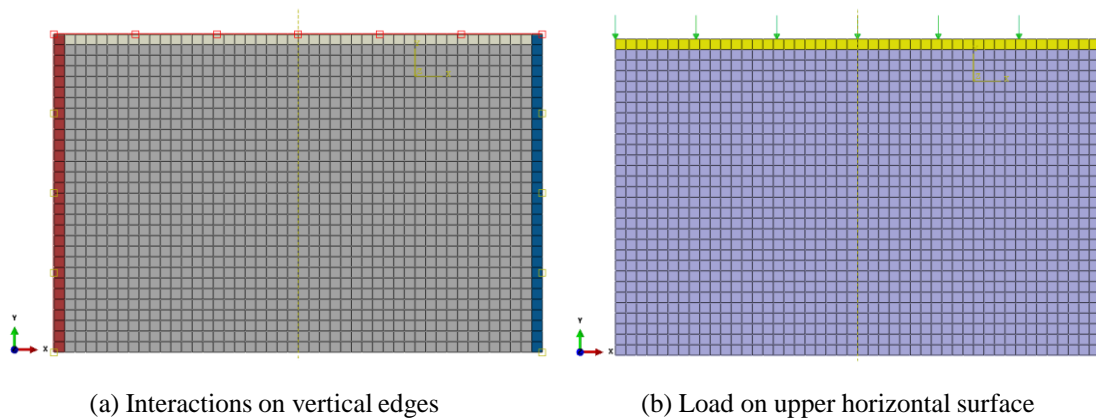
Figure 4-3: Loads and interactions in Abaqus.

4.5.1   Global Radiation

A surface heat flux was applied to the upper surface of the model geometry to simulate global horizontal irradiance. The surface flux is a load applied uniformly as shown in Figure 4-3b. Measured data for direct solar radiation from the weather station was applied as load magnitude at hourly intervals (3600 seconds). In instances where solar radiation data is unavailable, the models described in Chapter 2 of this dissertation may be used. An interaction coefficient representing the solar absorptivity was applied to surfaces exposed to radiation loads. The effect of surface texture on solar absorptivity was assumed to be negligible, thus these parameters were selected based on surface colour only.

4.5.2   Surface Convection

Convective heat transfer was modelled as a surface interaction on the upper horizontal surface shown in Figure 4-3a. An interaction coefficient equal to the convection coefficient was used, while the measured ambient air temperature was applied as the sink temperature, i.e. the temperature of the surrounding air. The convective coefficient was determined from measured wind speed data using Equation 2-12 (Larsson and Thelandersson, 2011). For wind speeds between 3 m/s and 8 m/s, this value ranges between 19 $W/m^2 \cdot °C$ and 23 $W/m^2 \cdot °C$.

4.5.3 Longwave Radiation

Long wave radiation is emitted from the specimen surface to the sky which was considered as a horizontal surface that completely absorbs the emitted energy. An interaction was therefore applied to the upper horizontal surface with a coefficient representing the radiation emissivity. The emissivity, dependent on surface colour ranged between 0.95 and 0.8, while the sky temperature was calculated from measured ambient temperature data using Equation 2-7 (Larsson and Thelandersson, 2011).

4.5.4 Concrete-Sand Interface

Interactions were applied to the vertical and lower horizontal faces shown in Figure 4-3a. An interaction coefficient that determines the rate of thermal flux was iteratively determined for the side and bottom surfaces of the concrete specimens. Sand temperatures, measured 15 mm from the faces at mid-depth (75 mm) were applied with linear interpolation between the ambient air temperature and the measured data for unknown temperatures across the depth of the sand heat sink.

4.6 Material Properties

This section presents details of the material inputs used to produce the heat transfer model. A homogenous two-dimensional solid material was assigned to a concrete section with dimensions representative of the beams that were instrumented and cast for the experimental investigation (Chapter 3). Table 4-1 shows the physical constants assigned in the Abaqus/Standard module, namely the Stefan-Boltzmann constant which governs radiative heat transfer from the solid material, as well as the reference or absolute zero temperature.

The thermal conductivity and specific heat characteristics that were assigned to the two-dimensional solid were selected from a range of published values presented in the literature study (Chapter 2), while the density of concrete was determined from laboratory testing using 100 mm cube specimens that were cured under the same conditions as the concrete beams. The measured density after seven days, compared well with published values for concrete produced with dolomite aggregates. For thermal conductivity and specific heat, the median values within the range of published thermal properties were assigned to the two-dimensional solid as shown in Table 4-2.

Table 4-1: Finite element model attributes.

Attribute	Value
Stephan-Boltzmann constant (W·m^{-2}· K^4)	5.67 x 10^{-8}
Absolute zero (°C)	-273.15

Table 4-2: Material properties of concrete used in finite element model.

Property	Range	Value Used
Conductivity (W/m·°C)	2.2 -2.7	2.5
Density (kg/m^3)	2400 -- 2600	2460
Specific Heat (J/kg·°C)	800 -- 1000	880

4.7   Surface Properties

The surface properties, emissivity and solar absorptivity, that were used in the development of the heat transfer model are shown in Table 4-3. These properties were determined from a range of published values presented in the literature study (Chapter 2). The median values from each range were selected and assigned to the heat transfer boundary on which incoming and outgoing radiation fluxes were applied to simulate the painted beam surfaces discussed in the experimental study (Chapter 3). It was found that an emissivity of 0.85 was applicable to all acrylic matt paints regardless of surface colour, while the absorptivity ranged from 0.22 for white paint to 0.95 for black paint. The painted surface texture was not considered in the determination of the aforementioned surface characteristics.

Table 4-3: Surface emissivity and absorptivity.

Surface Colour	Emissivity		Solar absorptivity	
	Range	Value used	Range	Value Used
Black Paint	0.70 - 0.90	0.85	0.88 - 0.95	0.95
Grey Paint	0.70 - 0.85	0.85	0.80 - 0.85	0.82
White Paint	0.70 - 0.85	0.85	0.15 - 0.30	0.22

4.8   Model discretization

The solid material used to develop the heat transfer model was discretised using quadratic C2D4R Abaqus/Standard heat transfer elements with 1:1 aspect ratio. These are 2-dimensional continuum (solid) elements with four nodes. Heat transfer occurs linearly by diffusion in both directions across each element (Simulia, 2011).

A mesh sensitivity analysis was performed to determine the optimal mesh dimensions. The final element size was selected once the solution converged, with mesh refinement, to within 0.1% of the solution. The mesh refinement varied from a coarse mesh with large elements and the element size was reduced to produce a fine mesh as shown in Figure 4-4a and Figure 4-4b respectively. Simulated results were compared to the instantaneous core temperature measured in the whitetop beam during a warm and rain –free week in March 2018 as shown in Figure 4-5. The difference between these simulated and measured temperatures is shown as a percentage of the measured temperature in Figure 4-6. From this investigation, a final element size of 2.5 mm x 2.5 mm was selected for model implementation. This element size corresponded to a total number of 5520 quadratic elements. Based on the results indicated in Figure 4-5 and Figure 4-6, increasing the number of elements beyond 5520 resulted in an increase in computing time with negligible change in the result error.

a)   Coarse finite element mesh   b)   Optimal finite element mesh
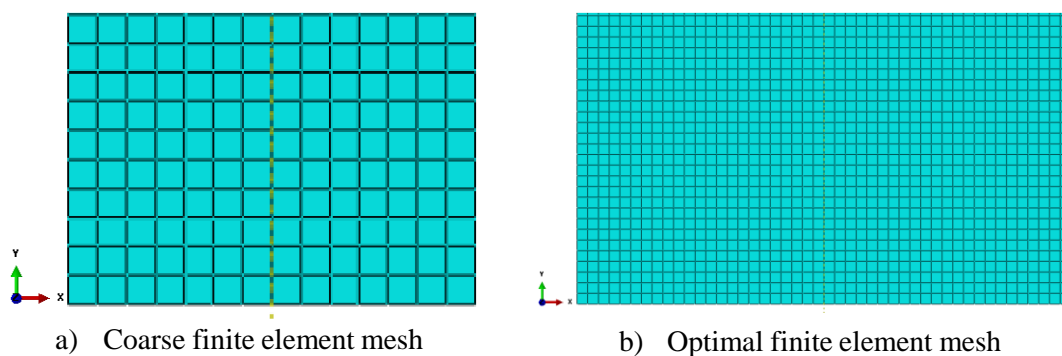
Figure 4-4: Finite element mesh used to develop model.
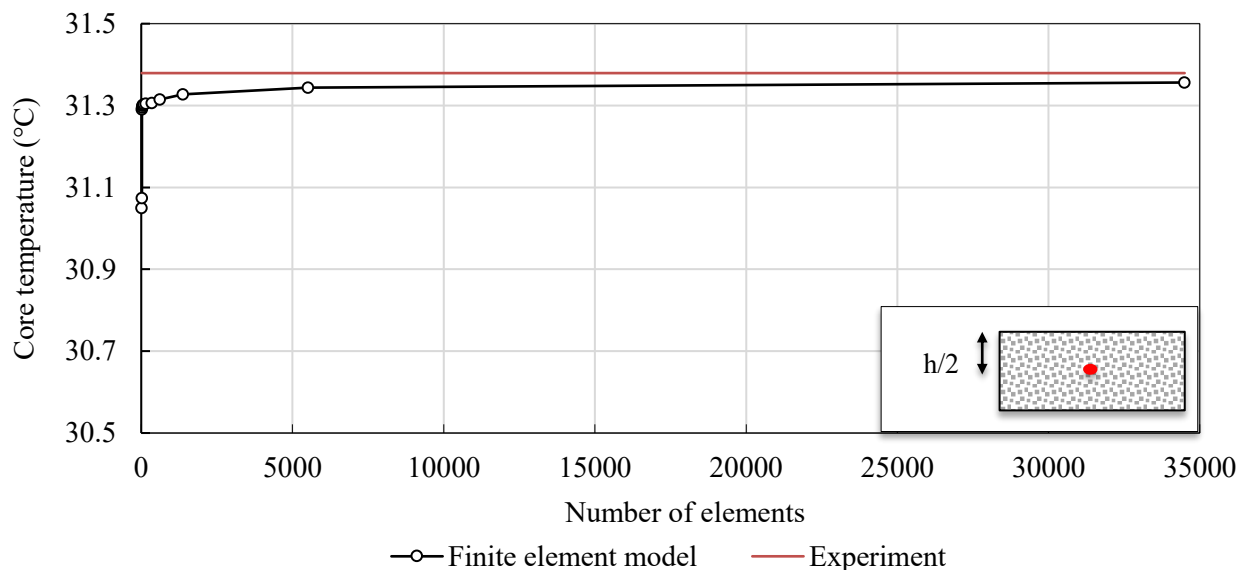
Figure 4-5: Change in result with decreasing element dimensions.
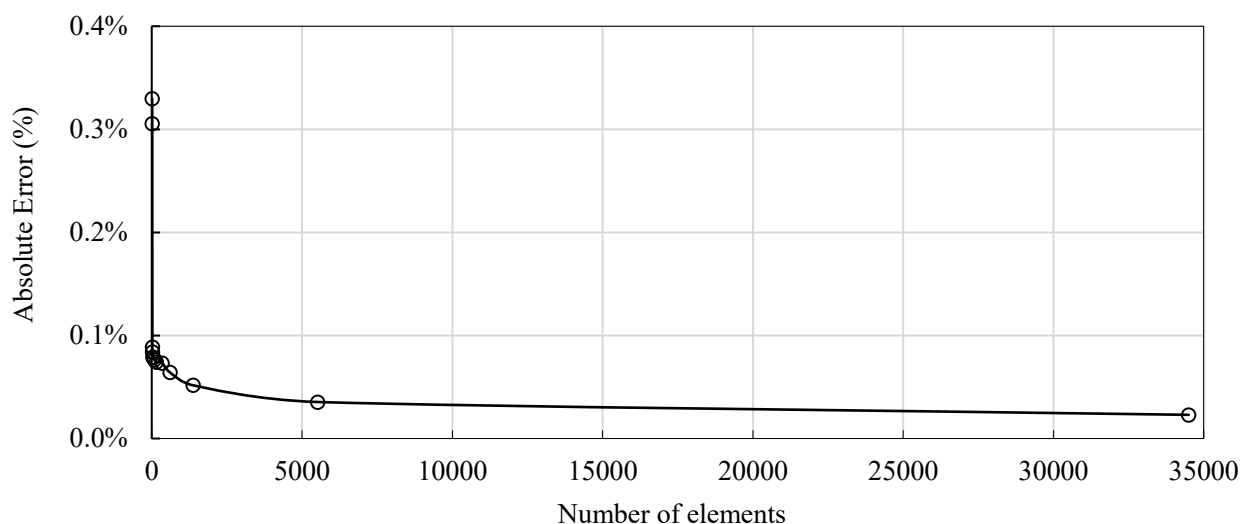
Figure 4-6: Change in absolute error with decreasing element dimensions.

4.9 Finite Element Model Validation

In this section, transient analyses were used to determine the final parameters and perform a verification of the model. The climate data measured hourly at a weather station on an adjacent building were used as inputs to validate and calibrate the model. This data included solar radiation, air temperature, wind speeds and rainfall. Two seasons, summer and winter, were selected for calibration as these would yield maximum and minimum temperatures observed during the analysis period which ranged from January

2018 to July 2018. In each season, a period of at least 7 days was selected for modelling. These weeks were 1 March to 8 March, and 1 July to 9 July. The results of the analyses in summer are shown in Figure 4-7 and Figure 4-8. These results show a good correlation between core temperatures in the physical model and finite element model with absolute errors of less than 2 °C for each surface colour.
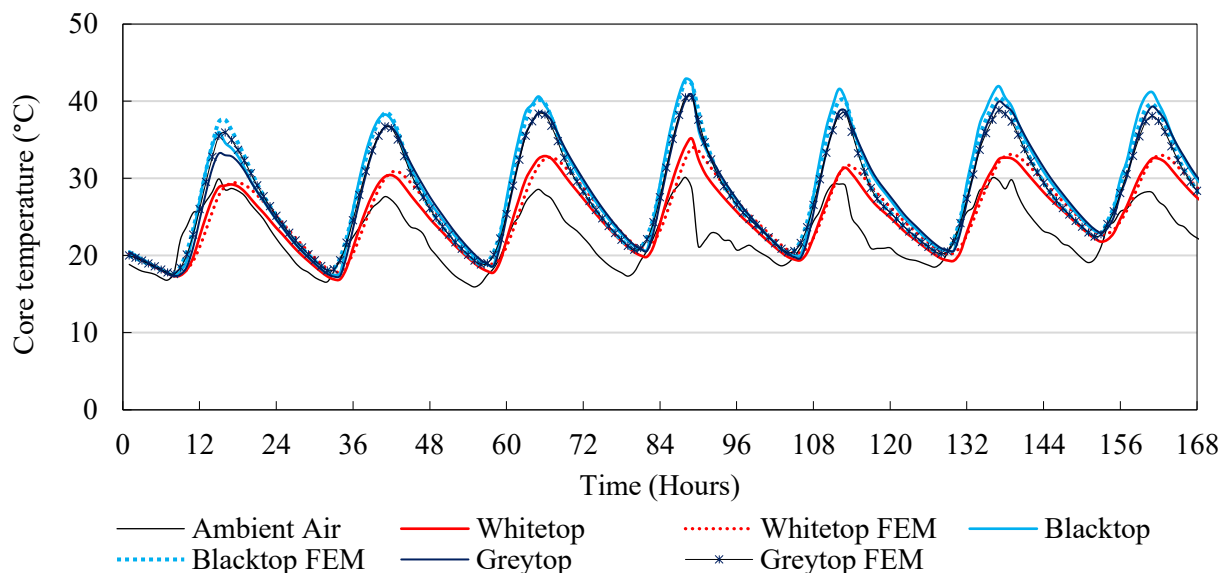
Figure 4-7: Comparison of experimental and simulated results for summer conditions.
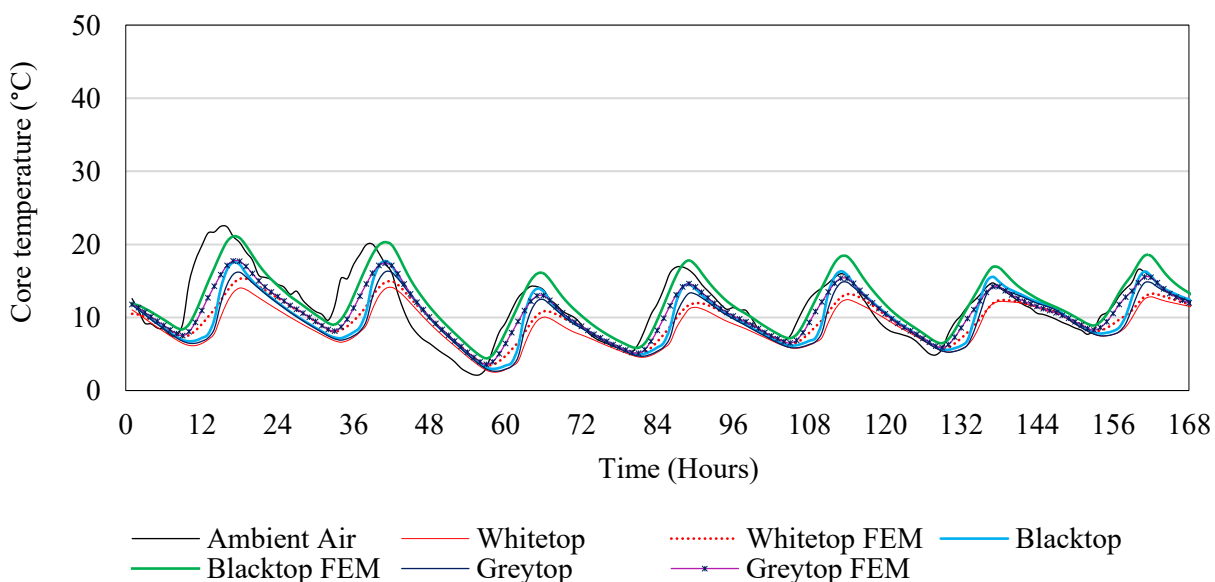
Figure 4-8: Comparison of experimental and simulated results for winter conditions.

It is known that increasing the moisture content of concrete increases the thermal conductivity and density. This is due to the conductivity of water, which fills air voids, being higher than that of air. To study this effect and incorporate it in the thermal prediction model, a partition was made at mid-depth with wet and dry thermal characteristics applied to either section as shown in Figure 4-9. The results obtained from the partitioned model geometry are shown in Figure 4-10. It can be seen that using a cross-section that simulates a dry upper half and moist lower half, improved the simulated results at least 24 hours after the last rainfall event indicating that the concrete beams had undergone a drying and wetting cycle.
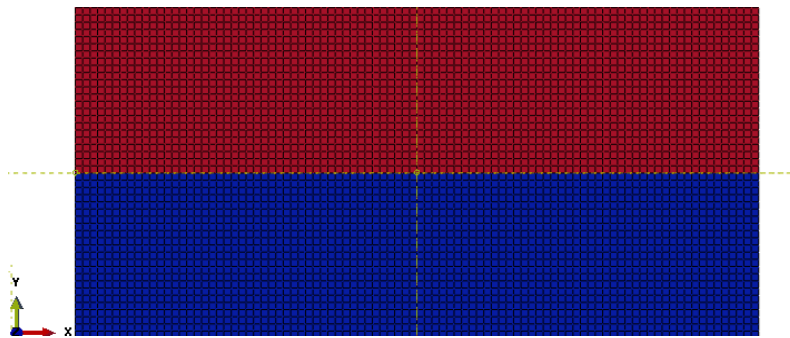
Figure 4-9: Partition for assignment of material properties.
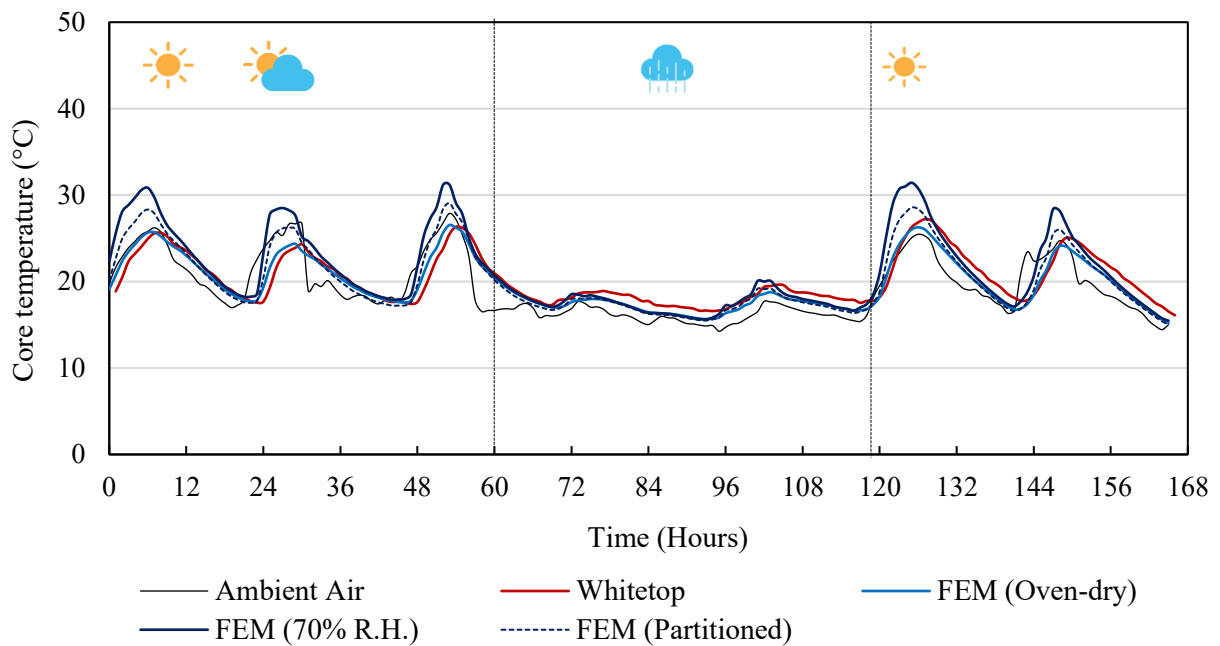
Figure 4-10: Core temperature of whitetop beam in summer when rainfall occurred.

The effect of two climatic input factors on the thermal prediction model output was investigated. During the experimental study, it was observed that solar radiation had the largest effect on the rate of temperature increase and the maximum temperatures measured in the concrete elements. In order to quantify this effect, an analysis was performed with a suppressed solar radiation load. Figure 4-11 shows the results of this simulation where it can be seen that in the absence of solar radiation, core temperatures in the concrete beams would follow a sinusoidal function that converges to the ambient air temperature. Such a trend was observed in Phase II of the experimental study.
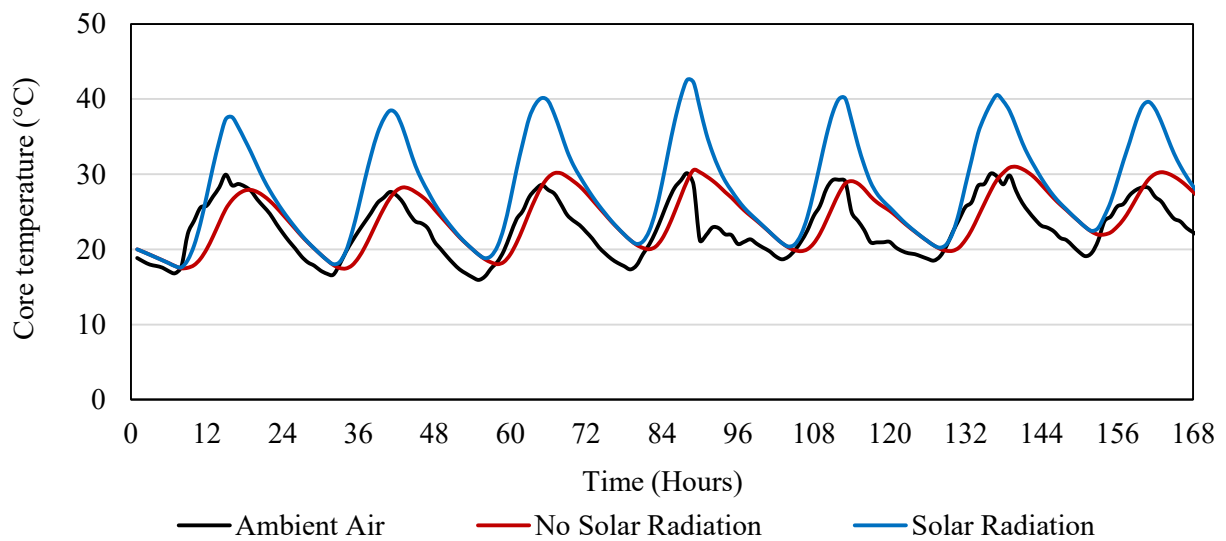
Figure 4-11: Effect of solar radiation load on model output

The second parameter that was investigated was the convective film coefficient. Figure 4-12 shows the effect of the convective film coefficient on the simulated core temperatures. Convective cooling occurs at the concrete-air interface and it is dependent on the free movement of air that is cooler than the concrete surface. When there was no wind movement around the concrete element, surface temperatures increased by up to 10 °C. When the simulated wind speeds were increased such that the convective coefficient was 10 or 20 times higher than the mean, surface temperatures decreased to values that were only 2 °C higher than the ambient temperature.
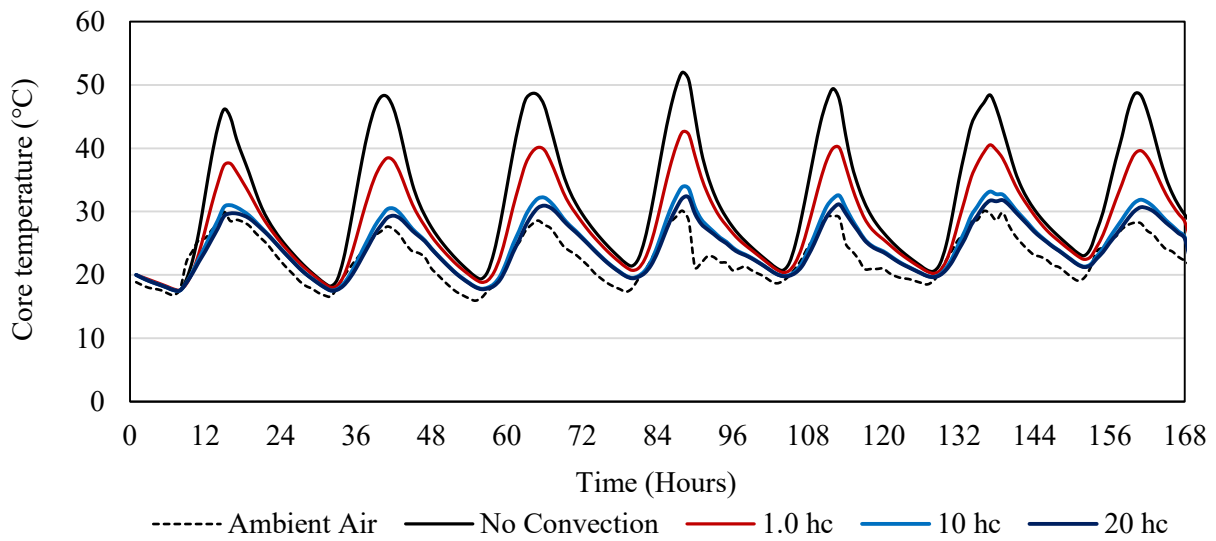
Figure 4-12: Effect of convection interaction coefficient on model output.

Figure 4-13 shows the correlation of core temperatures simulated by the thermal prediction model developed in this Chapter to the temperatures measured during the experimental study from 3 °C to 40 °C. The results show a linear relationship with a gradient of 0.98 and the coefficient of determination, R^2 approaches unity.
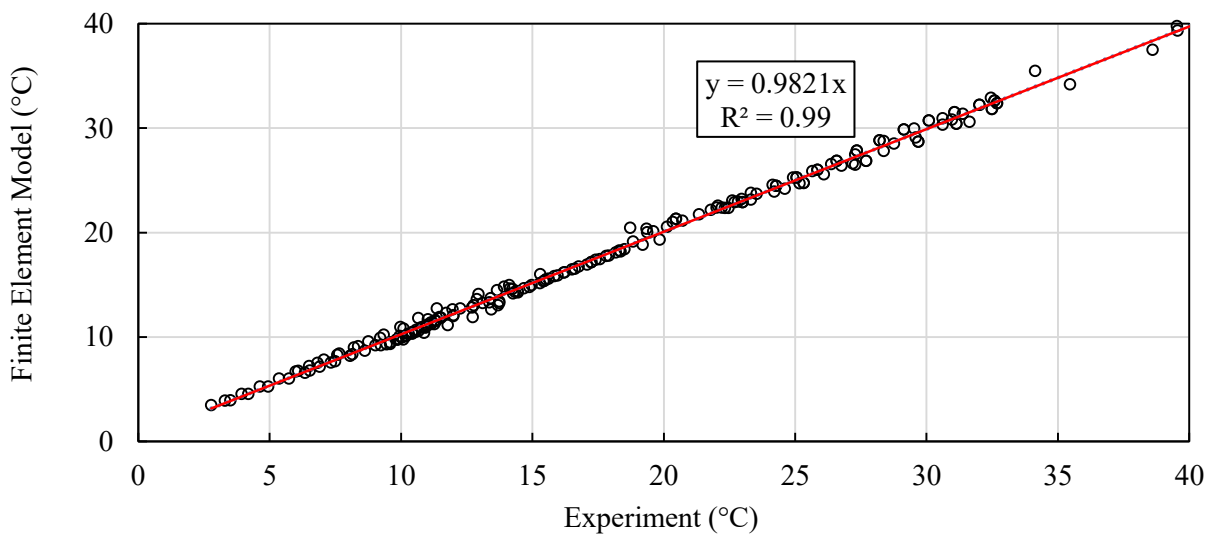
Figure 4-13: Calibration chart for finite element model.

4.10 Summary

Following the experimental program that was presented in Chapter 3, a two-dimensional heat transfer model was developed to simulate the experimental set-up and validated using measured data for internal concrete temperature and climatic factors such as global radiation, ambient air temperature and wind speed. The aforementioned heat transfer model was developed in Abaqus/Standard, an analysis module that forms part of the Abaqus Suite of finite element programs. Loads and interactions representing shortwave and longwave radiative heat transfer, convective cooling, internal conduction, and heat transfer between the concrete and surrounding sand were simulated.

The simulated thermal behaviour of concrete was found to be in good agreement with the experimental data, thus it could be implemented in further investigations with a reasonable degree of confidence. In the following chapters, the capabilities of the model were extended in the form of a parametric study in which the effects of surface colour, thermal mass and the thermal properties of concrete are investigated. Throughout the implementation process the following aspects of the model that were described in this chapter are maintained:

- The type and size of finite elements;
- Surface characteristics of white, black and grey matt acrylic paints, and
- All loads and interactions between the concrete element and the surrounding environment.

Chapter 5   Finite Element Model Implementation

5.1   Introduction

In this chapter, the climatic inputs used in the implementation of the two-dimensional finite element heat transfer model developed and validated in Chapter 4 are described. The advent of the modern computer has resulted in the increased use of numerical simulation methods to negate the economic and analytical limitations of experimental modelling, as well as to predict and optimise engineering systems. In this study, the experimental investigation (Chapter 3) was limited to one concrete mix composition, one concrete beam size, and three surface colours. The purpose of the implementation process was to numerically extend the capabilities of the two-dimensional heat transfer model beyond the simulation of the experimental investigation in order to:

- Improve the understanding of the thermal behaviour of concrete structures and elements exposed to climatic actions, as well as to
- Form a comparative basis for the effect of light coloured surfaces on urban infrastructure with the aim of mitigating global climate change.

In Chapter 6, a parametric investigation was performed in which several aspects of the experimental study were further investigated, including:

- Climatic actions such as global radiation, air temperature, and wind speed;
- The effect of adiabatic heat transfer boundaries;
- Cross-sectional dimensions of the concrete element;
- Thermal properties of the concrete, and
- Surface characteristics, namely solar absorptivity and emissivity.

Idealised daily and seasonal variations of ambient air temperature, global radiation intensity, and wind speed were developed using the climate models discussed in the literature study (Chapter 2) with data measured at a weather station in Pretoria as inputs. Similarly, the seasons considered for the parametric study were summer and winter. Variations in cloud cover, relative humidity and rainfall were not considered, however, the effect of varying moisture conditions that occurs in practice due to wetting and drying cycles were considered.

5.2   Climatic Factors

In this section, the models that were utilised in the idealisation of the climatic input factors for the parametric investigation conducted in Chapter 6 are presented. Climate data measured from January 2018 to July 2018 at a weather station near the experimental site in Pretoria, was used to simplify the daily and seasonal variations of climatic factors that would influence the thermal response of concrete structures and elements such as the beams that were described in the experimental study. The inputs used to represent seasonal variation were solar radiation, ambient air temperature, and the equivalent sky temperature. In order to minimise simulation errors, the idealised sinusoidal cycles were applied repetitively over analysis periods of four days (96 hours). The aforementioned analysis duration was used to ensure that a sufficient number of time steps were provided for model convergence to occur. It was assumed that cloud cover and relative humidity remained constant in both summer and winter, and wind speeds varied cyclically as described in Section 5.2.2. The magnitudes of each climatic factor were calculated using the climate modelling functions described in Section 2.2.

5.2.1 Global Radiation

It is known that global radiation has the largest influence on the thermal variations within concrete structures (Emerson, 1973). This was confirmed by analyses of measured temperature data in the experimental study (Chapter 3). Using Equation 2-5, hourly global radiation intensities were calculated for summer and winter days. The aforementioned model was developed by Gloyne (1972). The magnitudes of total daily global radiation used in Equation 2-4 were 7500 W/m^2 and 4200 W/m^2, and were representative of total daily global radiation calculated by determining the total area under the solar radiation distribution through using numerical integration (see Figure 5-1). The length of a solar day, or time elapsed from sunrise to sunset, was 14 and 12 hours for summer and winter respectively.

The selected inputs were based on solar radiation data that were measured at hourly intervals in the months of March 2018 and July 2018. The calculated input data compared well with experimental data measured during the analysis period. The resulting functions are shown in Figure 5-2.
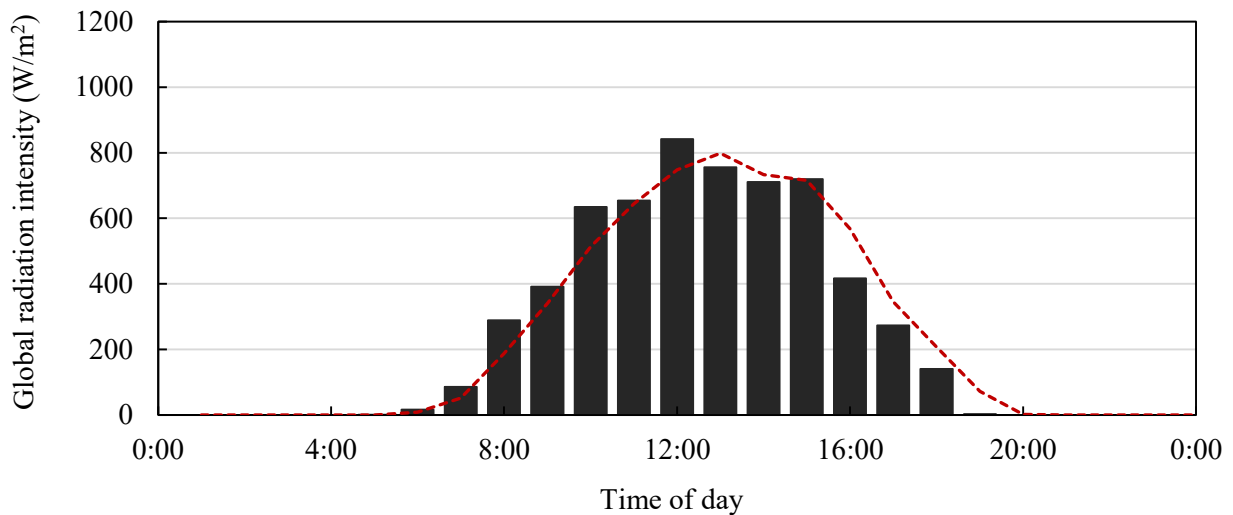
Figure 5-1: Measured hourly solar radiation distribution on a summer day in Pretoria.
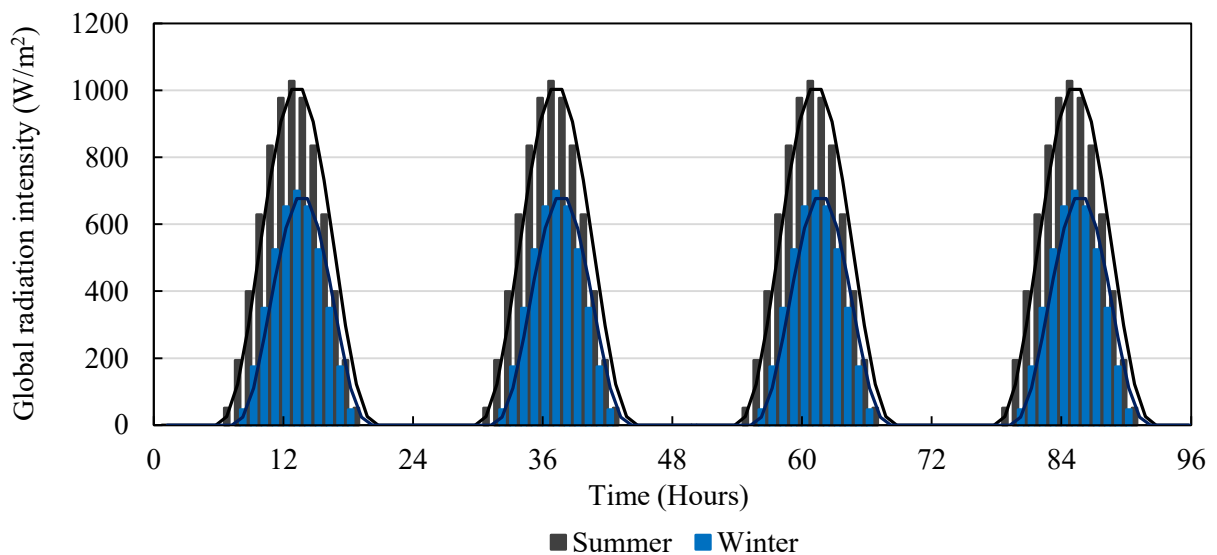
Figure 5-2: Idealised hourly solar radiation intensity for parametric study.

5.2.2 Wind Speed and Convective Heat Transfer

Convection accounts for the heat transfer between warm surfaces and the surrounding air. The random movement of cool air particles near the surfaces of warm objects aids the transfer of thermal energy from the object to the surrounding air by diffusion while advection occurs further away from the surface where air movement is uniform (Incropera et al., 2007). Figure 5-3 shows the average hourly wind speeds measured throughout the duration of the study (January 2018 to July 2018). It can be seen that the average hourly wind speeds formed a random set that typically ranges between 1 m/s and 8 m/s.

This trend was constant throughout the study. Using Equation 2-13 (Larsson and Thelandersson, 2011), these wind speeds result in convective film coefficients between 19 W/m²·°C and 23 W/m²·°C as shown in Figure 5-3. In order to simulate the hourly variation in average hourly wind speed while minimizing non-linearity within the model, a sinusoidal function for the convective film coefficient was calculated using a wavelength of 12 hours, a minimum wind speed of 3 m/s, and a maximum wind speed of 8 m/s. The idealised convection film coefficient is shown in Figure 5-4.
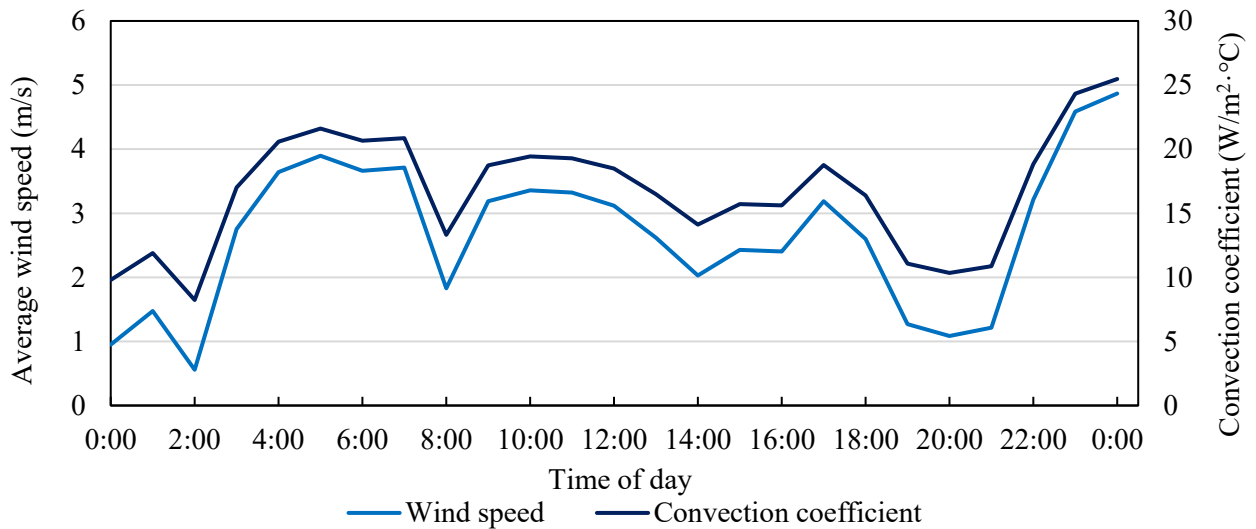
Figure 5-3: Measured hourly wind speed and convection coefficient.
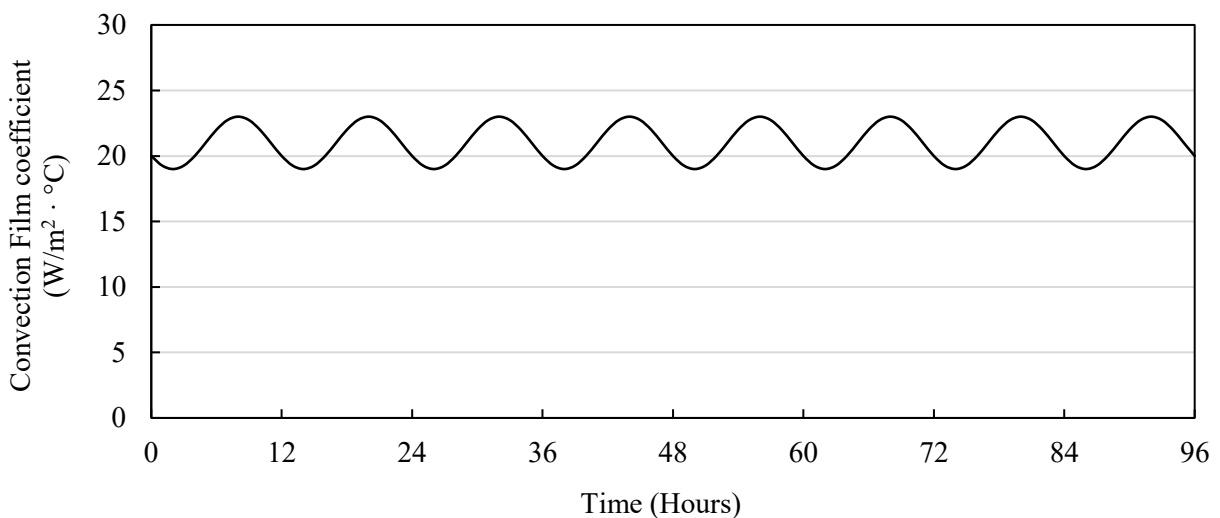
Figure 5-4: Convection coefficient used in parametric study.

5.2.3 Air and Sky Temperature

Idealised sinusoidal air temperatures were determined using Equation 2-10 (Hulsey and Powell, 1993). In this function the maximum and minimum temperatures for summer and winter of 30 °C and 16 °C, and 14 °C and 6 °C respectively were used. The aforementioned temperatures were the average maximum and minimum temperatures recorded in March 2018 and July 2018. The resulting air temperatures for summer and winter are shown in Figure 5-5. The sky temperatures, which represent the temperature of a theoretical surface that absorbs longwave radiation, were calculated from the air temperatures in Figure 5-5 using Equation 2-8 (Larsson and Thelandersson, 2011).
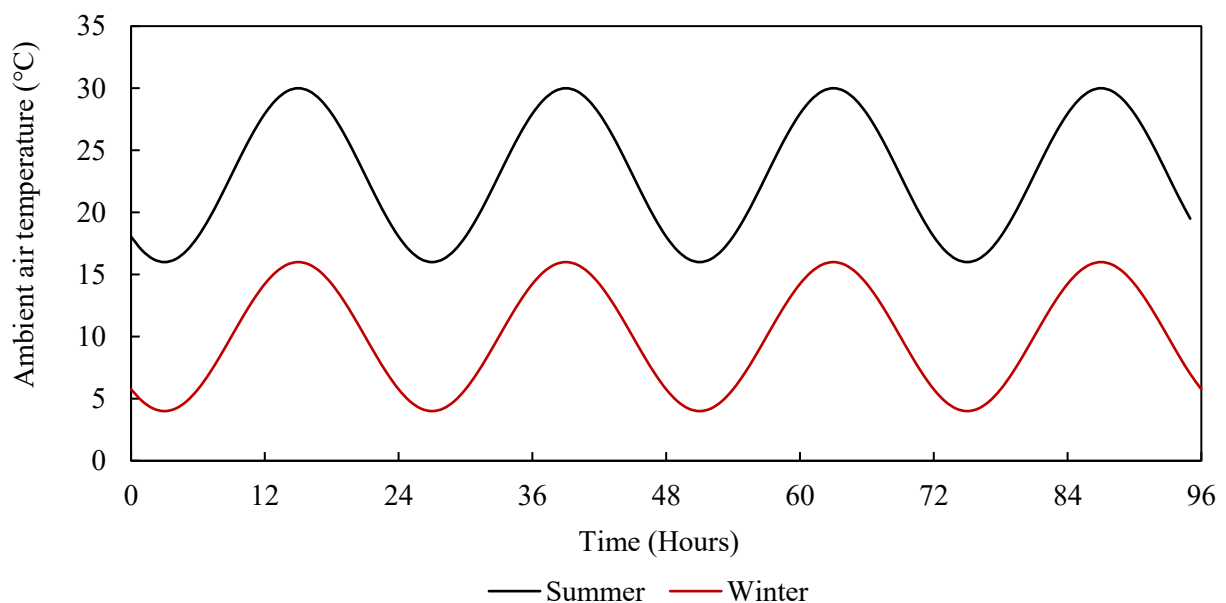
Figure 5-5: Idealised ambient air temperatures used in parametric study.

5.2.4 Concrete-Sand Interface

In the experimental study (Chapter 3), it was seen that the sand temperature 75 mm below the natural surface was approximately 2 °C higher than the ambient temperature in summer and up to 6 °C lower than the ambient air temperature in summer. For the implementation of the heat transfer model, a conditional function was determined such that the sand temperature would vary according to the idealised air temperature. In all analyses in which the sand was assumed to be present, the concrete-sand interface was modelled by applying a surface interaction on the vertical sides of the model with linear interpolation of temperatures. A film coefficient of unity was applied with the average sand temperature applied as the amplitude.

5.3   Summary

This chapter presented descriptions of the idealised climatic inputs that were used in the two-dimensional heat transfer model developed in Chapter 4. Climate prediction models from the relevant published works were used to simplify daily and seasonal variations in solar radiation intensity, air temperature and wind speed. Using these idealised climatic inputs, simulations were performed in order to extend the capabilities of the model beyond the simulation of the experimental study described in Chapter 3. An analysis period of 96 hours and time steps of 1 hour were selected in order to ensure convergence of the model for each combination of parameters. It was assumed that cloud cover and relative humidity would remain constant during the analysis period. In the following chapter, the parameters investigated in the parametric investigation and the results thereof are presented and discussed.

.

Chapter 6   Results Discussion and Analysis

6.1   Introduction

In this chapter, a parametric study of the effects of thermal mass, concrete thermal properties and surface characteristics on the thermal behaviour of concrete elements is presented. The results thereof are also presented and discussed. The capabilities of the two-dimensional model that was developed and validated in Chapter 4 were extended beyond the simulation of the experimental investigation described in Chapter 3. The finite element model developed in Chapter 4 was implemented with baseline material and surface properties as determined during the development phase, and the idealised climatic load factors selected in the previous section. The model simulated a 96 hour period with constant climatic conditions for each of the four diurnal cycles. A total number of 82 variable combinations were considered with only one parameter being varied in each analysis. The effects on the thermal behaviour of adiabatic boundaries, concrete beam dimensions, the thermal conductivity and moisture condition of concrete, daily and seasonal variations in climatic factors, and surface characteristics were simulated.

The effect indicators used included surface temperature changes, effective temperatures, the absolute amplitude of diurnal temperature variations, thermal gradients and the resulting Eigen-stresses in each concrete beam. Using repetitive and idealised climatic conditions, the effect of the following physical parameters on the thermal behaviour of concrete elements were investigated:

- Climatic factors including global radiation, ambient air temperature, and wind speed,
- Cross-sectional dimensions of the concrete element,
- Adiabatic heat transfer boundaries,
- Thermal properties of the concrete, and
- Surface characteristics, namely solar absorptivity and emissivity.

6.2   Climatic Factors

The idealised climatic input factors developed for the implementation of the two-dimensional heat transfer model were described in Chapter 5. Diurnal variations in solar radiation intensity, air temperature, sky temperature and wind speeds were simulated based on climate data measured during the experimental study at a weather station proximate to the experimental site. The climatic inputs were implemented with whitetop concrete elements measuring 0.15 m x 0.23 m.

6.2.1 Global radiation and Air temperature

Figure 6-1 shows the simulated effective temperatures with solar radiation and ambient air temperature inputs corresponding to summer and winter conditions. For the concrete element size and surface characteristics utilised in these simulations, similar trends were observed in summer and winter, however, the effective temperature was 15 °C and 12 °C higher for the maximum and minimum temperatures respectively in summer. This was due to the higher solar radiation intensity and subsequent air temperatures in summer. In both summer and winter, the maximum and minimum effective temperatures occurred at 16:00 and 05:00 respectively. These results showed that under the climatic conditions measured during the experiment, free thermal movement in a whitetop concrete element could be up to twice as large in summer than in winter. Thus consideration must be given where restraint to free movement is present.
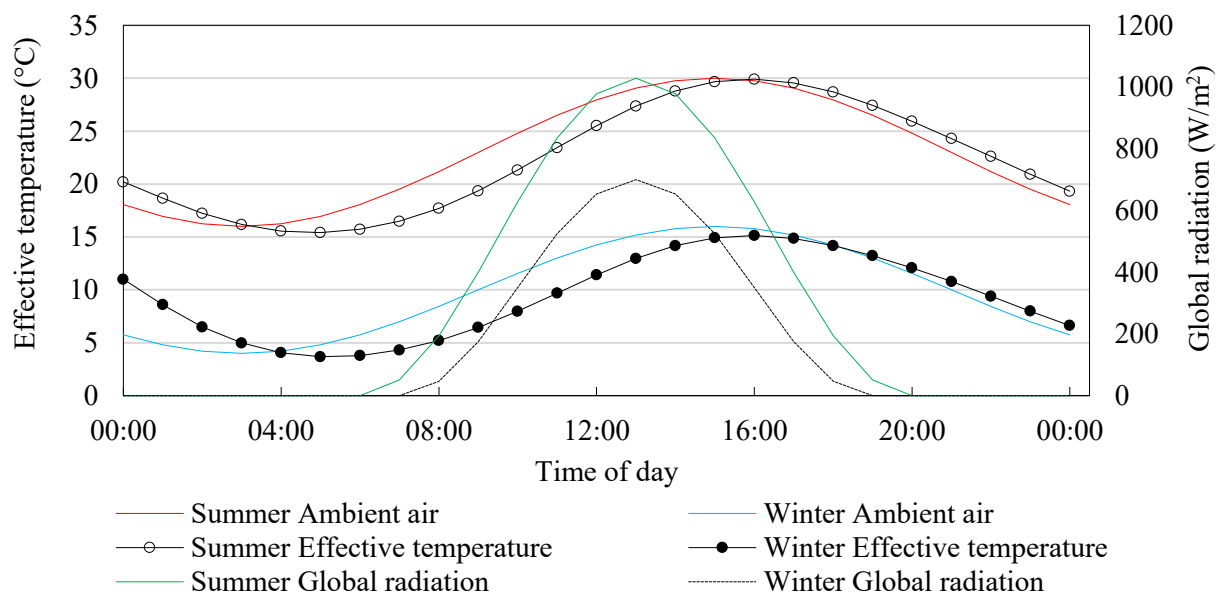
Figure 6-1: Influence of air temperature and global radiation on effective temperatures.

6.2.2 Wind speed and Convection

The influence of wind speed was investigated through simulations with a whitetop concrete element measuring 0.23 m x 0/15 m. Figure 6-2 and Figure 6-3 respectively, show the diurnal variation of surface temperatures with increasing wind speeds as well as the maximum and minimum surface temperatures under summer and winter conditions. These results show that, in summer, increasing the wind speed from 1 m/s to 5 m/s reduced the surface temperature by 14.2 °C, while no change was observed for wind speeds greater than 10m/s. The minimum surface temperature in summer was identical to the maximum surface temperature in winter indicating that at low ambient temperatures, the effect of wind speed was negligible.
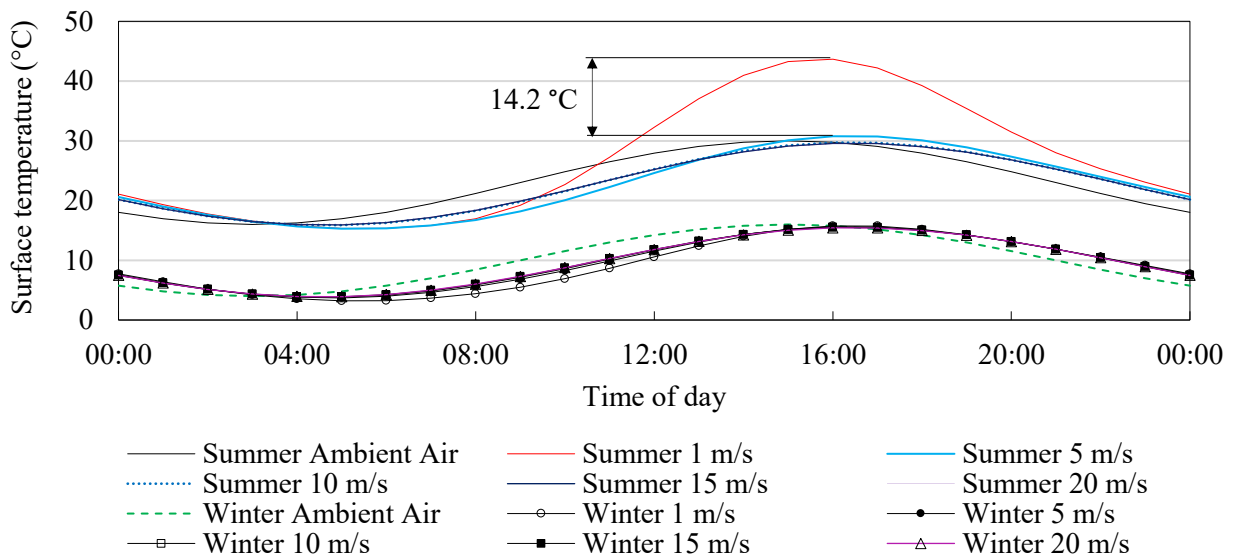
Figure 6-2: Effect of wind speed on surface temperatures in summer.
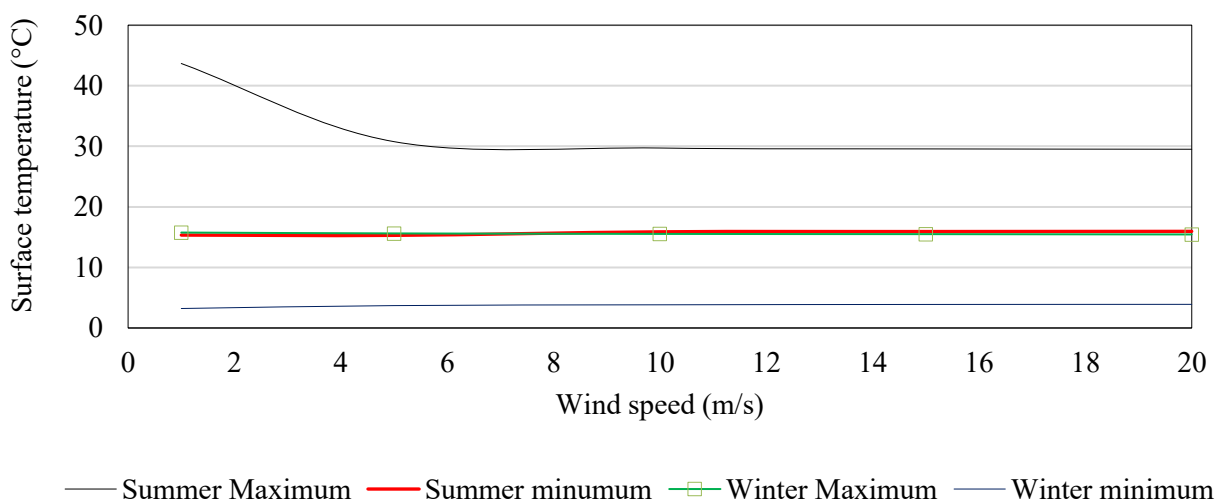
Figure 6-3: Effect of wind speed on maximum and minimum surface temperatures.

6.3   Thermal Mass

A review of relevant literature in Chapter 2 showed that thermal mass or inertia influences the amplitude of temperature variation, rate and quantity of heat gain, and the subsequent amount of heat that is released into the surroundings of a concrete element. The effect of thermal mass was investigated by varying the volumetric heat capacity of concrete elements under idealised summer climatic loads. This was done by varying the cross-sectional width (x) and depth (y) as represented in Figure 6-4. The climatic factors, boundary conditions, and interactions were kept constant while the width of a beam with whitetop surface characteristics and dolomite aggregates was varied from 100 mm to 1000 mm for a constant depth of 150 mm, and the depth was varied from 100 mm to 1000 mm for widths of 230 mm and 1000 mm. The dimensions used are shown in Table 6-1. These ranges of dimensions were selected as they encompass the typical cross-sections of mass and reinforced concrete members used for a variety of applications. These may include slab-on-grade, roof slabs, and bridge superstructures. The primary investigation was performed using the whitetop model, while extrapolation of the physical model was performed on the blacktop and grey models.
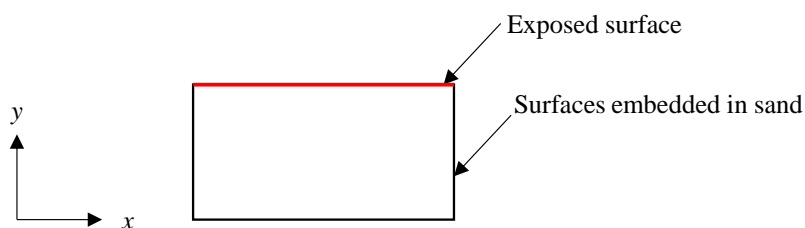
Figure 6-4: Finite element model coordinate system.

Table 6-1: Dimensions used in parametric study.

Depth (mm)	Width (mm)					
	100	230	400	600	800	1000
100		-				-
150	-	-	-	-	-	-
300		-				-
400		-				-
600		-				-
800		-				-
1000		-				-

6.3.1 Concrete Element Width

The effect of cross-sectional width on thermal behaviour of concrete elements was investigated with emphasis placed on the following effect indicators:

- Diurnal temperature variation on the exposed and horizontal embedded surfaces, and
- Full-depth temperature differentials.

The effect of cross-sectional width on effective temperatures, thermal gradients, and the resulting strain and stress profiles were considered in Section 6.3.2 where the influence of adiabatic heat transfer boundaries was also investigated. In these analyses, the effect of increasing the cross-sectional width was investigated on concrete elements with whitetop surface characteristics and a constant cross-sectional depth of 150 mm. A single set of surface colour and cross-sectional depth were used to minimise the effect of other variables such as solar absorptivity or albedo, and vertical heat transfer path lengths in accordance with the coordinate system previously shown in Figure 6-4.

Figure 6-5 and Figure 6-6 show the diurnal variation of simulated temperatures on the exposed and embedded surfaces respectively. A preliminary investigation of these trends showed that the simulated temperatures did not vary significantly from the ambient air temperature. This was likely due to the low solar absorptivity (0.22) or high albedo (0.78) of whitetop surfaces, as well as the limited thermal mass of the concrete elements. Increases of 0.9 °C and 2.0 °C and in maximum temperature were observed for the exposed and embedded surfaces respectively when the concrete beam width was increased tenfold from 100 mm to 1000 mm. The minimum temperatures on the exposed and embedded surfaces were observed to increase by 3.2 °C and 4.3 °C respectively. The aforementioned trends were likely due to the increased amount of global radiation being absorbed as the area of the radiative heat transfer surface increased.

For the characteristics used, the maximum simulated exposed surface temperatures were marginally higher than the ambient air temperature while the minimum exposed surface temperatures of only concrete elements with widths less than or equal to 230 mm were less than the ambient air temperature. This was indicative of the potential benefits of light-coloured surfacing materials, namely: the reduction of ambient air temperatures above large horizontal structures such as roofs and pavements, as well as the reduction of cooling requirements in buildings where whitewashing is used on concrete elements.
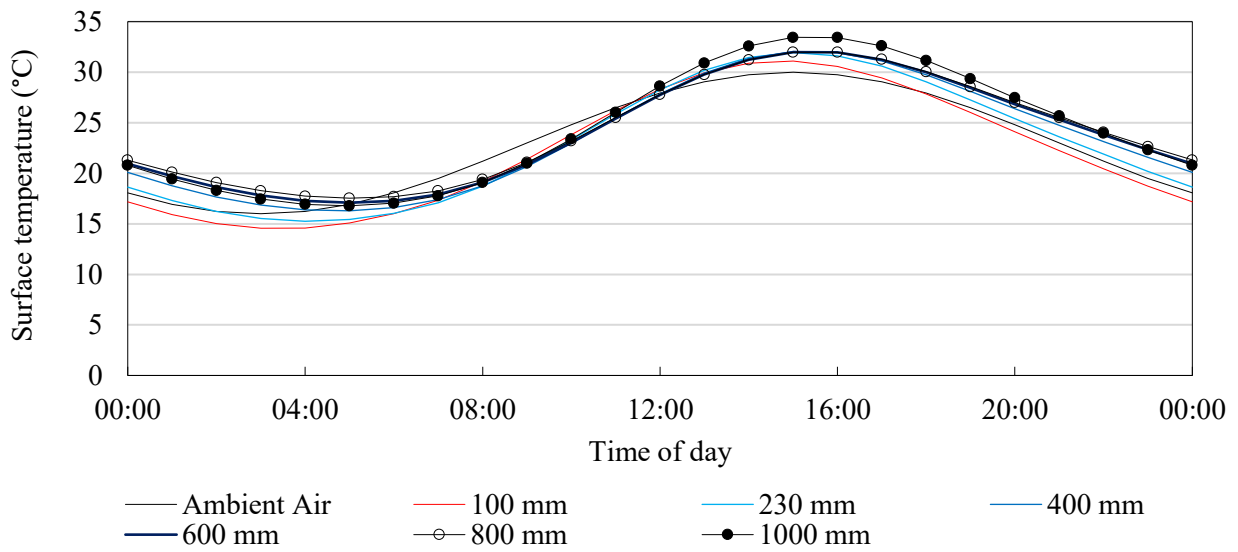
Figure 6-5: Effect of cross-sectional width on diurnal variation of exposed surface temperatures.
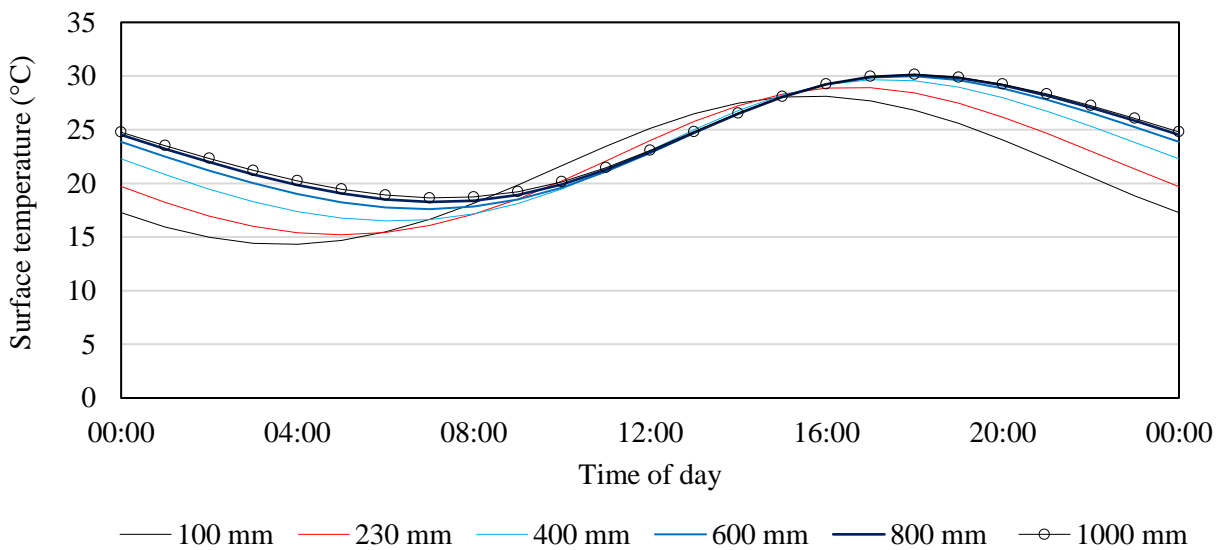
Figure 6-6: Effect of cross-sectional width on diurnal variation of embedded surface temperatures.

Figure 6-7 shows the change in the simulated maximum and minimum temperatures on the exposed (Top) and embedded (Bottom) surfaces. The influence of cross-sectional width on surface temperatures was observed to decrease with increasing magnitude. The change in maximum temperatures was observed to become negligible for widths equal to or greater than 300 mm and 700 mm for the top and bottom surfaces respectively. It was also observed that the maximum top temperature decreased marginally from a peak at a width of 230 mm. This was likely due to increased transfer of heat from the surface to lower layers within the concrete and is indicative of increasing thermal mass.
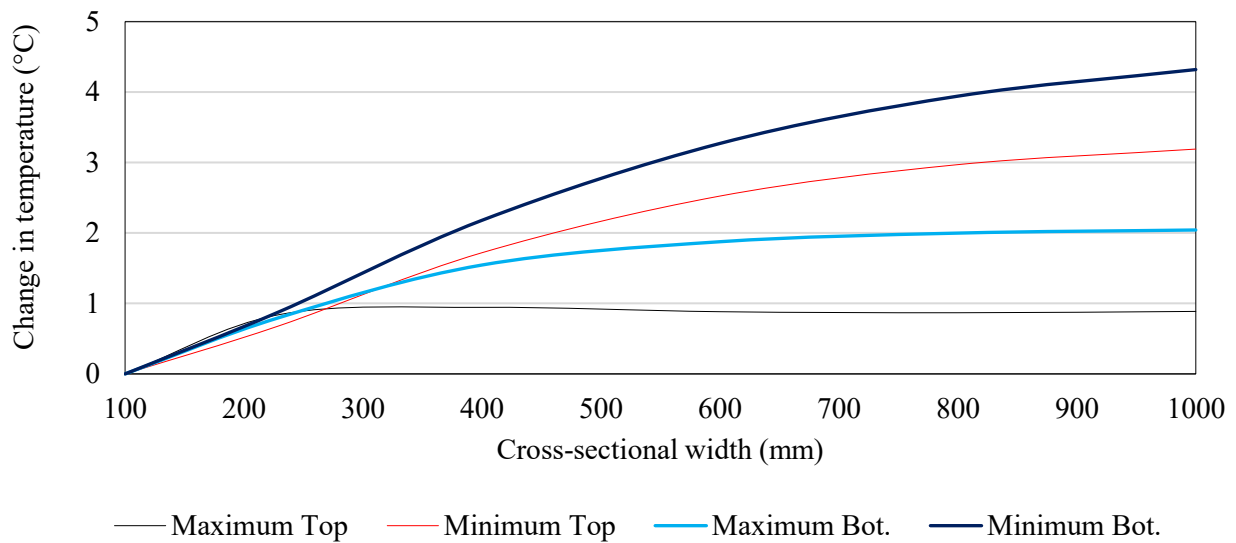
Figure 6-7: Effect of with cross-sectional width on the change in surface temperatures.

Figure 6-8 shows the variation in the absolute temperature difference between the exposed and embedded surfaces. The time lag between the turning points of each curve from 04:00 to 08:00 provided an indication of increasing thermal mass. The largest volume of concrete stored and released the largest quantity of thermal energy thus it had the largest time lag between the maximum and minimum full-depth temperature differentials. However, during heating the lag was visibly reduced as the thermal mass effect was counteracted by an increase in the absorption of global radiation.
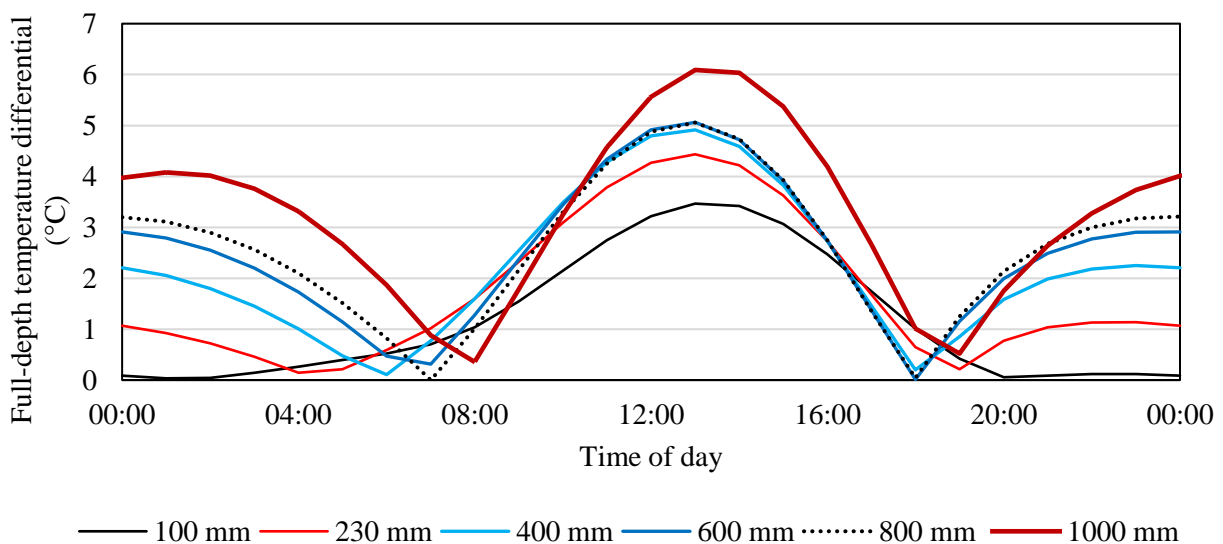
Figure 6-8: Effect of cross-sectional width on absolute full-depth temperature differentials.

The full-depth thermal gradients shown in Figure 6-9, indicate that the average temperature throughout the day increased due the minimum temperatures increasing with width. This increase was due to the increased quantity of thermal energy that was stored and subsequently released as the concrete elements became cooler at night. These thermal gradients were in good agreement with the theoretical basis for the calculation of temperature distributions in concrete elements where it was assumed that thermal gradients were uniform at 08:00 (Emerson, 1973). The uniformity of the aforementioned thermal gradients was observed to increase with increasing cross-sectional width as the effective temperature of concrete elements converged for cross-sectional widths of 600 mm or more. Although the surface temperatures were dissimilar, the convergence effect is also shown by the similarity of the thermal gradients in Figure 6-9(b) and Figure 6-9(c). Additional thermal gradients are shown in Appendix C.

The maximum simulated positive and negative thermal gradients for the depth of 150 mm with whitetop surface characteristics were 0.02 °C/mm and 0.015 °C/mm respectively. These values were significantly lower than the recommended positive and negative design gradients for concrete slabs of 0.033 °C/mm and 0.0533 °C/mm respectively as given in EN-1991-1-5 (CEN, 2004), and 0.055 °C/mm to 0.077°C/mm for concrete pavements (Huang, 2004). This showed that thermally induced cracking was unlikely to occur for the given depth and surface characteristics and this was independent of cross-sectional width. The maximum positive temperature gradients, measured at 16:00 corresponded to thermally induced tensile strains ranging from 13 μm/m to 17 μm/m on the bottom surface and while the maximum negative gradients corresponded to thermally induced tensile strains ranging from 3 μm/m to 17 μm/m on the top surface. Although tensile strain increased with cross-sectional width, these strains were well below the tensile capacity of the concrete of 125 μm/m, and would not result in thermal cracking. The compressive strains developed due to these temperature profiles were negligible.

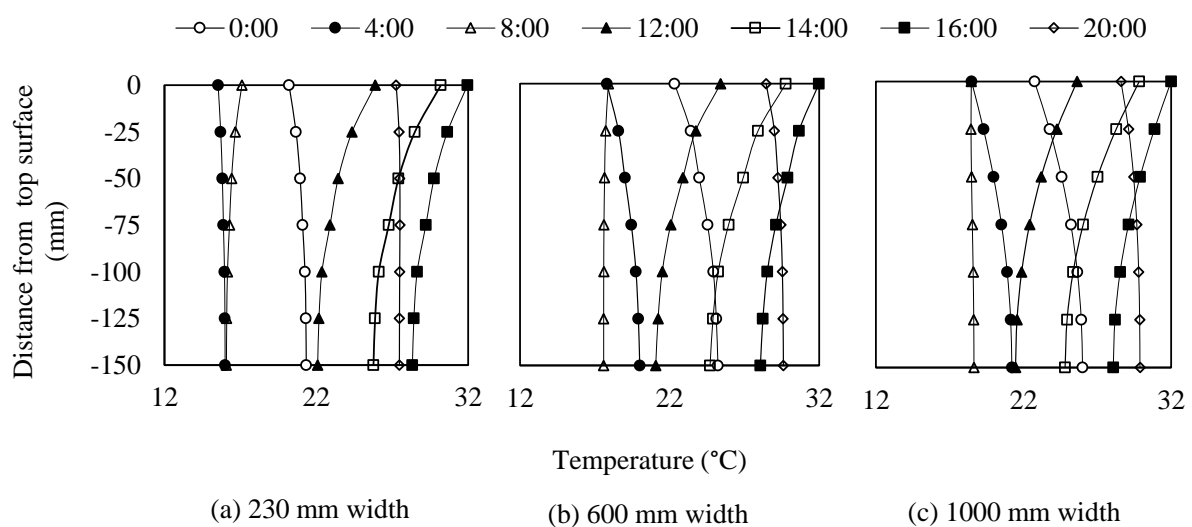
Figure 6-9: Thermal gradients with increasing cross-section width.

6.3.2 Adiabatic Boundaries

An adiabatic boundary between two thermodynamic systems does not allow heat or matter to pass across it. Such a system simulates heat transfer boundary that is infinitely far from the spatial region under investigation or a boundary at which thermal energy is approximately equal on either side thus preventing heat transfer. This is seen in practice in structural elements such as wide concrete slabs, ground beams and foundations, and deep shaded beams on bridges. Adiabatic boundaries were applied to the vertical edges of the finite element model in combination with width and depth changes. The purpose of these analyses was to determine a benchmark for the investigation of thermal mass effects, that is, to determine the concrete element width at which the effects of heat transfer on the vertical edges would become negligible with respect to effective temperature. This would represent the width at which the active heat transfer would simulate the behaviour of adiabatic boundaries. The two-dimensional heat transfer model was implemented with whitetop surface characteristics, width increasing from 50 mm to 2000 mm, and depths from 150 mm to 1000 mm. The effect indicators used were effective temperature variation and full-depth temperature differentials.

Figure 6-10 and Figure 6-11 show the diurnal variation of effective temperature with width for concrete elements with depths of 150 mm and 300 mm respectively. It was observed that for all concrete element depths considered, the diurnal variation of effective temperature reduced with increasing width and depth. For concrete elements with widths equal to or greater than 600 mm, the diurnal range approached that of a concrete element with adiabatic boundaries applied to the vertical edges. This effect increased by increasing depth beyond 300 mm.
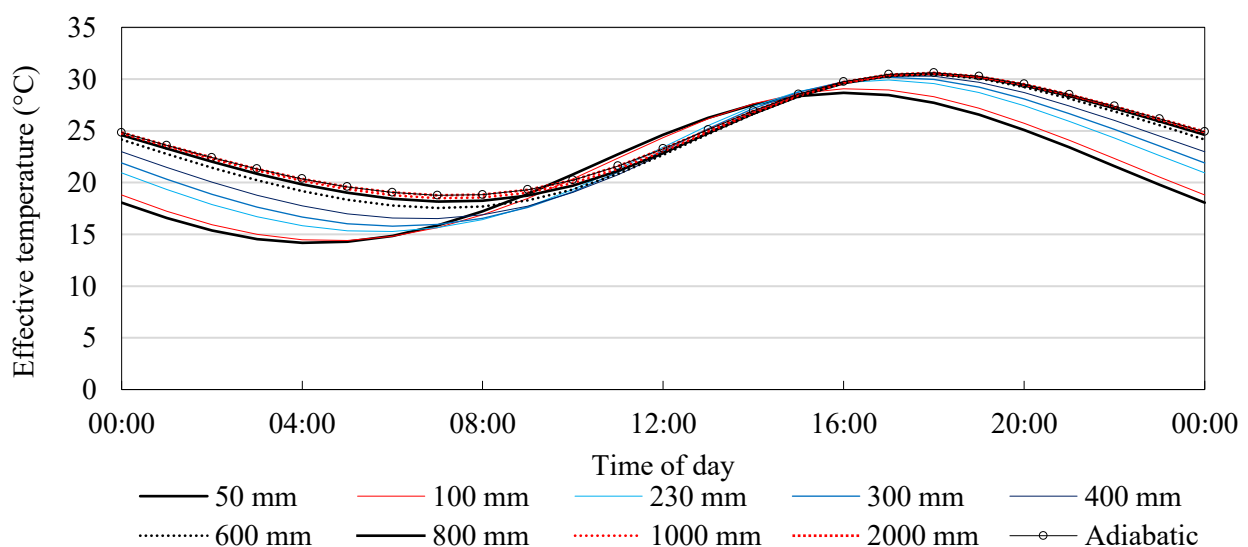
Figure 6-10: Effect of width on the diurnal effective temperature variation for 150 mm deep concrete elements.
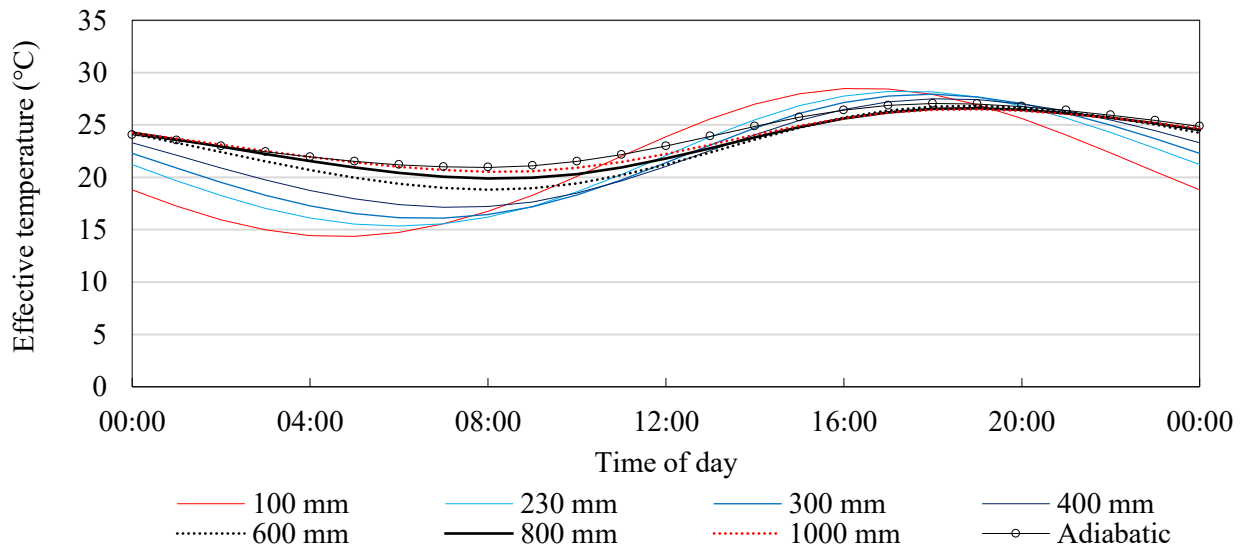
Figure 6-11: Effect of width on the diurnal effective temperature variation for 300 mm deep concrete elements.

Figure 6-12 shows the maximum effective temperature for concrete elements of various depths where the rightmost maximum effective temperatures were simulated with adiabatic boundaries. As previously mentioned, the temperatures approached a constant value for widths of 600 mm or greater. For a depth of 150 mm, the temperature initially increased before stabilising, while the effective temperature decreased and then stabilised for depths of 300 mm and more. The former was likely due to the shorter heat transfer paths between the exposed surface and other boundaries in the 150 mm deep concrete elements.
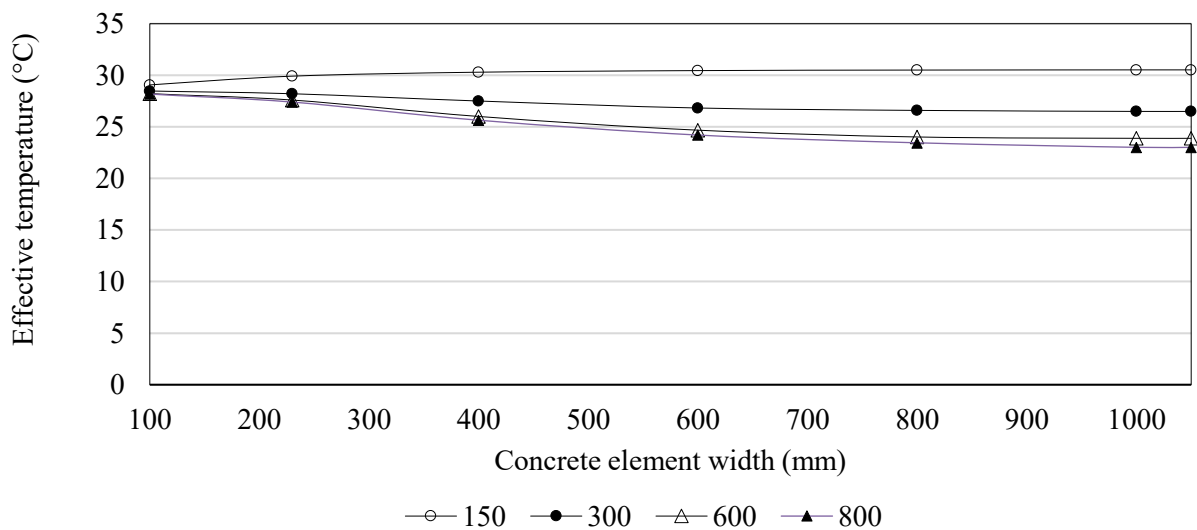
Figure 6-12: Effect of cross-sectional width on the maximum effective temperature.

Adiabatic boundaries were observed to increase the effects of thermal inertia, as shown by the absolute difference between the temperatures in upper (active) surface and the lower surface in Figure 6-13. For section depths larger than 150 mm, the adiabatic boundary increased the time lag from 1 hour to a maximum of 3 hours for a depth of 1000 mm.
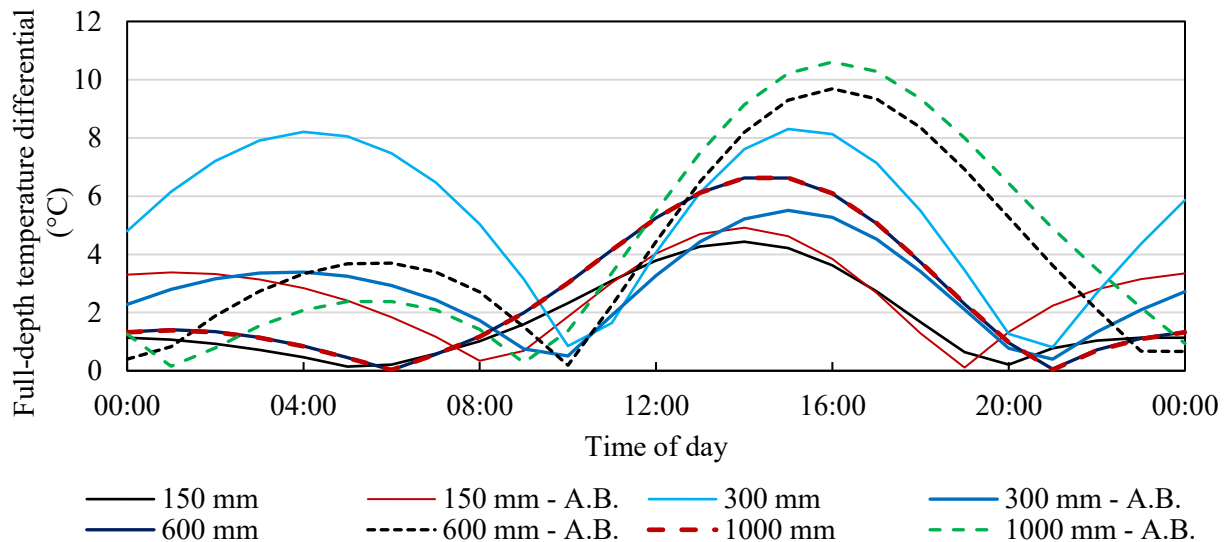
Figure 6-13: Diurnal temperature variation on top and bottom surfaces

It was found that adiabatic boundaries on any surface unexposed to direct solar radiation reduce the overall variation in diurnal temperatures. This reduction effect is further increased by increasing specimen depth. At a depth of 300 mm there is no variation in the bottom surface temperature, while a variation from the uniform mean is observed from approximately the mid-depth towards the exposed surface. Finally, for all widths considered in the investigation, adiabatic boundaries have no effect on beams with depths less than 300 mm.

Following the analyses performed, a width of 600 mm with adiabatic conditions was adopted for the further investigation of the effect of cross-sectional dimensions on the thermal behaviour of concrete elements exposed to climatic factors.

6.3.3 Concrete Element Depth

It was shown in Section 6.3.2 that for cross-sectional widths equal to or greater than 600 mm, heat transfer boundaries on the vertical edges of the concrete element (See Figure 6-12) could be modelled as adiabatic boundaries. Thus, whitetop surface characteristics and constant widths of 230 mm and 1000 mm were used with depth varying from 100 mm to 1000 mm. The aforementioned dimensions were used to compare the effects of the following parameters on thermal behaviour:

- The heat transfer path lengths which were predicted to have greater effects on narrow concrete elements such as columns, and
- Heat transfer on the vertical edges of the heat transfer model which were found to be negligible for cross-sectional widths equal to or greater than 600 mm.

Figure 6-14 and Figure 6-15 show the influence of cross-sectional depth on the diurnal variation of effective temperature for constant cross-sectional widths of 230 mm and 1000 mm respectively. For both cross-sectional widths, the effective temperatures were observed to decrease with increasing depth and were further decreased by increasing width from 230 mm to 1000 mm. In narrow concrete elements (230 mm) there were moderate variations in effective temperature for depths equal to or greater than 300 mm, with the minimum temperature remaining constant.
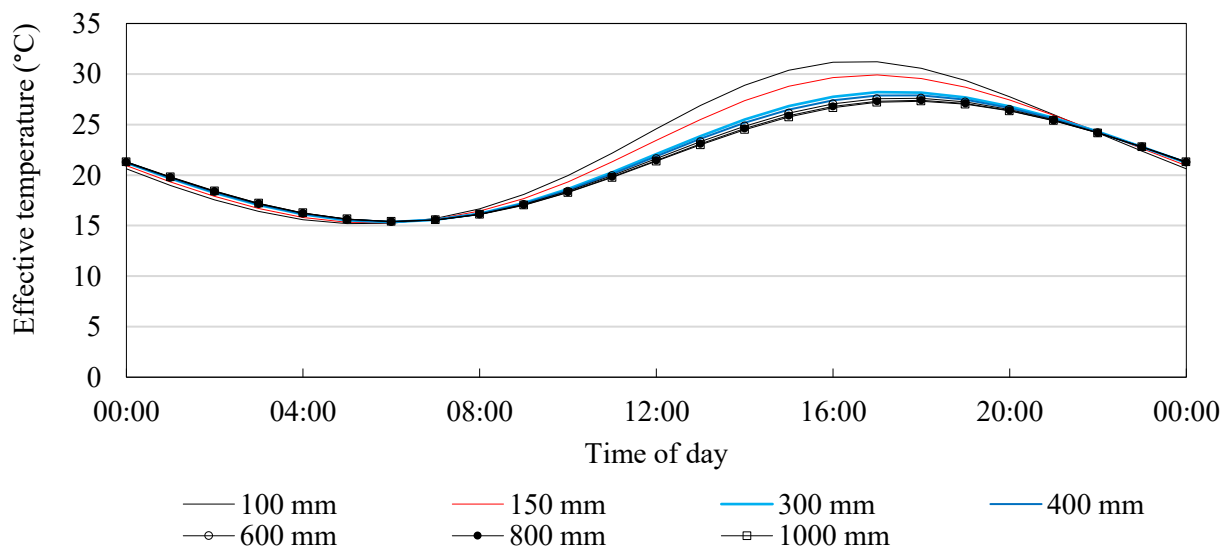
Figure 6-14: Diurnal variation of effective temperature with depth for constant width of 230 mm.

For wider concrete elements, the diurnal variation of effective temperatures significantly decreased for cross-sectional depths greater than or equal to 300 mm and varied moderately for cross-sectional depths greater than 600 mm as shown in Figure 6-15 and Figure 6-16. The maximum effective temperatures decreased with increasing depth and width, approaching constant values for depths greater than 300 mm and 600 mm respectively for widths of 230 mm and 1000 mm. The minimum effective temperatures in the 230 mm wide elements were largely uninfluenced by changes in depth while a moderate increase was observed in the minimum temperatures of the 1000 mm wide concrete elements.
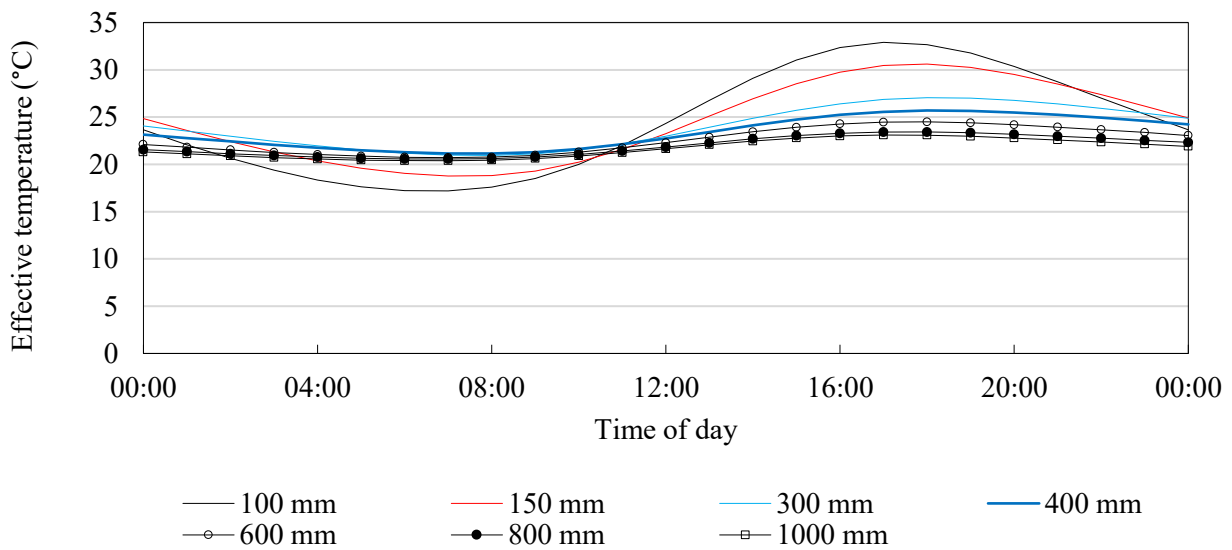

Figure 6-15: Diurnal variation of effective temperature with depth for constant width of 1000 mm.
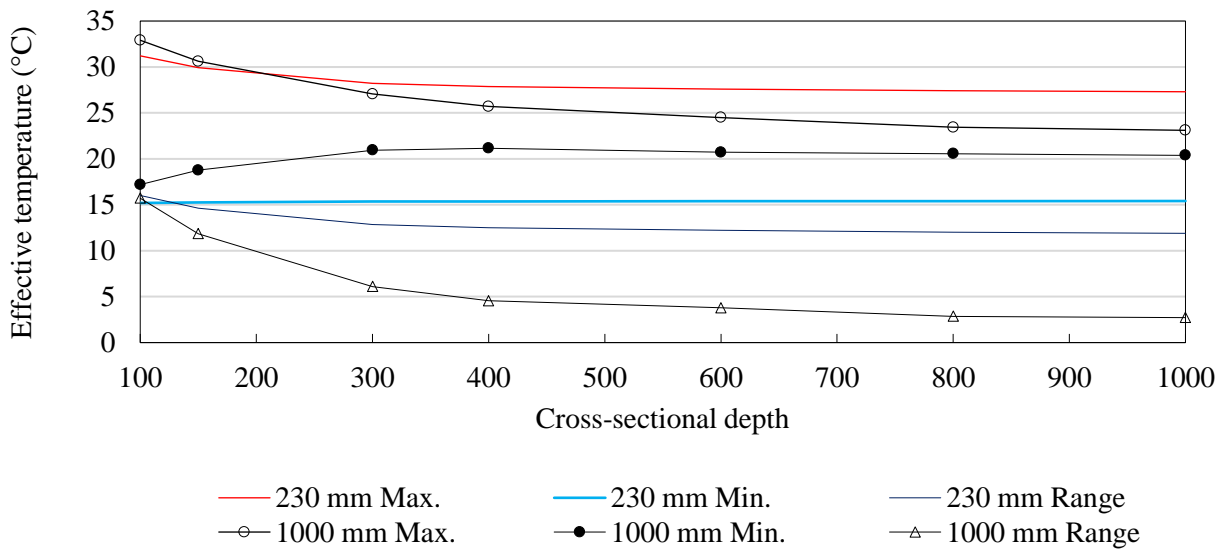
Figure 6-16: Effect of cross-sectional depth on maximum and minimum effective temperatures.

Figure 6-17 shows the influence of cross-sectional depth on the maximum and minimum temperatures on the exposed (top) and embedded (bottom) surfaces of whitetop concrete elements with cross-sectional of 230 mm and 1000 mm. The minimum temperatures simulated on the top and bottom the 230 mm wide concrete element increased by less than 1 °C across the range of cross-sectional depths and were less than the minimum ambient air temperature. The maximum temperatures on the top surfaces of concrete elements with widths of 230 mm and 1000 mm were higher than the ambient air temperature and gradually decreased with increasing depth up to a depth of 300 mm, after which they maintained constant values. For the wider concrete elements, the maximum temperature decreased while the minimum temperatures increased up to a depth of 800 mm where a constant difference of 1 °C was observed. This was indicative of the trends previously shown in Figure 6-15 in which diurnal temperature variation approached a near-constant value.
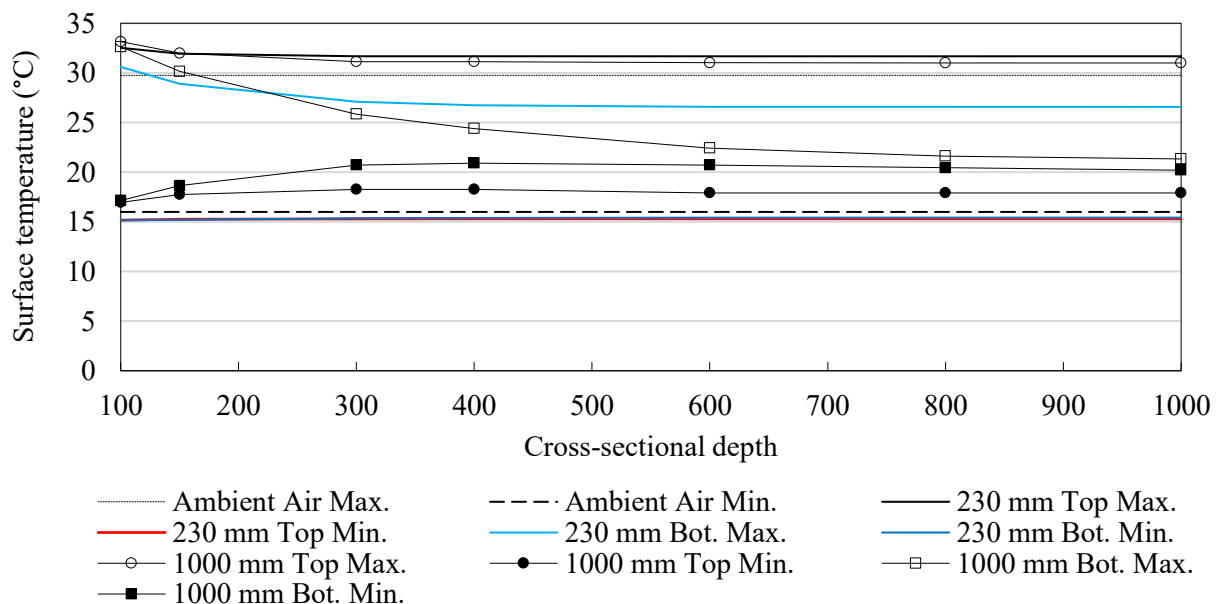
Figure 6-17: Effect of cross-sectional depth on maximum and minimum surface temperatures.

The absolute difference in temperature between the top and bottom surfaces is shown in Figure 6-18. It can be seen that the 100 mm concrete beam varied in temperature by less than 1 °C across its depth. The absolute temperature difference increased with depth, reaching a maximum of 6.5 °C at 16:00 for a depth of 1000 mm. The thermal mass effect is shown by time lags of 3 hours and 2 hours for heating and cooling respectively. The full-depth temperature differential results in the curling and warping of concrete elements. These results show that, while it is mitigated by self-weight, curling and warping would be increased in deep concrete sections and larger longitudinal movements would be observed in thinner concrete sections.
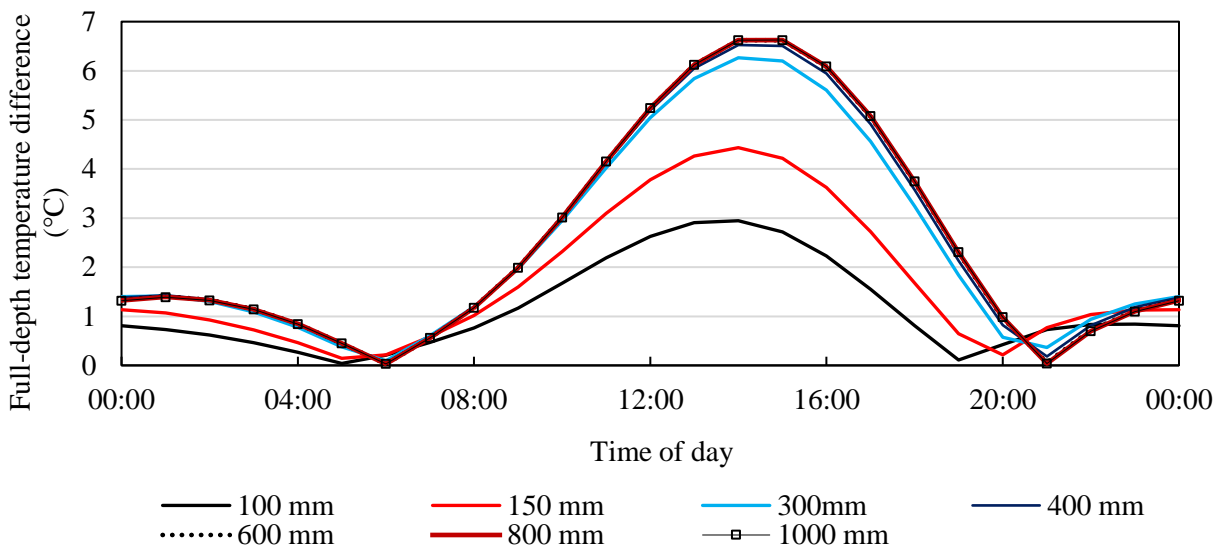
Figure 6-18: Effect of cross-sectional depth on absolute temperature difference between top and bottom surfaces.

Figure 6-19 shows thermal gradients measured in concrete beams with a constant width of 230 mm and depths of 300mm, 600mm, and 1000 mm. A reduction in the peak-to-peak temperature amplitude was observed with increasing depth and is indicated by the converging thermal gradients. This effect was observed to propagate from the bottom surface to the exposed surface. Such a temperature profile would result in a tendency of the beam to curl upward. However, this would be mitigated by increasing self-weight. For wider specimens, the bandwidth reduction effect was more pronounced.

Figure 6-20 shows thermal gradients measured in concrete beams with a constant width of 1000 mm and depths of 300mm, 600mm, and 1000 mm. The simulated thermal gradients that are not included in Figure 6-20 are shown in Appendix C. When the width of a 400 mm deep section was increased from 230 mm to 1000 mm, the change in temperature reduced from 10 °C to 4°C. In sections with depths from 600 mm to 1000 mm, there was little (0.5 °C) change in temperature from depths of 300 mm. The thermal gradients resulted in the thermally induced strains as shown in Table 6-2, for each tensile strain the corresponding compressive strain on the opposite face of the concrete element is shown in parentheses. The tensile strains were well below the tensile capacity of the concrete and would, therefore, not result in cracking of the concrete sections.

(a) 300 mm depth   (b) 600 mm depth   (c) 1000 mm depth
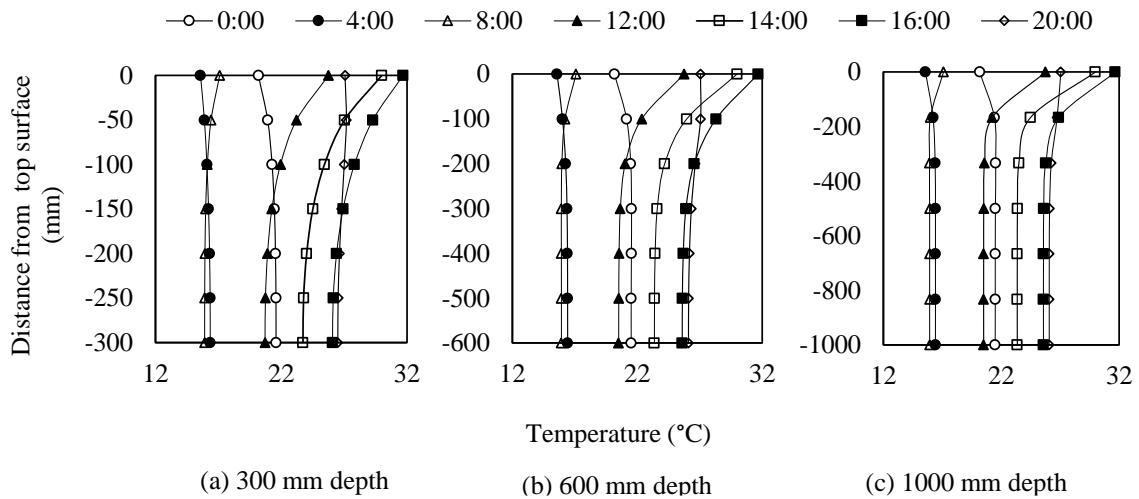
Figure 6-19: Change in thermal gradients with increasing depth for 230 mm width.

(a) 300 mm depth   (b) 600 mm depth   (c) 1000 mm depth
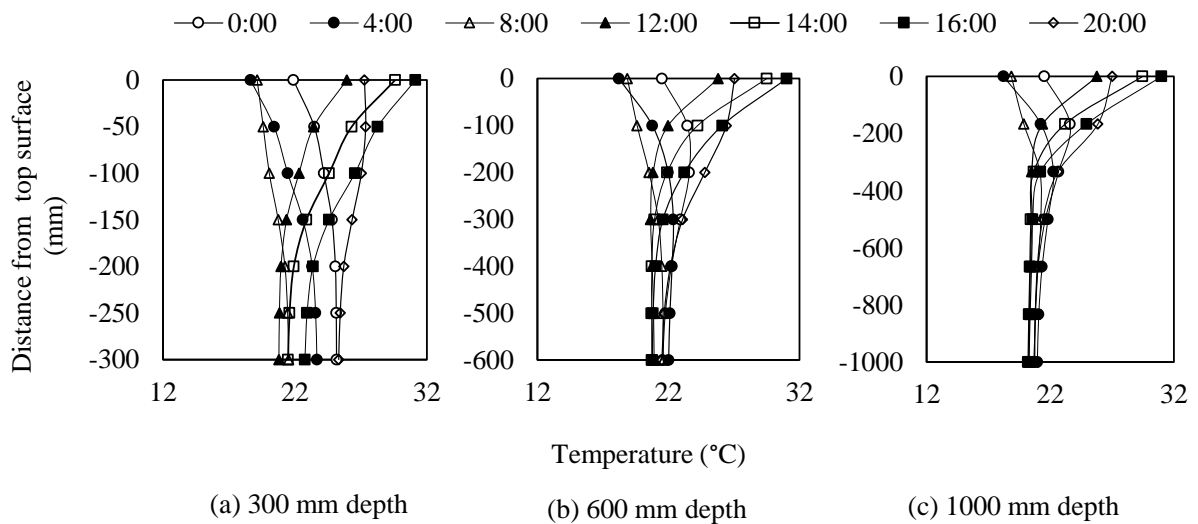
Figure 6-20: Change in thermal gradients with increasing depth for 1000 mm width.

Table 6-2: Influence of cross-sectional dimensions on maximum strains in whitetop concrete elements.

Width	Positive thermal gradient			Negative thermal gradient		
	300	600	1000	300	600	1000
230	48 (1.3)	23 (4)	57 (10)	17.6 (2.1)	27 (3)	57(10)
1000	24(53)	18.5 (65)	17.9 (70)	31.5 (16.3)	30.0 (5.9)	26.32 (0.3)

6.4 Thermal Properties and Moisture Condition

The influence of thermal properties and moisture condition on the thermal behaviour of concrete elements was investigated by varying the relevant parameters from the baseline parameters used to develop the finite element heat transfer model in Chapter 4. The thermal conductivity, density, specific heat and the thermal expansion coefficient of the material used in the model were varied to those of normal-weight concrete produced with four widely used aggregate types. The aggregate types were selected to provide a range from low to high density, thermal conductivity, and thermal expansion. Although the specific heat of normal-weight concrete does not vary significantly at normal working temperatures, this property was changed to accurately model properties of concrete produced with each aggregate type.

Concrete that is exposed to climatic variations seldom exists in a constant hygrothermal state: the relative humidity of atmospheric air is highly variable while drying and wetting cycles occur when concrete is exposed to rainfall or varying phreatic levels in structures installed underground. The effect of moisture content was investigated through the use of published thermal characteristics of concrete in two states, namely, the bone-dry state and the wet state (above 80% relative humidity). Table 6-3 shows the thermal characteristics of the four aggregates types selected for implementation were determined through an extensive literature review in Chapter 2.

Table 6-3: Variation in concrete properties with aggregate type

Aggregate	Density (kg/m^3)		Specific heat (J/kg·°C)		Thermal conductivity(W/m·°C)	
	Dry	Wet	Dry	Wet	Dry	Wet
Dolomite	2460	2600	880	910	2.50	2.70
Granite	2350	2420	880	900	2.50	2.60
Limestone	2020	2440	700	800	1.40	2.20
Quartzite	2500	2600	900	920	2.70	4.10

The abovementioned thermal properties were assigned to the two-dimensional heat transfer model with cross-sectional dimensions measuring 0.23 m x 0.15 m and whitetop surface characteristics. The diurnal variation of the simulated effective temperatures for the abovementioned concrete types is shown in Figure 6-21. It was found that changing the aggregate type with thermal conductivity ranging from 1.4 W/m·°C to 4.1 W/m·°C had no observable effect on the effective temperature calculated over 24 hours.
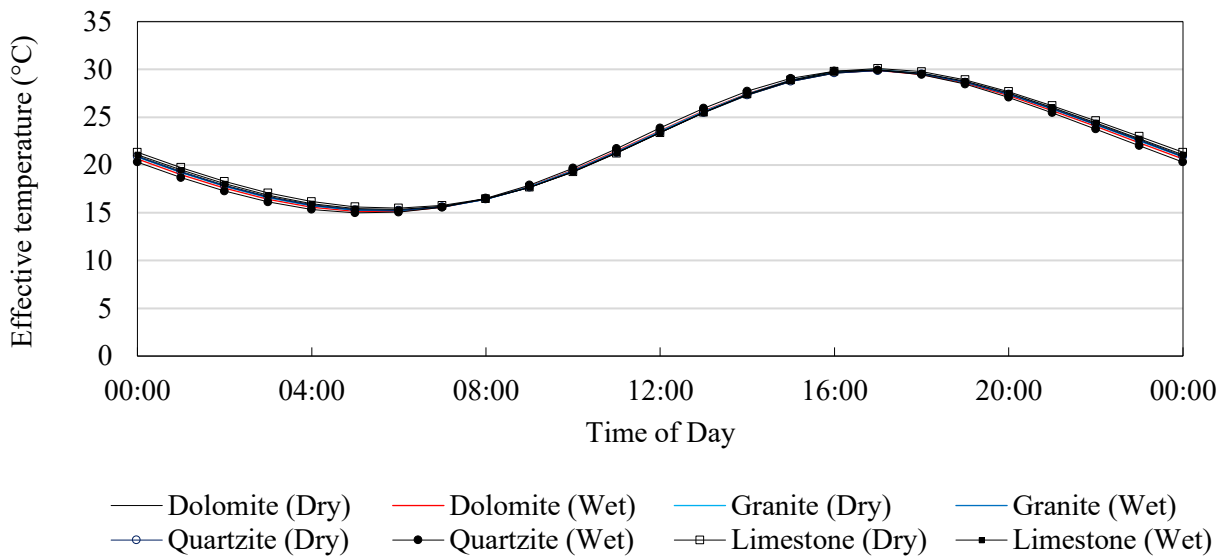
Figure 6-21: Diurnal variation of effective temperature for different aggregate properties.

Figure 6-22 shows the diurnal variation of simulated surface temperatures on the exposed (top) and embedded (bottom) surfaces. When thermal conductivity increased, the temperatures near the lower surface were increased due to the increased rate of heat transfer from the upper boundary through the depth of the section. Subsequently, the temperatures near the exposed surface were decreased resulting in a reduction of the absolute temperature difference between the top and bottom surfaces as shown in Figure 6-23. For the concrete aggregate types, surface characteristics, and cross-sectional dimensions used, it was observed that the minimum temperatures on both surfaces were not affected by aggregate type.
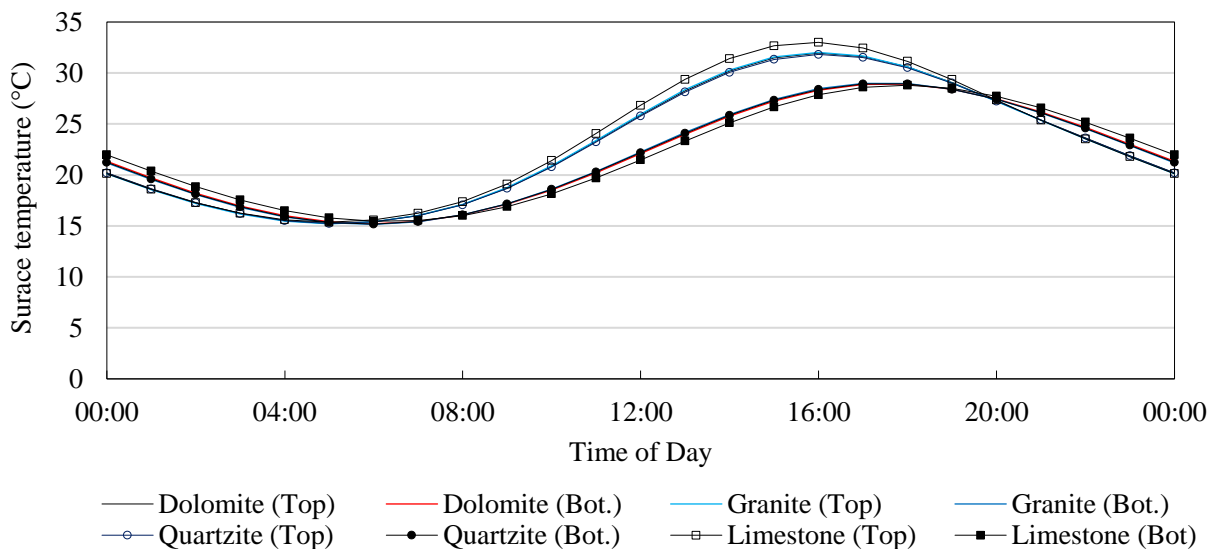
Figure 6-22: Effect of concrete aggregate type on surface temperatures.
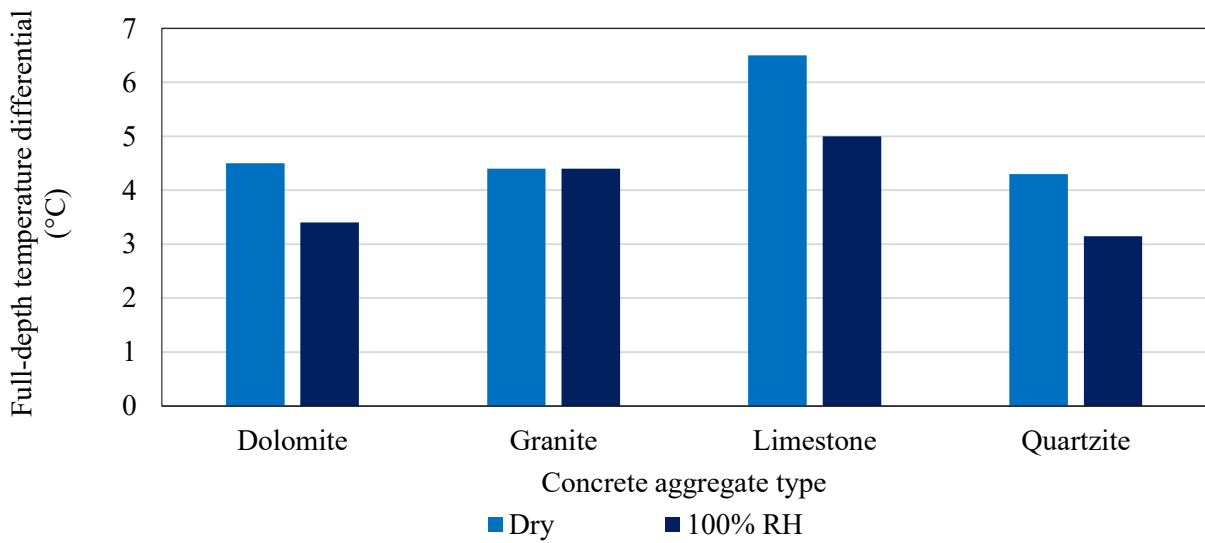
Figure 6-23: Maximum temperature difference between top and bottom surfaces.

When the thermal properties of moist concrete were varied, minimum temperatures decreased. This was likely due to water having specific heat higher than air, resulting in greater energy demands to increase temperature. An increase in effective temperatures of 1 °C was observed between 04:00 and 08:00. For the aggregate types considered, increasing conductivity and specific heat were observed to reduce the full depth temperature differential by up to 3 °C as well as increasing the uniformity of thermal gradients as shown in Figure 6-24. Additionally, the thermal gradients simulated with the complete range of thermal properties are shown in Appendix C. For a concrete element with whitetop characteristics, the aforementioned temperature differentials correspond to thermal gradients of 0.04 °C/mm and 0.02 °C/mm, which are well below recommended design gradients.
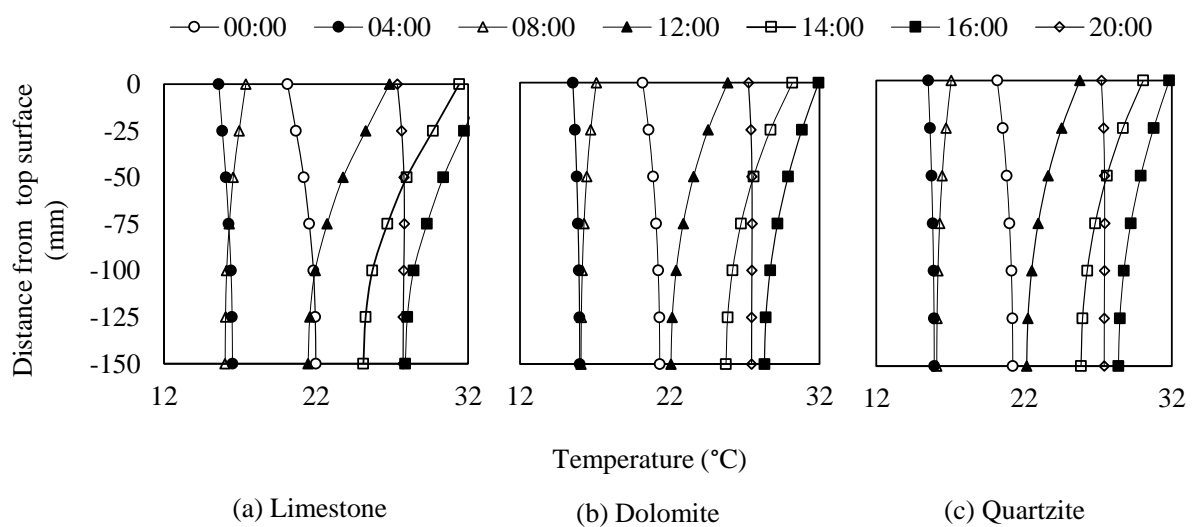
Figure 6-24: Effect of concrete aggregate type on thermal gradients.

6.5 Surface Colour

In the preliminary simulation of the experimental study discussed in Chapter 4, the thermal behaviour of three concrete beams was simulated using the solar absorptivity and emissivity characteristics of white, black and grey paint only. In this section of the parametric study, the two-dimensional heat transfer model was extended to encompass a greater range of surface characteristics. The influence of surface colour on the thermal response of concrete elements under climatic loading was investigated by varying the solar absorptivity, or albedo, and the emissivity characteristics on the exposed surface the two-dimensional heat transfer model. For either parameter, values ranging from 0.001 to 1.0 were implemented while the other characteristic was maintained at a constant value. A solar absorptivity of 0.001 was representative of a transparent surface while the solar absorptivity of 1.0 represented a perfect blackbody respectively. These analyses were performed to form a comparative basis for the use of light coloured surfacing on engineering structures. The emissivity characteristic was expected to influence minimum temperatures in concrete structures which would result in thermally induced internal restraint and cracking as discussed in the literature study (Chapter 2). This section presents a discussion of the effects of surface colour, which is numerically represented by solar absorptivity and emissivity. These results are presented with emphasis on the effects of solar absorptivity.

6.5.1 Solar absorptivity

The solar absorptivity of a surface is a non-dimensional parameter that is calculated from the albedo, or reflectivity, r which represents the ratio of reflected light to the total available light. Conversely, the solar absorptivity is the ratio of absorbed light to the total available light. In Chapter 4, the thermal behaviour of three concrete beams measuring 0.23 m x 0.15 m with a unit length was numerically simulated. The solar absorptivity and emissivity characteristics for white, black and grey acrylic matt paint were assigned to the model surface subjected to radiative heat transfer. In these analyses, a constant emissivity factor equal to 0.85 was applied to the radiative heat transfer boundary and the effect of surface texture was neglected. Similarly, the analyses performed in this section were performed with a constant emissivity of 0.85 and solar absorptivity ranging from 0.001 to 1.0. The effect indicators used were surface temperature, full-depth temperature differentials, effective temperatures, and thermal gradients. These effect indicators are presented in the aforementioned sequence.

Figure 6-25 shows the diurnal variation of temperatures on two surfaces of concrete beams measuring 230 mm x 150 mm: the exposed (top) surface and embedded (bottom) surface. The maximum simulated temperatures on both surfaces were highest for the blacktop beam which had a solar absorptivity of 0.95, and lowest in the whitetop beam with an assigned solar absorptivity of 0.22. A comparison of the blacktop and whitetop beams showed that the maximum temperatures calculated for the blacktop beam were 14 °C and 6 °C higher for the top and bottom surfaces respectively higher. Differences of 3 °C and 1.3 °C were observed between blacktop and greytop beams for the maximum top and bottom surface temperatures respectively. This was attributed to the absorptivity of the grey beam being only 17% less than that of the blacktop beam. Solar absorptivity, however, had no observable effect on the minimum temperatures of both surfaces.
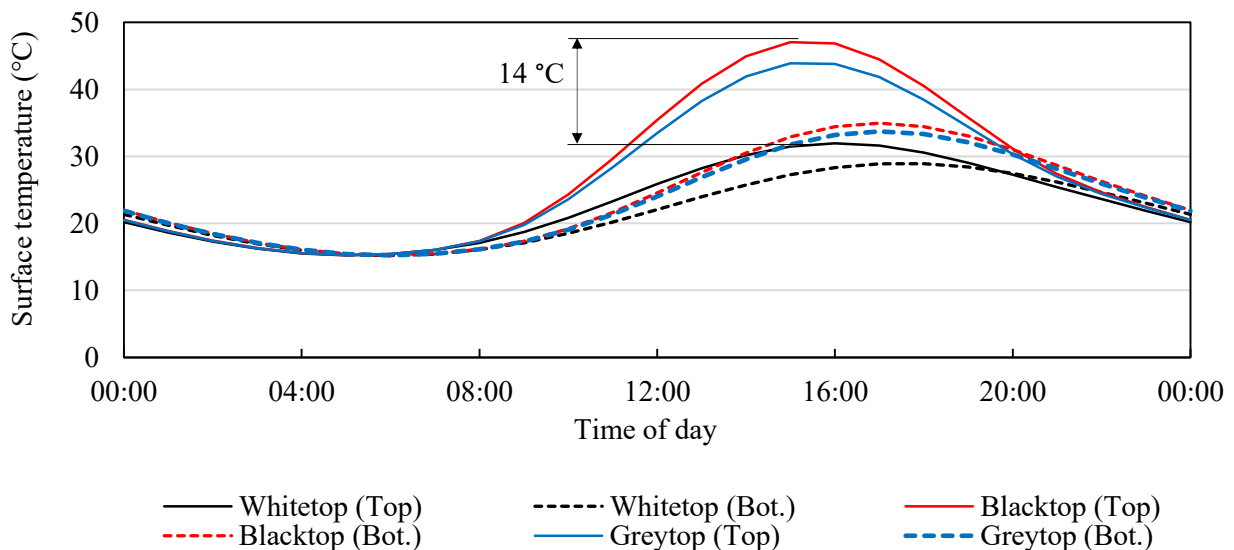
Figure 6-25: Effect of surface colour on the diurnal temperature variation on top and bottom surfaces.

The previous results were extended to encompass the complete range of solar absorptivity characteristics. A total of eleven transient simulations were performed with idealised summer climatic conditions, a constant emissivity of 0.85, and solar absorptivity ranging from 0.001 to 1.0 in increments of 10%. The aforementioned maximum and minimum limits of solar absorptivity represented theoretically transparent and ideal black surfaces respectively. The simulated diurnal variations of the exposed surface temperature are shown in Figure 6-26. For the range of absorptivity characteristics used, the simulated minimum temperatures were unchanged while the maximum temperatures increased by 20.5 °C. This increase was equivalent to 74.7%, and varied linearly at a rate of 7.47% or 1.53 °C per tenth of solar absorptivity as shown in Figure 6-27. For solar absorptivity less than or equal to 0.2 or albedo greater than or equal to 0.8, the maximum temperatures varied moderately about the ambient air

temperature. These results provided further proof of the potential benefits of light coloured surfacing for the reduction of the urban heat island effect.
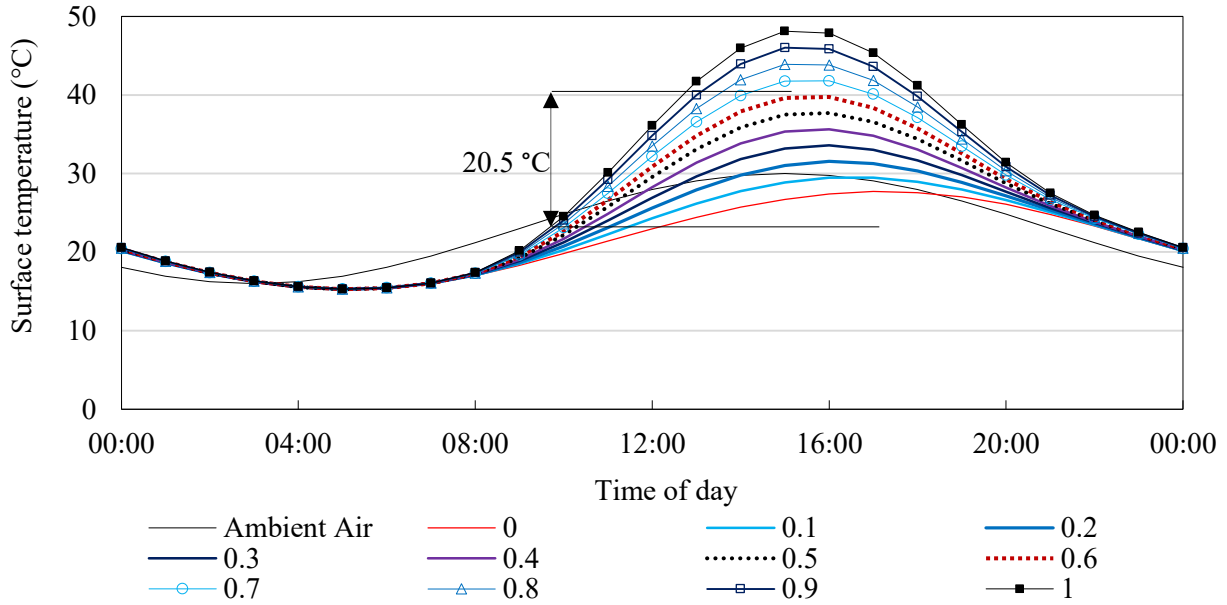

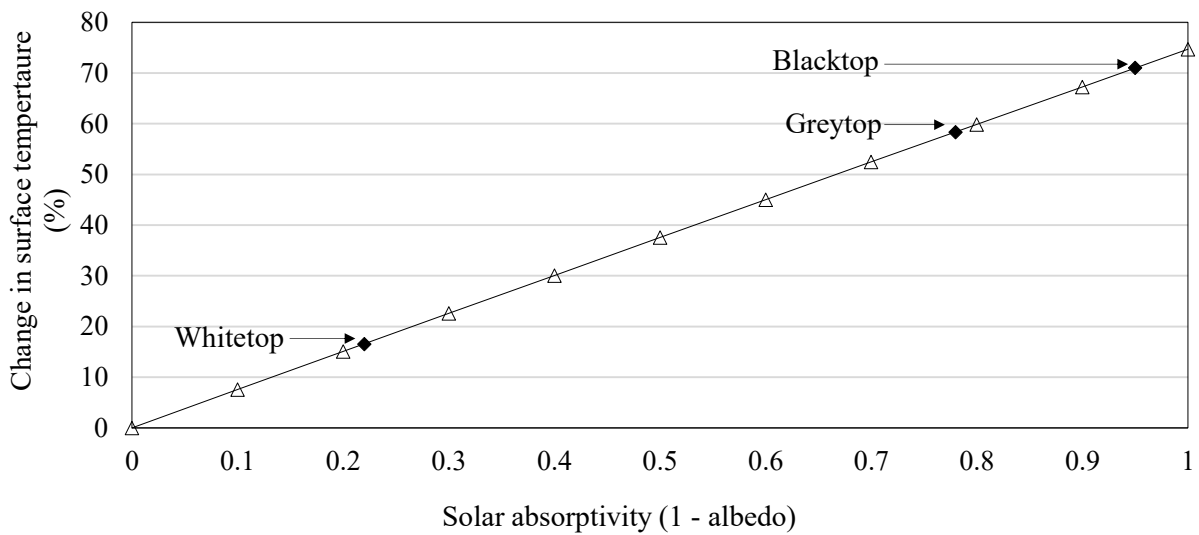Figure 6-26: Diurnal variation of surface temperature with changing solar absorptivity

Figure 6-27: Effect of surface colour on change in maximum surface temperature.

Figure 6-28 shows the diurnal variation in the absolute temperature difference between the exposed and embedded faces. The rates of heat gain and heat loss were observed to increase with increasing solar absorptivity. The former occurred due to increased absorption of global radiation and the latter was due to the higher quantity of longwave radiation that was emitted by the beam surfaces. The quantity of longwave radiation that a body emits is temperature dependent and increases with increasing temperature differentials between the emitting and receiving bodies. As a result, the exposed surface temperatures of the blacktop and greytop beams became cooler than the embedded surfaces between 20:00 and midnight. This effect was observed as a reversal of the thermal gradient along the centreline of each beam.
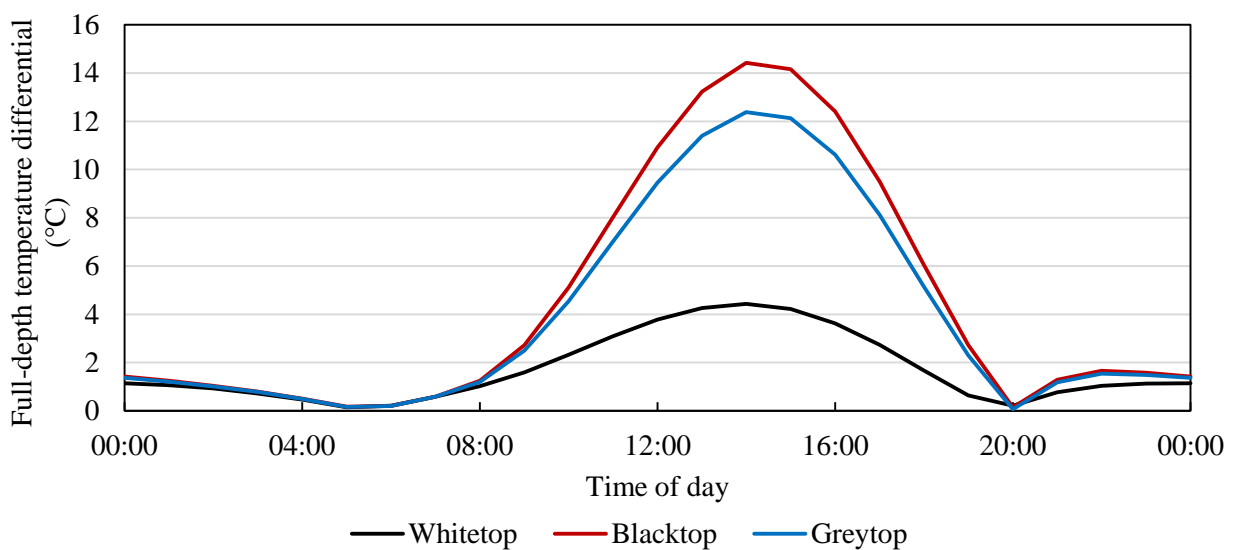
Figure 6-28: Maximum temperature difference between top and bottom surfaces

The absolute difference between the maximum temperatures on the top and bottom surfaces is presented as a function of solar absorptivity in Figure 6-29. The trend line shown appeared to be linear, indicating that for given thermal properties, the solar absorptivity could be selected such that a specific temperature difference could be achieved. This effect indicator provided further evidence in support of the use of light coloured surfacing for the maintenance of indoor temperatures in buildings and subsequent reduction of cooling demands.
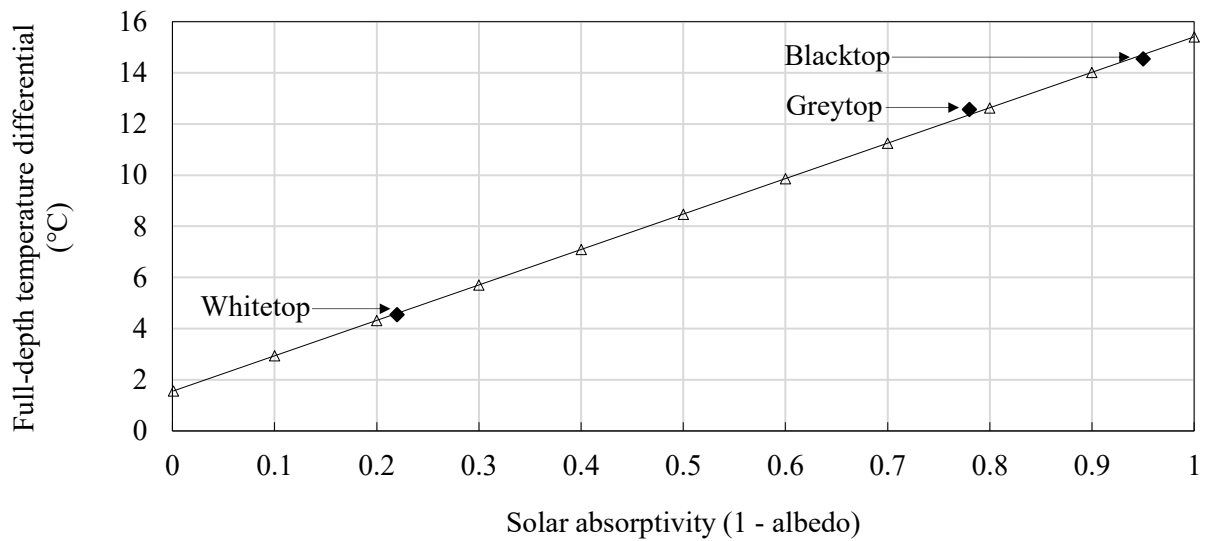
Figure 6-29: Influence of solar absorptivity on maximum temperature differential

Figure 6-30 shows the influence of surface colour on the diurnal effective temperature variation on concrete elements measuring 230 mm x 150 mm. The maximum simulated effective temperatures increased by 16.2 °C across the range of solar absorptivity characteristics, while the minimum effective temperatures were largely unaffected by changes in solar absorptivity.
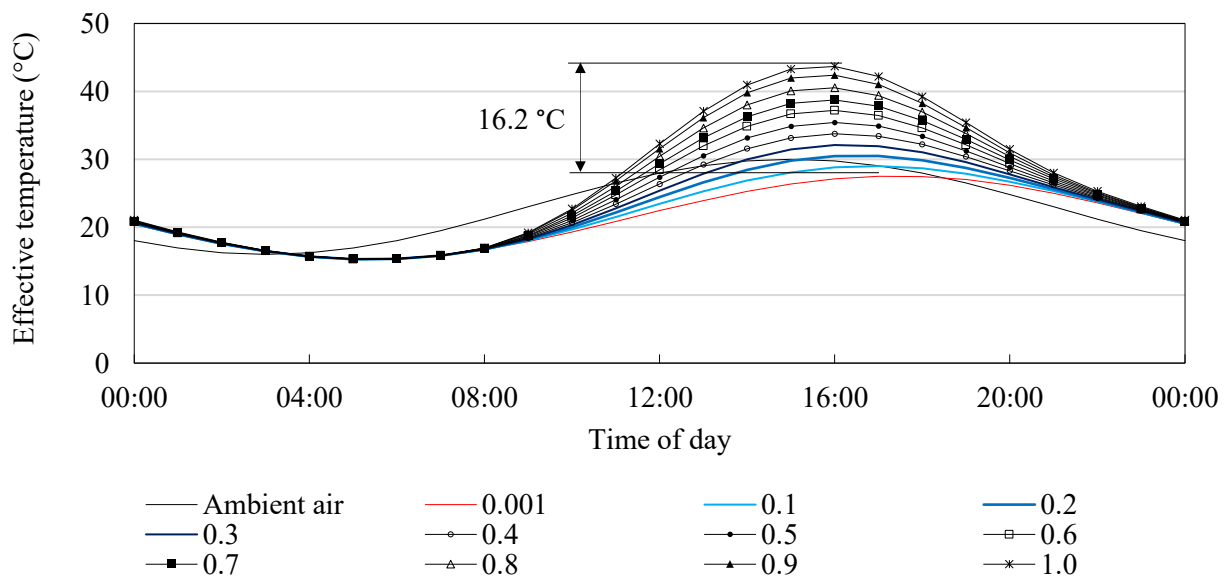
Figure 6-30: Influence of surface colour on effective temperature

Figure 6-31 shows the increase in the maximum and minimum effective temperature as a percentage of the simulated effective temperature for a concrete beam with solar absorptivity equal to 0.001. The maximum effective temperature was observed to increase linearly at a rate 6% or 0.97 °C per tenth of solar absorptivity from 0.001 to 0.5. For absorptivity greater than 0.5, the effective temperature increased non-linearly up to a maximum of 58.9%. The minimum effective temperature remained largely unchanged by increases in solar absorptivity. These results indicated that thermal movements in concrete elements could be increased up to 5 times when the solar absorptivity was increased from 0.2 (White paint) to 0.85 (Black paint). These results further support the trend posited in Figure 6-29 and provide a comparative basis for the use of light coloured surfacing on concrete structures and elements.
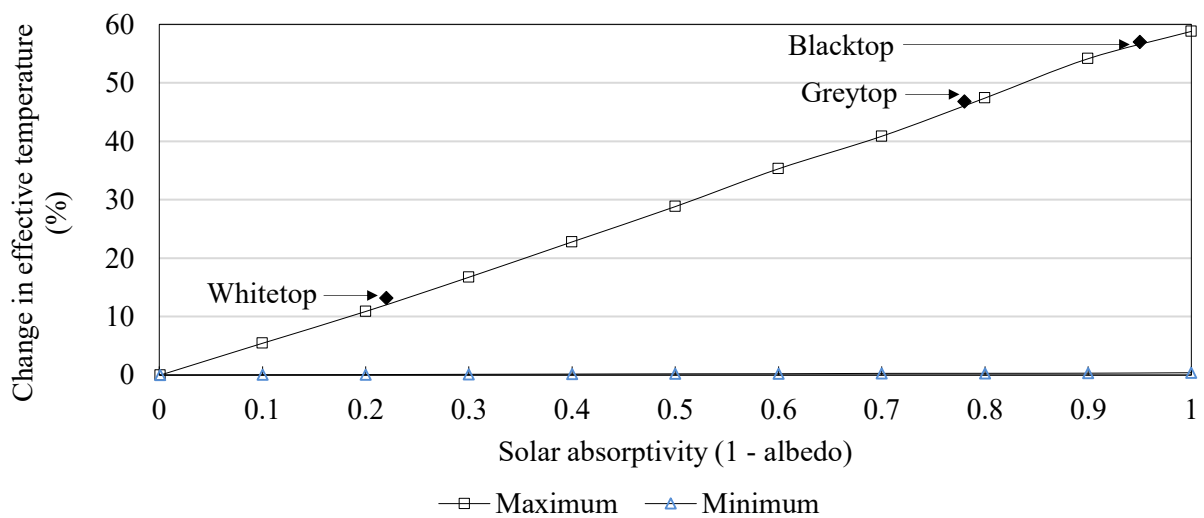

Figure 6-31: Influence of surface colour on change in effective temperature

Figure 6-32 shows the simulated thermal gradients for the diurnal temperature trends shown in Figure 6-25 and Figure 6-28. These results show that the non-linearity of thermal gradients increased with increasing temperature while uniform gradients were observed at times coincident with the minimum simulated temperatures. This indicated that low temperatures were unlikely to result in thermally induced internal restraint that can cause cracking when the tensile strain capacity of concrete is exceeded. The thermal gradients observed in the white top beam were near-uniform throughout the diurnal cycle, providing further support for white topping as a climate change mitigation measure.
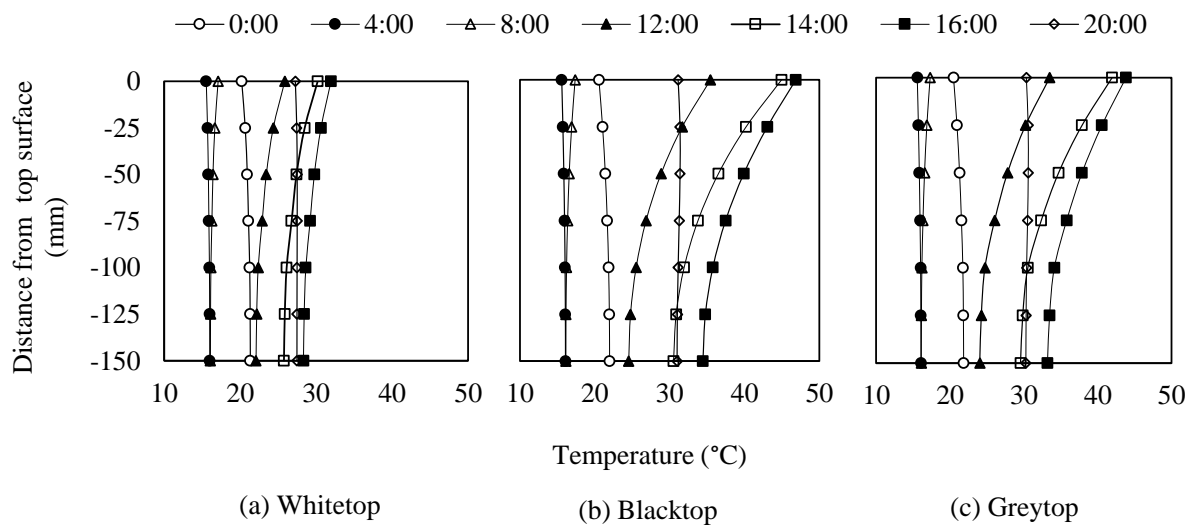
Figure 6-32: Effect of surface colour on thermal gradients

The abovementioned thermal gradients resulted in the thermally induced strains shown in Table 6-4. In the case of positive thermal gradients, the tensile stresses were greatest on the lower edge while compressive strains occurred on the exposed or top surface. The tensile strains were less than the predicted tensile capacity of the concrete (125 μm/m) and were unlikely to cause cracking.

Table 6-4: Influence of solar absorptivity on thermally induced strains

Width	Positive gradient		Negative gradient	
	Tension (μm/m)	Compression (μm/m)	Tension (μm/m)	Compression (μm/m)
Whitetop	11.8	22.8	7.3	3.6
Blacktop	42.3	75.6	8.9	4.6
Greytop	36.0	65.0	8.8	4.4

The influence of cross-sectional dimensions and surface colour on the effective temperature of concrete elements were presented and discussed in Section 6.2 and the preceding text of this Section. The aforementioned parameters were found to significantly influence the thermal behaviour of concrete elements when all other parameters were kept constant. It was, therefore, necessary to investigate the combined effect of surface colour and cross-sectional dimensions.

Figure 6-33 shows the influence of cross-sectional depth on the maximum and minimum effective temperatures of concrete elements with whitetop (WT) and blacktop (BT) surface characteristics for two cross-sectional widths: 230 mm and 1000 mm. These results shown in this figure indicated that:

- Surface colour and cross-sectional depth had no influence on the minimum effective temperature of 230 mm wide concrete elements. This was likely due to the limited thermal mass as well as the shorter heat transfer paths from the core to the vertical edges of the concrete elements.

- The maximum effective temperatures of 230 mm wide concrete elements increased with increasing solar absorptivity. However, these effective temperatures reduced with increasing cross-sectional depth and the effect of surface colour was also observed to reduce with increasing cross-sectional depth. A linear reduction was observed from a maximum temperature difference of 13.4 °C for a depth of 100 mm up to 300 mm, followed by a reduction in the rate of change to a minimum temperature difference of 2.2 °C between the whitetop and blacktop concrete elements.

- The minimum temperatures of 1000 mm wide concrete elements were increased by increasing cross-sectional depth. This was likely due to the increased distance from exposed surface area as well as the reduced effect of heat transfer on the vertical edges of the concrete element, which were found to closely replicate the behaviour of adiabatic boundaries for cross-sectional widths greater than or equal to 600 mm in Section 6.3.2. These temperatures were increased by increasing solar absorptivity, however, this effect was reduced at depths below 230 mm and greater than 600 mm.

- The maximum temperatures followed similar trends for both 230 mm and 1000 mm wide concrete elements. However, the reduction was greater for the 1000 mm wide concrete elements with the maximum effective temperature approaching the minimum effective temperatures with increasing depth.

- For the range of cross-sectional dimensions and extreme surface characteristics used in this investigation, the maximum effective temperatures decreased with increasing thermal mass, however, they were not observed to converge. This indicated that for concrete elements with

maximum cross-sectional dimensions (width or depth) of 1000 mm or less, the effect of surface colour could not be neglected.
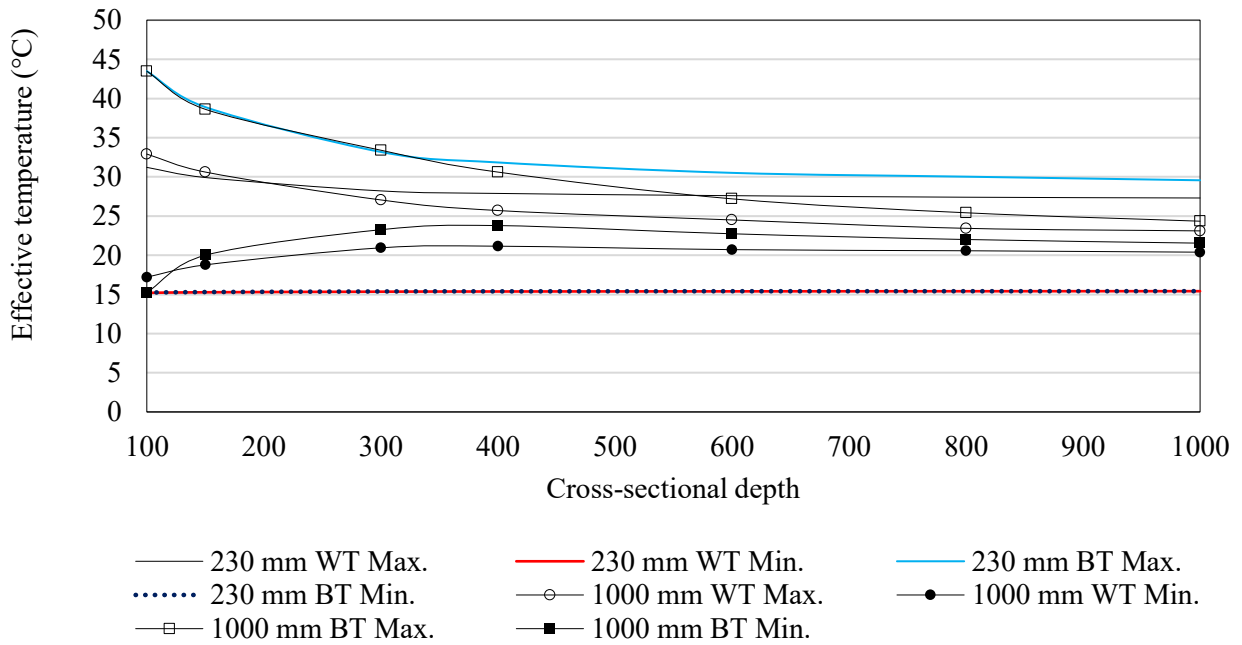

Figure 6-33: Influence of surface colour and cross-sectional depth on effective temperatures

6.5.2 Emissivity

Longwave radiation from the surfaces of concrete structures and elements is governed by the Stefan-Boltzmann law as described in the literature study (See Equation 2-6). Along with absolute temperature differentials, the emissivity factor influences the quantity of longwave radiation that is emitted by a body to the surrounding environment.

The influence of the emissivity factor on the diurnal variation of surface temperatures is shown in Figure 6-34. It was observed that this surface characteristic had no observable effect on the minimum surface temperatures and had a nominal influence on the maximum surface temperatures. These results show that the emissivity factor which is dependent on surface colour, has negligible effect on the maximum surface temperatures recorded before cooling occurs at night. This further supports the observation that solar absorptivity is the dominant surface property that determines the rate and quantity of heat gain during daytime hours while emissivity influences radiative heat loss when ambient temperatures become cooler than the concrete surfaces.
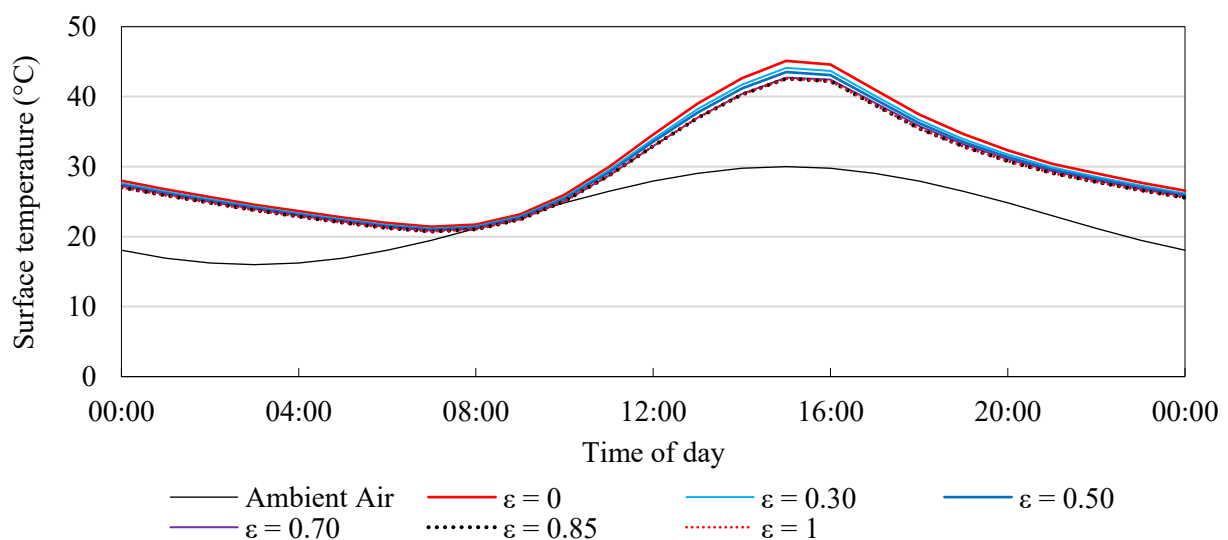
Figure 6-34: Effect of surface emissivity on diurnal surface temperature variation.

The influence of the emissivity factor on the maximum effective and surface temperatures is shown in Figure 6-35. When emissivity was increased from 0 to 0.85, the maximum effective and surface temperatures decreased by 5.5% and 8.4% respectively. These results provide further support to the observations made above.
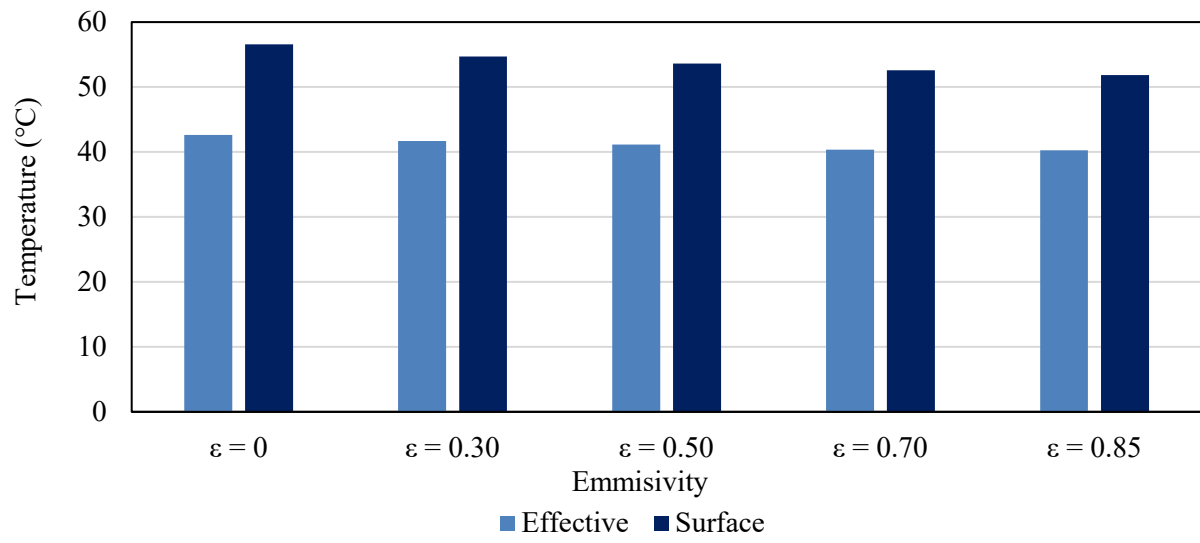
Figure 6-35: Effect of surface emissivity on maximum temperatures

6.6   Summary

This chapter presented the discussion and analysis of results obtained in a parametric investigation of the thermal properties of concrete. It was observed that the solar absorptivity, a non-dimensional value depended on surface colour had the largest influence on maximum surface temperatures and full depth temperature differentials. A comparison of the relative effects of increasing each parameter on the maximum temperatures and full depth differentials in concrete beams with depths less than 300 mm and widths less than 600 mm is shown in Figure 6-36. It can be seen that varying the surface colour from a highly reflective material to a highly absorptive material had the largest effect on surface temperatures. The depth of specimen had the largest effect on the absolute temperature differential between the opposite faces and consequently on the non-linearity of thermal gradients at peak temperatures. Increasing convective cooling and thermal conductivity were found to have beneficial effects on thermal behaviour: Surface temperatures and absolute temperature differentials would be reduced by increasing these parameters.

The abovementioned observations were also, although to a lesser extent, true for concrete elements with depths and widths in excess of 300 mm and 600 mm respectively. Such concrete elements, were found to behave as having adiabatic boundaries resulting in the reduced influence of climatic factors and specimen width.
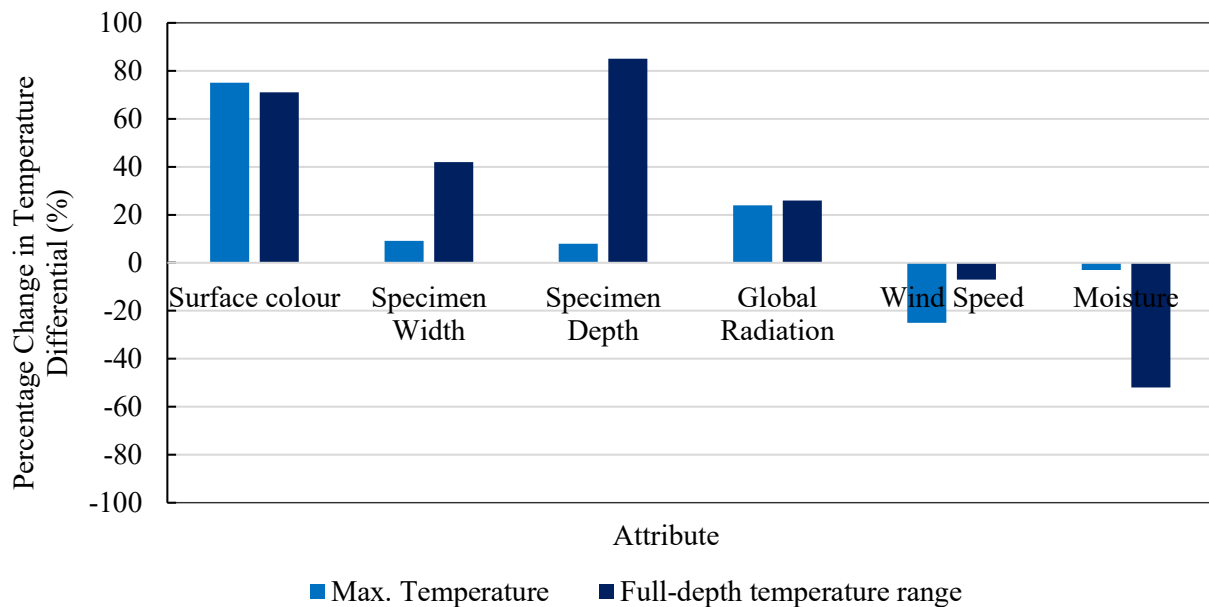

Figure 6-36: Relative effect of various parameters on maximum and full depth temperature differentials

Chapter 7   Conclusions and Recommendations

7.1   Introduction

This chapter presents the conclusions of the research conducted in this study. Three beams were cast using a single concrete mix composition and surfaced with white, black and grey paints. The thermal behaviour of the beams was monitored from January 2018 to July 2018. The data obtained was used to develop and validate a two-dimensional heat transfer model that was subsequently used to perform a parametric study of the effects of several characteristics on the thermal behaviour of concrete elements.

7.2   Conclusions

In accordance to the study objectives described in Chapter 1 of this dissertation, the conclusions that were made are as follows:

- Global or total solar radiation has the largest effect on the thermal energy balance of concrete structures and elements. As such, effective temperatures were up to 15 °C higher in summer than in winter due to the increased intensity of global radiation and duration of daytime hours.
- Wind speed, represented by a convective heat transfer coefficient, resulted in the reduction of surface temperatures in concrete elements. The influence of above wind speed was, however, negligible for speeds in excess of 10 m/s. Through a parametric investigation it was found that wind aids the cooling of surfaces with potential reductions of up to 25% in the maximum surface temperatures for average wind speeds in unobstructed areas.
- Concrete elements with cross-sectional widths greater than or equal to 600 mm could be modelled as having adiabatic boundaries. As such, heat transfer on the vertical faces of the elements or edge effects, could be neglected for such widths. The aforementioned conclusion was true for concrete elements with a maximum depth of 1000 mm.
- Increasing cross-sectional width resulted in increased surface temperatures due to the increased absorption of global radiation, while increasing cross-sectional depth resulted in a reduction in the effective temperature within concrete elements regardless of the surface colour.
- The effects of rainfall and variations in atmospheric relative humidity were not investigated explicitly in this research, however, the effects of moisture variation where investigated. In practice, such variations would occur as a result of precipitation in urban infrastructure and

varied exposure in partially submerged hydraulic structures. It was observed that the increase in thermal conductivity due to increased moisture resulted in the increased uniformity of thermal gradients. Thus, the increase in moisture has temporarily beneficial effects, however, the subsequent drying would likely cause internal restraint and surface cracking if the tensile capacity of concrete is exceeded. Thus wetting and drying cycles could increase the rate of deterioration of concrete structures and elements.

- The quantity of solar radiation that is absorbed is determined by surface colour. In summer the maximum temperature measure in the blacktop beam was approximately 14 °C higher than those in the whitetop beam. The temperatures in the blacktop and greytop beams did not vary significantly.

- The use of light coloured surfacing materials with low solar absorptivity or high albedo, could effectively reduce the surface temperatures of concrete surfaces by between 40% and 60% and up to 75% for blacktopped surfaces. This observation is of particular importance. The mitigation of global climate change and reduction of air temperatures in urban areas requires the use of innovative materials and construction methods.

7.3 Recommendations

This section contains recommendations for the improvement of the research that was conducted during this study as well as items that may be investigated further based on the findings of this research:

- Light surfaces such as white paint overlays could be used to maintain uniform thermal gradients in concrete elements with depths less than 300 mm. Uniform thermal gradients result in a zero stress state in concrete elements in which volume changes are unrestrained thus reducing the likelihood of thermally induced cracking.

- The use of light coloured materials could be a cost effective method that will also have future economic benefits. This research may be used to contribute to the development of climate change mitigation policy to ensure widespread and immediate implementation of light-coloured materials.

- The use of various cooling technologies as techniques for the mitigation of climate change is currently being investigated across the world. Future research should be conducted into the implementation of the findings of this research for smart structures using structural health monitoring techniques which have gained popularity in recent times.

- This beneficial effect of wind movement may be decreased in urban areas as a result of the nature of infrastructure preened in these areas. Consequently, innovative and energy efficient

methods for the artificial cooling of engineering structures are required as the number of high-rise structures increases globally.

- A two dimensional heat transfer model was developed in the Abaqus finite element package, and implemented in a parametric study to investigate the effect of several characteristics on thermal behaviour. The model did not calculate thermal strains as this extended beyond the scope of the study. It is, therefore, recommended that a three-dimensional heat and mass transfer model be developed. Such a model could be extrapolated for use on full scale structures. The effects of environmental loading could be investigated with the inclusion of variations in relative humidity, which was found to have a significant influence on the thermal characteristics of concrete.

Chapter 8   References

Addis, B.J. and Davis, D.E., 1986. *Fulton's concrete technology*. Halfway House, South Africa: Portland Cement Institute.

AfriSam, 2016 Cement Technical Reference Guide. URL https://www.afrisam.co.za/media/76326// Cement_Technical_Reference_Guide.pdf

Akbari, H., 2009. Cooling our communities. A guidebook on tree planting and light-colored surfacing.

Akbari, H., 2012. Opportunities for saving energy and improving air quality in urban heat islands. In Advances in Passive Cooling (pp. 66-128). Routledge.

Alexander, M. and Mindess, S., 2014. *Aggregates in concrete*. CRC Press.

AUC, 2015. Agenda 2063: the Africa we want. *(Addis Ababa, Ethiopia: African Union, September 2015), http://archive. au. int/assets/images/agenda2063. pdf*.

Barnes, K.B., Morgan, J. and Roberge, M., 2001. Impervious surfaces and the quality of natural and built environments. *Baltimore: Department of Geography and Environmental Planning, Towson University*.

Barth, F., Abou-Zeid, M., Fowler, D.W., Nawy, E.G., Allen, J.H., Halvorsen, G.T., Poston, R.W., Barlow, J.P., Hansen, W., Rhoads, R.J., Brander, M.E. and Hassoun, M.N., 2001. Control of Cracking in Concrete Structures. *Report, ACI Committee, 224*, pp.12-16.

Bažant, Z.P., Osman, E. and Thonguthai, W., 1976. Practical formulation of shrinkage and creep of concrete. *Matériaux et Construction*, *9*(6), pp.395-406.

Branco, F.A. and Mendes, P.A., 1993. Thermal actions for concrete bridge design. *Journal of Structural Engineering*, *119*(8), pp.2313-2331.

Brewer, H.W., 1967. General relation of heat flow factors to the unit weight of concrete. Portland Cement Association, Research and Development Laboratories.

Brooks, M.J., Du Clou, S., Van Niekerk, W.L., Gauché, P., Leonard, C., Mouzouris, M.J., Meyer, R., Van der Westhuizen, N., Van Dyk, E.E. and Vorster, F.J., 2015. SAURAN: A new resource for solar radiometric data in Southern Africa. *Journal of energy in Southern Africa*, *26*(1), pp.2-10.

Brundtland, G., 1987. Our common future: Report of the 1987 World Commission on Environment and Development. *United Nations, Oslo*, *1*, p.59.

Campbell-Allen, D. and Thorne, C.P., 1963. The thermal conductivity of concrete. *Magazine of concrete Research*, *15*(43), pp.39-48.

Cavanaugh, K., McCall, M.S.B.W.C., Speck, J.F., Musser, T.W.B.D.W., Spinney, S.C., Ries, K.D.C.J.P., Sukenik, A.L., Szoke, S.S., Bradfield, M.S., Bremmer, T.W. and Graber, D.W., 2002. Guide to thermal properties of concrete and masonry systems. *American Concrete Institute, ACI*.

CEN (European Committee for Standardization), 2004. Eurocode 1: Actions on structures—Part 1-5: General actions—Thermal actions. *EN 1991-1-5*.

CEN (European Committee for Standardization), 2009. Eurocode 1: Actions on structures—Part 1-5: General actions—Thermal actions. *EN 1991-1-5*.

Côté, J. and Konrad, J.M., 2005. Thermal conductivity of base-course materials. *Canadian Geotechnical Journal*, *42*(1), pp.61-78.

Damtoft, J.S., Lukasik, J., Herfort, D., Sorrentino, D. and Gartner, E.M., 2008. Sustainable development and climate change initiatives. *Cement and concrete research*, *38*(2), pp.115-127.

Domone, P. and Illston, J.M., 2010. Construction materials: their nature and behavior, 2010 Spon Press.

Doulos, L., Santamouris, M. and Livada, I., 2004. Passive cooling of outdoor urban spaces. The role of materials. Solar energy, 77(2), pp.231-249.

Elbadry, M.M. and Ghali, A., 1983. Temperature variations in concrete bridges. *Journal of Structural Engineering*, *109*(10), pp.2355-2374.

EN, B., 2000. 197-1, Cement-Part 1: Composition, specifications and conformity criteria for common cements. *British Standards Institution*.

Emerson, M., 1968. *Bridge temperatures and movements in the British Isles*. (No. TRRL Lab Report 228).

Emerson, M., 1973. *The calculation of the distribution of temperature in bridges* (No. TRRL Lab Report 561 R&D Rept.).

Gloyne, R.W., 1972. Diurnal-variation of global radiation on a horizontal surface-special reference to Aberdeen. *Meteorological Magazine*, *101*(1195), p.44.

Google Maps., 2018. *Google Maps* URL: https://www.google.com/maps/ [Accessed 1 Jan. 2018].

Gribniak, V., Kaklauskas, G., Kliukas, R. and Jakubovskis, R., 2013. Shrinkage effect on short-term deformation behavior of reinforced concrete–when it should not be neglected. Materials & Design, 51, pp.1060-1070.

Gui, J., Phelan, P.E., Kaloush, K.E. and Golden, J.S., 2007. Impact of pavement thermophysical properties on surface temperatures. *Journal of Materials in Civil Engineering*, *19*(8), pp.683-690.

Hall, K. and Tayabji, S., 2011. Coefficient of thermal expansion in concrete pavement design (No. FHWA-HIF-09-015).

Harmathy, T.Z. and Allen, L.W., 1973, February. Thermal properties of selected masonry unit concretes. In *Journal Proceedings* (Vol. 70, No. 2, pp. 132-142).

Hoffmann, K., 1974. Applying the Wheatstone bridge circuit. Germany: HBM.

HRB, H., 1962. *The AASHO Road Test, Report 5: Pavement Research* (No. 61E). Special Report.

Huang, Y.H., 2004. Pavement design and analysis. Pearson/Prentice Hall.

Hulme, M., Doherty, R., Ngara, T., New, M. and Lister, D., 2001. African climate change: 1900-2100. *Climate research*, *17*(2), pp.145-168.

Hulsey, J.L. and Powell, D.T., 1993. Rational weather model for highway structures. *Transportation research record*, (1393).

Incropera, F.P., Dewitt, D.P., Bergman, T. and Lavine, A., 2007. Fundamentals of Heat and Mass Transfer.

IPCC, 2018. Global Warming of 1.5° C: An IPCC Special Report on the Impacts of Global Warming of 1.5° C Above Pre-industrial Levels and Related Global Greenhouse Gas Emission Pathways, in the Context of Strengthening the Global Response to the Threat of Climate Change, Sustainable Development, and Efforts to Eradicate Poverty. Intergovernmental Panel on Climate Change.

Jones, P.D., Osborn, T.J. and Briffa, K.R., 2001. The evolution of climate over the last millennium. *Science*, *292*(5517), pp.662-667.

Kearsley, EP., Lecture notes on Aggregates for concrete, Postgraduate course in Concrete Technology, University of Pretoria, 2017.

Khan, M.I., 2002. Factors affecting the thermal properties of concrete and applicability of its prediction models. *Building and Environment*, *37*(6), pp.607-614.

Kim, K.H., Jeon, S.E., Kim, J.K. and Yang, S., 2003. An experimental study on thermal conductivity of concrete. *Cement and Concrete Research*, *33*(3), pp.363-371.

Larsson, O. and Thelandersson, S., 2011. Estimating extreme values of thermal gradients in concrete structures. *Materials and structures*, *44*(8), pp.1491-1500.

Lentz, A.E. and Monfore, G.E., 1966. *Thermal conductivities of Portland cement paste, aggregate and concrete down to very low temperatures*. Portland Cement Association, Research and Development Laboratories.

Lewis, R.W., Morgan, K., Thomas, H.R. and Seetharamu, K., 1996. *The finite element method in heat transfer analysis*. John Wiley & Sons.

Li, H., Harvey, J. and Jones, D., 2014. Development and Preliminary Validation of Integrated Local Microclimate Model for Numerical Evaluation of Cool Pavement Strategies. *Transportation Research Record: Journal of the Transportation Research Board*, (2444), pp.151-164.

Marshall, A.L., 1972. The thermal properties of concrete. *Building Science*, *7*(3), pp.167-174.

Monteith, J.L., 1965. Light distribution and photosynthesis in field crops. *Annals of Botany*, *29*(1), pp.17-37.

Neville, A.M., 2011. Properties of Concrete, 4th. *London Pearson Education Limited*, *443*(846), p.444.

Neville, A.M. and Brooks, J.J., 1987. *Concrete technology*.

Oke, T.R., 2002. *Boundary layer climates*. Routledge.

Owens, G. ed., 2009. *Fulton's concrete technology*. Cement & Concrete Institute.

Potgieter, I.C. and Gamble, W.L., 1989. Nonlinear temperature distributions in bridges at different locations in the United States. *PCI JOURNAL*, *34*(4), pp.80-103

Power, H.C. and Mills, D.M., 2005. Solar radiation climate change over Southern Africa and an assessment of the radiative impact of volcanic eruptions. *International journal of climatology*, *25*(3), pp.295-318.

Rhodes, J.A., 1978. —Thermal Properties. In *Significance of Tests and Properties of Concrete and Concrete-Making Materials*. ASTM International.

Robertson, E.C., 1988. *Thermal properties of rocks* (No. 88-441). US Geological Survey,.

Rosenfeld, A.H., Romm, J.J., Akbari, H., Pomerantz, M. and Taha, H.G., 1996. Policies to reduce heat islands: magnitudes of benefits and incentives to achieve them (No. LBL-38679; CONF-9608106-9). Lawrence Berkeley National Lab., CA (United States).

Simulia, D.S., 2011. ABAQUS 6.11 User's manual. *Dassault Systems, Providence, RI*.

SIS, Swedish Standards Institute, 2005. SS EN 1991-1-5, Eurocode 1: actions on structures—part 1–5: general actions—thermal actions

South African Weather Bureau, 1978. Monthly weather reports for the year 1978. South African Weather Bureau, WB35, Pretoria

Taha, H., Akbari, H., Rosenfeld, A. and Huang, J., 1988. Residential cooling loads and the urban heat island—the effects of albedo. *Building and environment*, *23*(4), pp.271-283.

Taha, H., Sailor, D.J. and Akbari, H., 1992. High-albedo materials for reducing building cooling energy use.

Tatro, S.B., 2006. Thermal properties. *Significance of Tests and Properties of Concrete and Concrete-Making Materials*. ASTM International.

Tatro, S.B., ACI Committee 207, 2007. Report on Thermal and Volume Change Effects on Cracking of Mass Concrete. American Concrete Institute.

Thepchatri, T., Johnson, C.P. and Matlock, H., 1977. *Prediction of temperature and stresses in highway bridges by a numerical procedure using daily weather reports* (No. FHWATX-77-23-1 Interim Rpt.).

Teller, L.W. and Sutherland, E.C., 1936. The structural design of concrete pavements-part 4-a study of the structural action of several types of transverse and longitudinal joint designs. *Public roads*.

Troxell, G.E., Davis, R.E. and Raphael, J.M., 1958. Long–Term Creep and Shrinkage Tests of Plain and RC. In Proceedings ASTM (Vol. 58).

UNFCC, 2015. Adoption of the Paris agreement. *United Nations Office at Geneva, Geneva Google Scholar*.

U.S. Bureau of Reclamation, 1940. Thermal Properties of Concrete," Boulder Canyon Project Final Reports, *Bulletin No. 1,* Part VII, Denver, CO.

Valore, R.C., 1958, November. Insulating concretes. *ACI Journal Proceedings* (Vol. 53, No. 11, pp. 509-532).

Valore, R.C., 1980. Calculations of U-values of hollow concrete masonry. Concrete International, 2(2), pp.40-63.

Vishay Precision Group, 2017. Special Use Sensors – Concrete Embedment Strain Gages. *Document No. 11526.*

Williamson, R.H. and Marais, C.P., 1975. Pavement Temperatures in Southern Africa. *The Civil Engineers in South Africa, South African Institute of Civil Engineers*.

Yuan, H.W., Lu, C.H., Xu, Z.Z., Ni, Y.R. and Lan, X.H., 2012. Mechanical and thermal properties of cement composite graphite for solar thermal storage materials. *Solar energy*, *86*(11), pp.3227-3233.

Appendix A Construction Drawings

A.1   List of Drawings

1. Thermistor string dimensions
2. Final thermistor layout
3. Typical cross-section of experimental set-up

.

1. All dimensions are in mm

120

100

100
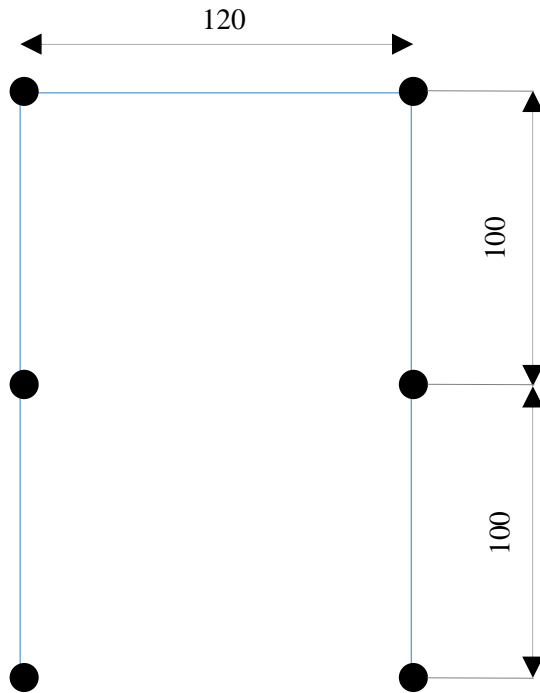
OUTER STRING (3No)

SCALE: NTS

30

50

50

50

50
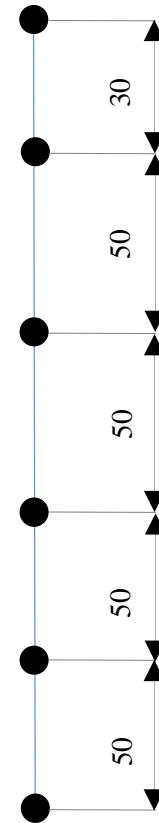
CENTRAL STRING (3No)

SCALE: NTS

DESIGNED	T.M.	SCALE	AS SHOWN	TITLE	Thermistor strings
DRAWN	T.M.	DATE	01/2018	DRAWING NO.	MEng/001
CHECKED	E.K.	REV	01		

UNIVERSITEIT VAN PRETORIA
UNIVERSITY OF PRETORIA
YUNIBESITHI YA PRETORIA

THERMISTOR LAYOUT

SCALE: NTS

NOTES

1. All dimensions are in mm
2. All thermistors are logged on Campbell Scientific CR6 data logger.

Temperature conversion:

$$°C = \frac{1}{0.00025374 \ln(R) + 0.0011958} - 273$$

DESIGNED	T.M.	SCALE	AS SHOWN	TITLE · Final thermistor layout
DRAWN	T.M.	DATE	01/2018	DRAWING NO. · MEng/002
CHECKED	E.K.	REV	01	

UNIVERSITEIT VAN PRETORIA
UNIVERSITY OF PRETORIA
YUNIBESITHI YA PRETORIA

Laboratory roof

Timber frame

Bidim® Geotextile

Silica sand

Instrumented concrete beam

Plinth

150

230

150

50

1200
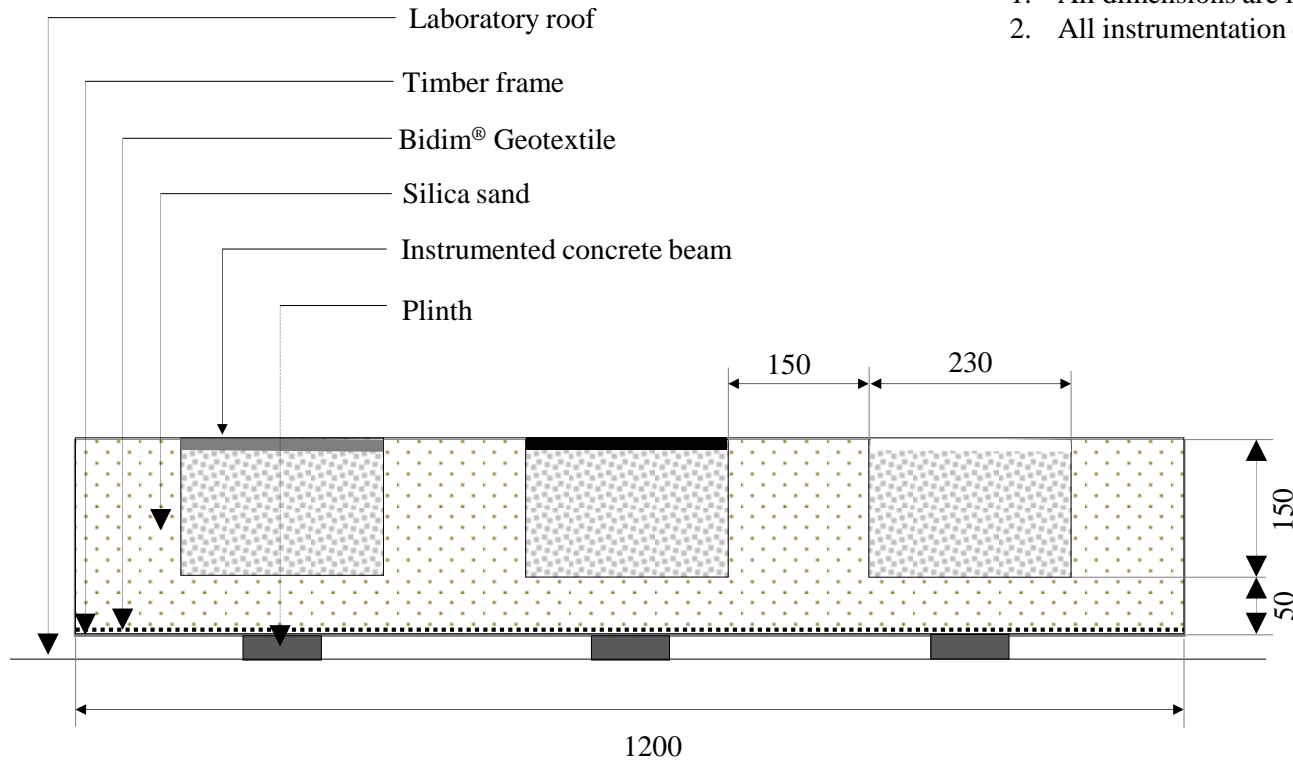
EXPERIMENTAL SET-UP: TYPICAL CROSS-SECTION

SCALE: NTS

DESIGNED	T.M.	SCALE	AS SHOWN	TITLE	Typical cross-section
DRAWN	T.M.	DATE	01/2018	DRAWING NO.	MEng/003
CHECKED	E.K.	REV	01		

UNIVERSITEIT VAN PRETORIA
UNIVERSITY OF PRETORIA
YUNIBESITHI YA PRETORIA

Appendix B Temperature Data

B.1 Calculation of Effective Temperature

An example of the calculation procedure used to calculate the effective temperature of a concrete cross-section is presented in below. Figure B-1 and Figure B-2 respectively show the temperature and area of each region.
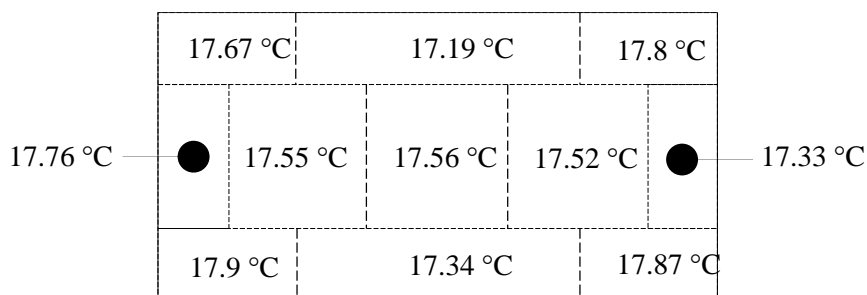
.Figure B1: Measured temperature probe data.
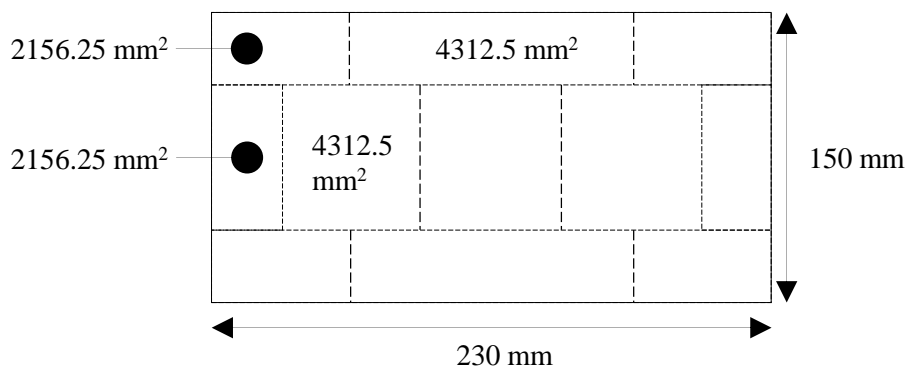
.Figure B2: Area of region associated with each temperature probe.

The resulting effective temperature is calculated according to Equation 2-21:

$$T_{mean} = \frac{\sum_1^n T_i \cdot A_i}{\sum_1^n A_i}$$

$$= \frac{2156.25 \cdot (17.87 + 17.9 + 17.76 + 17.33 + 17.33 + 17.67 + 17.8)}{34500} + 4312.50 \cdot (17.55 + 17.56 + 17.52 + 17.19 + 17.34)$$

$$= 17.54 \text{ °C}$$
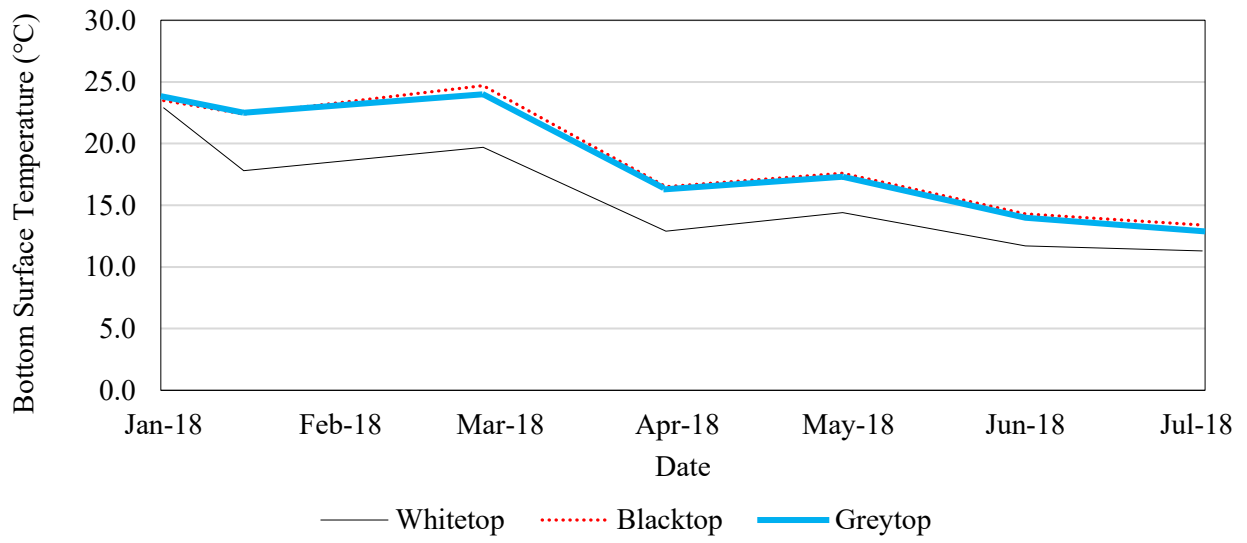
B.2   Average Monthly Temperatures

The following figures show the average monthly near-surface and core temperatures measured during the experimental study.
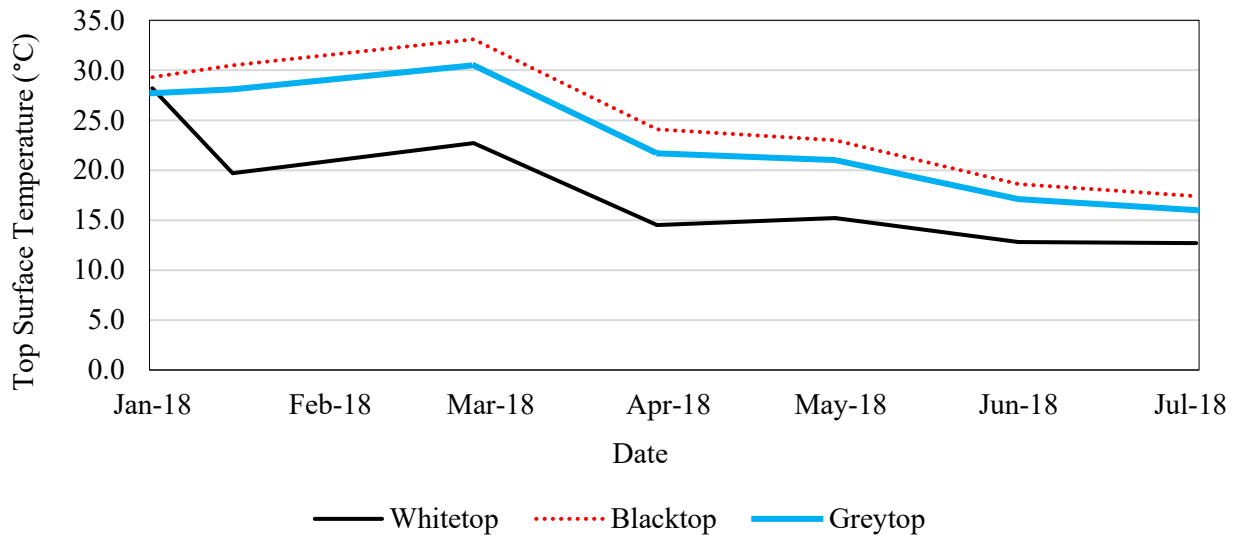
.Figure B3: Average monthly near-surface temperatures on top surface.
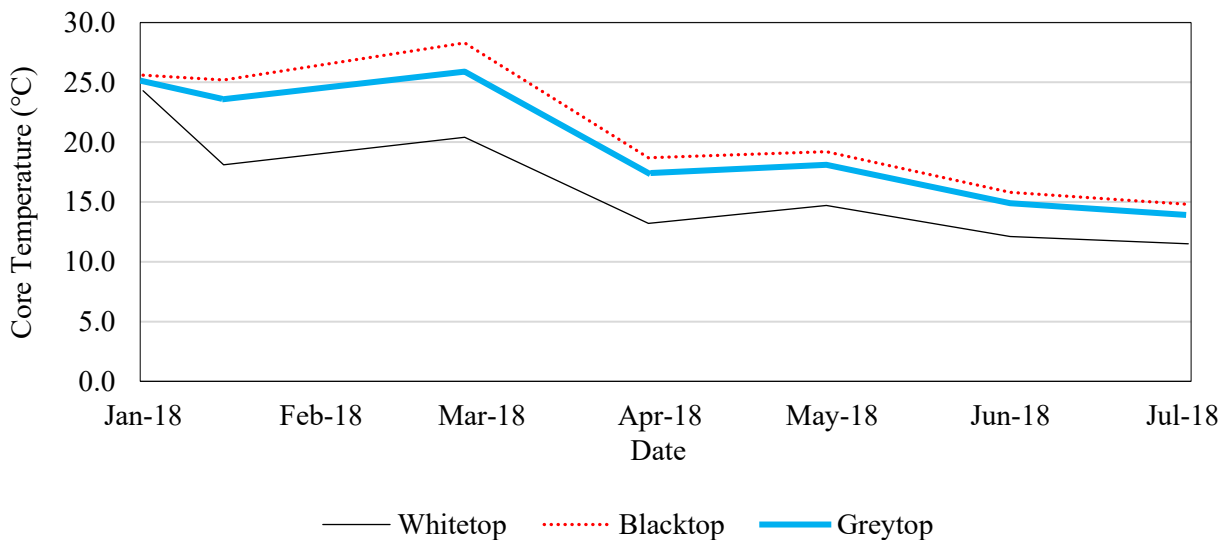
.Figure B4: Average monthly core temperatures.

.Figure B5: Average monthly near-surface temperatures on bottom surface.

Appendix C Thermal Gradients

C.1 Simulated Thermal Gradients

The following figures show selected thermal gradients as simulated by the two-dimensional heat transfer model.
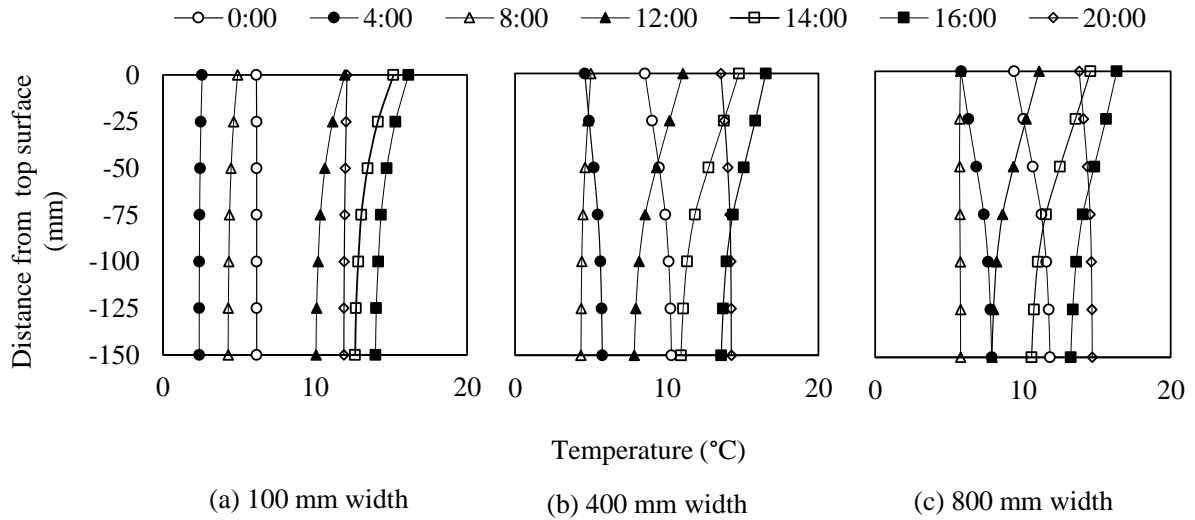
C.1.1 Effect of Concrete Beam Width

(a) 100 mm width

(b) 400 mm width

(c) 800 mm width

Figure C-1: Influence of concrete beam width on thermal gradients

C.1.2 Effect of Concrete Beam Depth
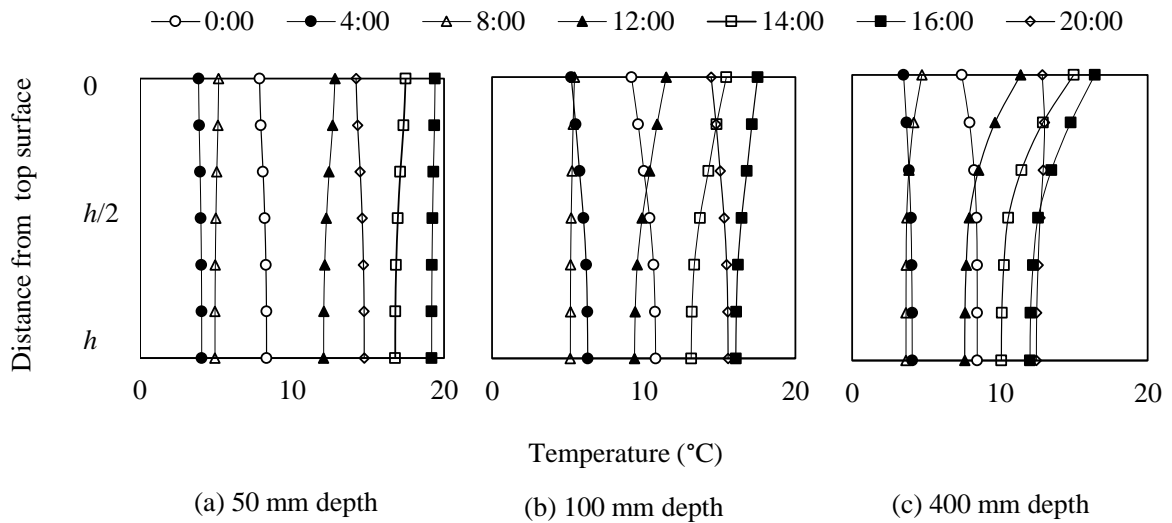

(a) 50 mm depth

(b) 100 mm depth

(c) 400 mm depth

Figure C-2: Influence of concrete beam depth on thermal gradients
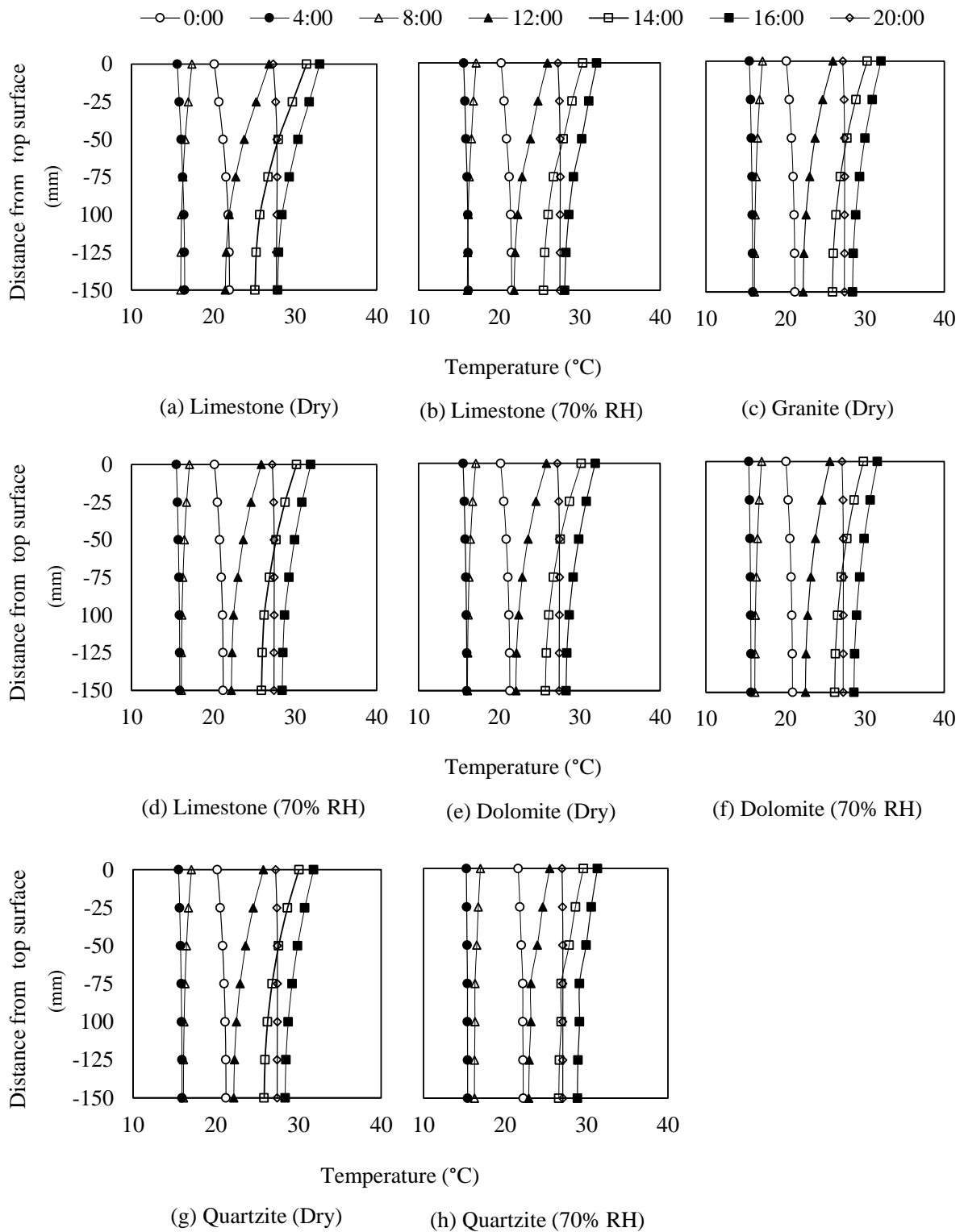
C.1.3 Effect of Concrete Thermal Properties

Figure C-2: Influence of concrete aggregate type on thermal gradients